Coupling the Spectral Element Method with a modal solution for Elastic Wave Propagation in Global Earth Models

Y. CAPDEVILLE[1] *, E. CHALJUB[1,2] †, J.P. VILOTTE[1,2] and J.P. MONTAGNER[1]

[1] *Département de Sismologie, Institut de Physique du Globe de Paris, 4 Place Jussieu, 75252–Paris cedex05 (France)*

[2] *Département de Modélisation Physique et Numérique, Institut de Physique du Globe de Paris*

SUMMARY

We present a new method for wave propagation in global Earth models based upon the coupling between the spectral element method and a modal solution method. The Earth is decomposed in two parts, an outer shell with 3D lateral heterogeneities and an inner sphere with only spherically symmetric heterogeneities. Depending on the problem, the outer heterogeneous shell can be mapped as the whole mantle or restricted only to the upper mantle or the crust. In the outer shell, the solution is sought in terms of the spectral element method, which stem from a high order variational formulation in space and a second-order explicit scheme in time. In the inner sphere, the solution is sought in terms of a modal solution in frequency after expansion on the spherical harmonics basis. The spectral element method combines the geometrical flexibility of finite element methods with the exponential convergence rate of spectral methods. It avoids the pole problems and allows for local mesh refinement, using a non conforming discretization, for the resolution of sharp variations and topography along interfaces. The modal solution allows for an accurate isotropic representation in the inner sphere. The coupling is introduced within the spectral element method via a Dirichlet-to-Neumann (DtN) operator. The operator is explicitly constructed in frequency and in generalized spherical harmonics. The inverse

transform in space and time requires special attention and an asymptotic regularization. The coupled method allows a significant speed-up in the simulation of the wave propagation in earth models. For spherically symmetric earth model, the method is shown to have the accuracy of spectral transform methods and allow the resolution of wavefield propagation, in 3D laterally heterogeneous models, without any perturbation hypothesis.

Key words: Global wave propagation – coupled method – spectral elements – modal solution – surface waves – body waves – synthetic seismograms.

1   INTRODUCTION

The availability of continuously increasing large data sets of high quality broadband digital data from global instrument deployments and global data centers, like IRIS or GEOSCOPE, have been critical in fostering global seismology. Improvement of seismic earth models must incorporate new numerical methods that allow the computation of detailed waveforms and provide insights into the physics of the wave propagation in models with a broad range of heterogeneity scales. This new challenge takes place at the same time as the advent of parallel computers. Progress in computational seismology is now bringing direct numerical simulation of wave propagation back into the heart of global seismology.

In the past decades much effort has been expanded to improve images of the large scale variations of velocity heterogeneities in the earth's mantle with the aim of inferring some information on the thermal and chemical heterogeneities and to relate them to dynamic processes. Arrival times (Vasco & Johnson, 1998; van der Hilst *et al.*, 1997; van der Hilst *et al.*, 1998; Grand *et al.*, 1997), differential travel times of surface phases and body waves (Su *et al.*, 1994; Liu & Dziewonski, 1998; Masters *et al.*, 1996), normal mode coefficients (Resovsky & Ritzwoller, 1999), and waveform analysis (Li & Romanowicz, 1996) have been used in global tomography providing increasing evidence that the earth's mantle is laterally heterogeneous in a broad range of scales, with coherent large scale patterns. Tomographic models, derived from global or regional studies, agree reasonably well, at least between 100 and 600 Km, on the long wavelength structure, i.e. the first 12 degrees in spherical harmonics with a spatial resolution of the order of 1500 Km at the surface (Dziewonski, 1995; Ritzwoller & Lavely, 1995). Regional tomographic models tend, however, to predict somewhat higher power spectral density at shorter wavelengths than can be resolved in global studies (Chevrot *et al.*, 1998b; Chevrot *et al.*, 1998a). An increasing number of indirect studies suggest the importance of small scale heterogeneities

both in the upper (Aki, 1981; Kennett, 1997; Kennett & Bowman, 1990) and lowermost part of the mantle (Lay, 1995; Ding & Helmberger, 1997; Lay *et al.*, 1997; Lay *et al.*, 1998; Pulliam & Sen, 1999; Kendall & Silver, 1996; Matzel *et al.*, 1996; Vinnik *et al.*, 1996).

The impact of the theoretical assumptions used in the methods for computing synthetic seismograms has not yet been fully assessed but recent studies by Clévédé *et al.* (2000) and Igel *et al.* (2000) have pointed out the importance of the theoretical approximations in the tomography models. Direct numerical simulation (DNS) methods are now required to: understand the physics of wave propagation in heterogeneous earth models; assess the impact of the theoretical approximations used in practice to compute the synthetic seismograms; assess the actual resolution of the tomographic models and of the seismic records with respect to small scale heterogeneities. However, in contrast to the rapid progress of computational seismology in exploration geophysics, DNS methods are less advanced in global seismology in part because of the large scale of the system and of the pole problems associated with the spherical coordinates system.

The principal methods used today in global seismology for the computation of synthetic seismograms are based upon spectral transform methods (STM) (Gelfand *et al.*, 1963; Newman & Penrose, 1966; Takeuchi & Saito, 1972; Phinney & Burridge, 1973; Wu & Yang, 1977), which expand the solution, and the physical variables, into vector spherical harmonics defined on a spherical reference configuration. These methods are exceptionally accurate and stable for smooth functions with a uniform resolution on the sphere and provide an elegant solution to the so-called pole problem.

Among these methods, normal mode summation methods have long been used in global seismology (Dahlen & Tromp, 1998; Lognonné & Clévédé, 2000). The normal modes of a reference spherical configuration, and the corresponding eigenfrequencies, are computed as intermediate functions for the computation of the seismograms at the surface. Asphericity and lateral heterogeneity distributions are then considered as perturbations. Perturbation theories (Dahlen, 1969; Woodhouse, 283; Valette, 1987; Valette, 1989; Lognonné, 1991; Dahlen & Tromp, 1998; Lognonné & Clévédé, 2000) rely on two approximations: small lateral variations of amplitude and small lateral gradients. The most sophisticated perturbative normal mode methods (Lognonné & Romanowicz, 1990; Lognonné, 1991; Lognonné & Clévédé, 1997; Lognonné & Clévédé, 2000) requires the coupling of modes along the same dispersion branch while the multiple scattering is resolved up to the accuracy limit of the actual order of the perturbative expansion. Even for only a second order expansion, these methods face serious computational limits when dealing with dominant periods of less than 50 seconds. For practical analysis, high frequency (asymptotic) approximations (Romanowicz & Roult, 1986; Romanowicz, 1987; Li & Tanimoto, 1993) are combined with a Born approximation (Snieder & Romanowicz, 1988; Tromp & Dahlen, 1992; Pollitz, 1998; Friederich, 1998) in the computation of synthetic seismograms.

High frequency approximations assume that the wavelengths of the heterogeneities remain large compared to the dominant propagating wavelength while first order Born approximations assume that heterogeneities can be considered as secondary sources. Despite continuous theoretical improvements and the many successes of refined asymptotic theories, especially for surface waves, these methods face serious theoretical problems when finite frequency effects on the whole waveform are important. Higher order asymptotic approximations become rapidly computationally expensive and can not deal with localized zones of high velocity contrasts.

Other spectral transform methods directly solve the elastodynamics equation in the frequency domain, bypassing the intermediate step of calculating the normal modes. For spherical earth models, the method developed by Friederich & Dalkolmo (1995) integrates the strong form of the elastodynamics equation expanded spatially on the vector spherical harmonics basis. The synthetic seismograms are then obtained after summation over the spherical harmonics and a numerical inverse Fourier transform. Another interesting method based on a weak variational formulation of the elastodynamics equation in the frequency domain was proposed by Hara *et al.* (1993) and Geller & Ohminato (1994). This method makes use of a weighted residual formalism (Finlayson, 1972; Zienkiewicz & Morgan, 1983), in which boundary and continuity conditions becomes natural boundary conditions with the help of appropriate surface integrals. Using a Galerkin approximation, the trial and the weight functions are chosen to be the tensor product of linear splines in the radial direction and generalized spherical harmonics basis functions. Cummins *et al.* (1994), Cummins *et al.* (1994) and Geller & Ohminato (1994) used the direct solution method (DSM) to compute synthetic seismograms for laterally homogeneous media in spherical coordinates. In this case, there is no coupling between the toroidal and the spheroidal modes. Due to the degeneracy of the spherically symmetric case, the algebraic system can be decomposed into smaller separate banded subsystems for spheroidal and toroidal displacements that are solved for each angular and azimuthal order. For laterally heterogeneous models, all angular and azimuthal orders become coupled and the computational requirement increases drastically. This implies some approximations such as a truncation of the coupling between angular orders, the restriction to axisymmetric lateral variations (zonal) (Cummins *et al.*, 1997), or the use of Born approximations (Takeuchi *et al.*, 2000).

All these methods, based on global spectral transforms, usually solve the elastodynamics problem in frequency and do not provide direct informations on the wave propagation. Moreover, spectral transform methods involve an expansion of the variables into a non local spherical harmonics basis as well as the computation of the spatial derivatives in this basis. The major drawbacks are therefore: the need for high order spherical expansions when the lateral variations become rough and spatially localized; the difficulty to incorporate mesh refinement; the inherent computational complexity and the

communication overheads. Despite recent improvements (Kostelec *et al.*, 2000), the transform requires $\mathcal{O}(N^3)$ operations, where N is the number of points in latitude. On distributed memory architectures, the global structure of the communication between processors involved in this transform imposes an overhead which becomes critical as N is increased.

A limited number of studies have been recently conducted toward direct numerical simulation of seismic wave propagation in spherical earth models. They are based upon finite differences or pseudo-spectral methods. Finite differences (FD) have been widely used in exploration seismology. They however suffer from grid dispersion near strong gradients and require a large number of grid points to achieve the expected accuracy (Kelly *et al.*, 1976). Balancing the trade-off between numerical dispersion and the computational cost turns out to be quite difficult (Virieux, 1986; Dablain, 1986; Bayliss *et al.*, 1986; Levander, 1988) and critical in global seismology (Alterman *et al.*, 1970). Higher order methods, like the pseudo-spectral methods, enable to achieve the expected accuracy using fewer grid points. Maximum efficiency is obtained when using fast Fourier transforms but for more general boundary conditions the set of truncated Fourier series are often replaced by a set of algebraic polynomials (Kosloff *et al.*, 1990; Fornberg, 1996), Chebychev or Legendre, with the drawback of introducing non uniform grid points. This limitation can lead to severe stability problems that can be partly overcome with the help of generalized coordinates (Fornberg, 1988; Kosloff & Tal-Ezer, 1993). Finite differences and pseudo-spectral methods are based on a strong formulation of the elastodynamics initial boundary value problem and face severe limitations for an accurate approximation of free-surface and continuity conditions which is crucial for long term simulation of surface and interface waves. Finite differences and pseudo spectral methods have been used in global seismology under rather restricted approximations: axisymmetric P and SV (Furumura *et al.*, 1998; Furumura *et al.*, 1999) or SH (Igel & Weber, 1996; Chaljub & Tarantola, 1997) wave propagation avoiding the inherent pole problems associated with spherical coordinates. The major problem with these grid-based methods is that, unlike global spectral transform methods, they fail to provide an isotropic representation of scalar functions on a sphere. Latitude-longitude grid points become clustered near the poles leading to severe CFL conditions. This problem can be partly circumvented when using latitude-longitude pseudo-spectral solvers (Merilees, 1973; Fornberg, 1995) in conjunction with suitable spectral filters (Jakob-Chien & Alpert, 1997; Yarvin & Rokhlin, 1998) or when resorting to a multidomain approach (Sadourny, 1972; Heikes & Randall, 1995; Rančić *et al.*, 1996). However in the latter case, one is faced with the non trivial problem of how to glue together the different coordinate systems. This implies overlapping regions between the mesh subdomains which put severe stability conditions. These techniques have not yet received much attention in the seismological community.

Another direction, that was recently explored (Chaljub, 2000; Chaljub *et al.*, 2001), is to resort to

the spectral element method (Patera, 1984; Maday & Patera, 1989; Bernardi & Maday, 1992). This method which stems from a variational formulation of the elastodynamics equations (Priolo *et al.*, 1994; Faccioli *et al.*, 1997; Komatitsch & Vilotte, 1998), combines the geometrical flexibility of conventional finite element methods with the exponential convergence rate associated with spectral techniques. It provides an optimal dispersion error and an accurate representation of surface and interface waves. The first problem in applying the spectral element method in global seismology is the paving of a 3-sphere using hexahedra, a natural element for efficient sum-factorization techniques. This was solved (Chaljub, 2000; Chaljub *et al.*, 2001) by first the tilling of embedded spherical interfaces in six quadrangular regions using the central projection (Sadourny, 1972; Ronchi *et al.*, 1996) of a cube onto the circumscribed spherical interface, then by inscribing a cube at the center of the sphere with a smooth transition between the six faces of the inner cube and the innermost spherical interface (Chaljub, 2000). Such a discretization is shown to provide an almost uniform tilling of the spherical interfaces and to avoid the pole problems and the singularity at the center of the sphere. Moreover, all the transformations can be defined analytically, and perturbed to map aspherical geometries or interface topographies. In contrast with finite differences, the spectral element method provides a natural setting for handling the connection between the six regions produced by the central projection. Spectral element can then be formulated in conjunction with a hybrid variational formulation (Chaljub, 2000; Chaljub *et al.*, 2001) allowing : an efficient coupling between solid and fluid domains at the core mantle boundary; a non conforming domain decomposition and mesh refinements with the help of the mortar method (Bernardi *et al.*, 1994; Ben Belgacem & Maday, 1994; Ben Belgacem, 1999). Such mesh refinement flexibility is crucial for an accurate representation of localized heterogeneities within a global model while reducing the computational cost. Coupled with an explicit second order predictor-corrector scheme in time, the method can be very efficiently parallelized on distributed memory architectures as shown in Chaljub *et al.* (2001). Even though this method should become one of the leading method for direct numerical simulation in global seismology, it still requires front end computational resources for realistic problems, typically 128 processors with more than 90 GB distributed memory for a dominant period of less than 30 seconds, which still preclude its use in a day to day basis.

It is worth noting that no one scheme can be expected to be optimal for the entire range of applications we might wish to consider in the context of global seismology. Within the actual limitation of the computer resources, beside few front end infrastructures, it is of importance to explore the possibility of combining the respective advantages of the spectral transform and spectral element methods for exploring some realistic 3D problems. We present here a new method that couple spectral element and normal mode summation methods. Such a coupled method actually allows the computation of

synthetic seismograms and wavefield propagation in laterally heterogeneous earth models down to periods of 30 seconds on a medium size parallel architecture, typically a cluster of 32 processors and 32 GB distributed memory. The underlying idea is that, with regard to the actual resolution of the broad-band records, it is quite reasonable to focus on the effect of lateral heterogeneities confined in an outer shell while the corresponding inner sphere is still approximated as spherically symmetric. Depending on the problem in hand, the outer heterogeneous shell can be mapped as the whole mantle, down to the CMB, or restricted to some portion of the upper mantle or to the crust. In this approach, a modal solution is sought for the inner sphere while the high-order spectral element solution is retained for the heterogeneous outer shell. The coupling between the spectral element method, formulated in space and time, and the modal summation method, formulated in frequency and wave-number, requires some original solution. Within the spectral element method, the a coupling is introduced via a dynamic interface operator, a Dirichlet-to-Neumann (DtN) operator, which can be explicitly constructed in frequency and generalized spherical harmonics. The inverse transform in space and time requires however an optimal asymptotic regularization. Such a coupling allows a significant speed-up in the simulation of the wavefield propagation and the computation of synthetic seismograms in laterally heterogeneous earth models. It is of interest to note here that in the coupled method the outer shell can be aspherical providing that the coupling interface remains a spherical interface. The interface can then be chosen to be an artificial coupling interface below the CMB. This still reduces significantly the computational requirements since the stringent CFL constrains come from the core discretization in the full spectral element method.

In this paper, we focus on the construction of the DtN operator which is the crucial part of the method and applications are restricted to spherical earth models for which we do have solutions to compare with. Applications to laterally 3D earth models are part of two companion papers (Capdeville *et al.*, 2002; Capdeville *et al.*, 2002). The paper is organized as follows. We first introduce the coupling method in a simple 1D example where the explicit calculation of the DtN operator is provided with several numerical examples to assess the accuracy of the method. We then explicit the construction of the DtN operator in the 3D case in conjunction with the spectral element method developed in Chaljub (2000) and Chaljub *et al.* (2001). Several numerical tests are performed in order to illustrate the accuracy of the method and the efficiency of the asymptotic regularization of the DtN operator. Then the method is used to compute the synthetic seismograms in the case of the PREM model and a simple example is provided for the SAW12D model. In conclusion, we outline some ongoing extensions especially for the study of the CMB zone.

2   PROBLEM STATEMENT AND EQUATION OF MOTION

We consider a spherical earth domain $\mathbf{\Omega}$, with the boundary $\partial\mathbf{\Omega}$ and internal radius $r_{\mathbf{\Omega}}$, see Fig. 1. The domain is decomposed in solid and fluid parts, $\mathbf{\Omega}_S$ and $\mathbf{\Omega}_F$ respectively, where the fluid part typically includes the outer core. We assume here for sake of simplicity that each of these subdomains is spherical with no interface between two fluid subdomains. The solid-solid interfaces are denoted Σ_{SS}, the solid-fluid interfaces Σ_{SF} and the set of all the interfaces Σ.

For a spherical non rotating earth model, the linearized momentum equation, around an initial hydrostatic state of equilibrium, is given by :

$$\rho(\mathbf{r})\frac{\partial^2\mathbf{u}(\mathbf{r},t)}{\partial t^2} - \mathcal{H}\mathbf{u}(\mathbf{r},t) = \mathbf{f}(\mathbf{r},t)\,, \tag{1}$$

where $\mathcal{H}$ is the elasto-gravity operator which, when neglecting the perturbation of the earth gravity potential, is given by :

$$\mathcal{H}\mathbf{u}(\mathbf{r},t) = \mathbf{\nabla}\cdot\left[\boldsymbol{\tau}(\mathbf{u}) - \mathbf{u}\cdot\mathbf{\nabla}\boldsymbol{\tau}^0\right] - \mathbf{\nabla}\cdot(\rho\mathbf{u})\mathbf{g}\,. \tag{2}$$

Here ρ is the initial density, $\mathbf{g}$ is the unperturbed gravity acceleration, $\mathbf{f}$ is a generalized source term and $\boldsymbol{\tau}^0$ the initial reference hydrostatic stress. The perturbed displacement $\mathbf{u}$ and the associated stress perturbation $\boldsymbol{\tau}$ have to satisfy the following continuity relations :

$$[|\mathbf{u}(\mathbf{r},t)|] = 0 \qquad \forall\mathbf{r}\in\Sigma_{SS}\,, \tag{3}$$

$$[|\mathbf{u}(\mathbf{r},t)\cdot\mathbf{n}(\mathbf{r})|] = 0 \qquad \forall\mathbf{r}\in\Sigma_{SF}\,, \tag{4}$$

$$[|\boldsymbol{\tau}(\mathbf{u})(\mathbf{r},t)\cdot\mathbf{n}(\mathbf{r})|] = 0 \qquad \forall\mathbf{r}\in\Sigma\,, \tag{5}$$

with the initial conditions

$$\mathbf{u}(\mathbf{r},0) = 0 \quad ; \quad \frac{\partial\mathbf{u}}{\partial t}(\mathbf{r},0) = 0 \qquad \forall\mathbf{r}\in\mathbf{\Omega}\,, \tag{6}$$

and the following free surface condition

$$\boldsymbol{\tau}(\mathbf{r},t).\mathbf{n}(\mathbf{r}) = 0 \quad \forall r\in\partial\mathbf{\Omega}\,, \tag{7}$$

where $\mathbf{n}(\mathbf{r})$ denotes the unit outward normal.

In the solid parts $\mathbf{\Omega}_S$, the elasto-gravity operator can be rewritten as :

$$\mathcal{H}\mathbf{u}(\mathbf{r},t) = \mathbf{\nabla}\cdot\boldsymbol{\tau}(\mathbf{u}) - \mathbf{\nabla}\cdot(\rho\mathbf{u})\mathbf{g} + \mathbf{\nabla}(\rho\mathbf{u}\cdot\mathbf{g})\,, \tag{8}$$

where for a linearly elastic medium, the Lagrangian stress perturbation is simply defined as :

$$\tau_{ij}(\mathbf{u})(\mathbf{r},t) = d_{ijkl}(\mathbf{r})u_{k,l}(\mathbf{r},t)\,, \tag{9}$$

with $u_{k,l} = \partial u_k/\partial x_l$ and d_{ijkl} is the elastic tensor with all the major and minor symmetries.

In the following, the lateral heterogeneities of interest are restricted within an outer spherical shell $\mathbf{\Omega}^+$ and only radial heterogeneities are retained within the inner sphere $\mathbf{\Omega}^-$. The interface between these two domains will be denoted $\mathbf{\Gamma}$. Even though such a partitioning might appear quite artificial, it has some practical interest. With regard to the actual resolution of the observations, it is quite reasonable, when studying the mantle lateral heterogeneities, to assume only radial heterogeneities within the earth core. The artificial boundary $\mathbf{\Gamma}$ can therefore be chosen at the core-mantle boundary or below the CMB. In the latter case, the earth model can be aspherical as far as the coupling boundary remains spherical. When focussing to the strong lateral heterogeneities within the crust, or the upper lithosphere, the interface $\mathbf{\Gamma}$ can be set somewhere within the mantle. The aim is to take advantage of the high order variational formulation, in space and time, only within the domain $\mathbf{\Omega}^+$, where strong lateral heterogeneities are assumed to be important depending on the problem in hand, while taking advantage of the modal summation method in $\mathbf{\Omega}^-$. This leads to a significant speed up in the computation of seismograms while retaining informations on the complicated wave propagation within the laterally heterogeneous parts. The coupling between the variational formulation of the elastodynamic problem, formulated in space and time, and the modal summation method, formulated in frequency and wave number, requires special attention. We first consider a simple 1-D scalar example to introduce the methodology and then extend it to more realistic 3D problems.

3 A ONE DIMENSIONAL EXAMPLE

We first consider, Fig. 2, a simple 1-D domain $\mathbf{\Omega}$ of length L. The domain is decomposed into two subdomains $\mathbf{\Omega}^- = [0, L_0]$ and $\mathbf{\Omega}^+ = [L_0, L]$. The interface between the two domains $\mathbf{\Gamma} = \{L\}$ is oriented by the unit outward normal $\mathbf{n_\Gamma}$, directed from the domain $\mathbf{\Omega}^-$ toward $\mathbf{\Omega}^+$. The interface $\mathbf{\Gamma}$ may be related to a physical discontinuity or not. The elastic medium is characterized by the density $\rho(x)$, the elastic parameter $\lambda(x)$ and the sound speed $c(x) = \sqrt{\lambda(x)/\rho(x)}$. The source condition is taken as a collocated point force, at $x = x_s \in \mathbf{\Omega}^+$, with $f = F\delta(x - x_s)g(t - t_0)$ where δ denotes the Dirac distribution, g a time wavelet centered at t_0 and F the amplitude of the force.

The problem involves only a scalar displacement field in the x-direction, $\mathbf{u}(x,t) = u(x,t)\mathbf{e}_x$ and the only non zero stress component $\tau(x,t) = \tau_{xx}(x,t) = \lambda(x)\partial u(x,t)/\partial x$. We introduce the restrictions u^+ and u^- of the displacement u to $\mathbf{\Omega}^+$ and $\mathbf{\Omega}^-$ respectively as $u^+(x,t) = u(x,t)$, $\forall x \in \mathbf{\Omega}^+$ and $u^-(x,t) = u(x,t)$, $\forall x \in \mathbf{\Omega}^-$.

The scalar wave equation $\forall x \in \Omega$ is :

$$\rho(x)\frac{\partial^2 u(x,t)}{\partial t^2} - \frac{\partial}{\partial x}\left(\lambda(x)\frac{\partial u(x,t)}{\partial x}\right) = f(x,t)\,, \tag{10}$$

with the initial conditions:

$$u(x, 0) = 0 \qquad \text{and} \qquad \frac{\partial u}{\partial t}(x, 0) = 0 \,, \tag{11}$$

and at both ends, a free-boundary condition is assumed:

$$T(0, t) = - \left. \lambda(x) \frac{\partial u(x, t)}{\partial x} \right|_{x=0} = 0 \,, \tag{12}$$

$$T(L, t) = \left. \lambda(x) \frac{\partial u(x, t)}{\partial x} \right|_{x=L} = 0 \,, \tag{13}$$

where $T(x, t) = \tau \cdot \mathbf{n}$ is the traction defined on the interface at position x with the unit outward normal vector $\mathbf{n}$. Across the solid-solid interface $\mathbf{\Gamma}$, the solution has to satisfy the continuity conditions of both displacement and traction :

$$[|u(L_0, t)|] = u_{\mathbf{\Gamma}}^+(t) - u_{\mathbf{\Gamma}}^-(t) = 0 \,, \tag{14}$$

$$[|T(L_0, t)|] = T_{\mathbf{\Gamma}}^+(t) - T_{\mathbf{\Gamma}}^-(t) = 0 \,, \tag{15}$$

where

$$u_{\mathbf{\Gamma}}^\pm(t) = \lim_{\epsilon \to 0, \epsilon > 0} u(L_0 \pm \epsilon, t) \qquad \text{and} T_{\mathbf{\Gamma}}^\pm(, t) = \lim_{\epsilon \to 0, \epsilon > 0} T(L_0 \pm \epsilon, t) \,,$$

In order to illustrate the coupling between the spectral element and the modal summation methods in this simple 1-D case, the problem will be solved using a spectral element approximation within the $\mathbf{\Omega}^+$ and a modal summation method within $\mathbf{\Omega}^-$. The coupling between the two solutions requires an explicit matching of the traction and displacement at the interface $\mathbf{\Gamma}$.

3.1   Variational formulation

The spectral element approximation of the scalar wave equation in the subdomain $\mathbf{\Omega}^+$, is first outlined. The solution u^+, i.e. the restriction of the solution u to the domain $\mathbf{\Omega}^+$, is searched in the space $H^1(\mathbf{\Omega}^+)$ of the square-integrable functions with square-integrable generalized first derivative. Introducing a time interval, $\mathbf{I} = [0, T]$, the solution belongs to the space $\mathcal{C}_t$ of the kinematically admissible displacements :

$$\mathcal{C}_t = \left\{ u(x, t) \in H^1(\mathbf{\Omega}^+) : \mathbf{\Omega}^+ \times \mathbf{I} \to \mathbb{R} \right\} \,. \tag{16}$$

The variational formulation of the problem (10)-(11) reads : find $u^+ \in \mathcal{C}_t$, such that $\forall t \in \mathbf{I}$ and $\forall w \in \mathcal{C}_t$

$$\left(w, \rho \frac{\partial^2 u^+}{\partial t^2}\right) + a\left(w, u^+\right) = (w, f) + \langle w, T^+(u^+)\rangle_{\mathbf{\Gamma}}, \tag{17}$$

$$\left(w, \rho u^+\right)\big|_{t=0} = 0, \tag{18}$$

$$\left(w, \rho \partial_t u^+\right)\big|_{t=0} = 0, \tag{19}$$

where $(\cdot, \cdot)$ is the classical L^2 inner product with

$$(w, u) = \int_{\mathbf{\Omega}^+} w \cdot u \, dx. \tag{20}$$

The bilinear form $a(\cdot, \cdot)$ defines the symmetric elastic strain-energy inner product :

$$a(w, w) = \int_{\mathbf{\Omega}^+} \tau(w) : \nabla w \, dx = \int_{\mathbf{\Omega}^+} \lambda \frac{\partial w}{\partial x} \frac{\partial w}{\partial x} \, dx, \tag{21}$$

and the bilinear form $\langle \cdot, \cdot \rangle_{\mathbf{\Gamma}}$ is defined as:

$$\langle w, T^+(u^+)\rangle_{\mathbf{\Gamma}} = \int_{\mathbf{\Gamma}} w \cdot T^+(u^+) \, dx = \left(w \cdot T^+(u^+)\right)\big|_{L_0}. \tag{22}$$

The last term involves the traction along the interface between the two subdomains $\mathbf{\Omega}^+$ and $\mathbf{\Omega}^-$. Taking into account the continuity conditions (14), and assuming that we are able to compute the solution that characterize the response of the domain $\mathbf{\Omega}^-$ to a prescribed displacement $u_{\mathbf{\Gamma}}^- = u_{\mathbf{\Gamma}}^+$ on the interface $\mathbf{\Gamma}$, the interface operator $\mathcal{A}$ will relate the traction T^- on $\mathbf{\Gamma}$ to that imposed displacement :

$$\mathcal{A} : T_{\mathbf{\Gamma}}^-(t) = \mathcal{A}(u_{\mathbf{\Gamma}}^-)(t), \tag{23}$$

where $\mathcal{A}$ is defined in terms of a convolution. With the continuity conditions (14), the interface operator relates directly the traction T^+ to the displacement u^+ on that side of the interface as a result of the dynamic behavior of the domain $\mathbf{\Omega}^-$:

$$\mathcal{A} : T_{\mathbf{\Gamma}}^+(t) = \mathcal{A}(u_{\mathbf{\Gamma}}^+)(t). \tag{24}$$

The interface operator $\mathcal{A}$ is a *Dirichlet to Neumann* (*DtN*) operator which, for a given displacement on the interface (Dirichlet condition), provides the associated traction (Neumann condition) on the interface. Such an operator was first introduced for absorbing boundary conditions (e.g. Givoli & Keller (1990) or Grote & Keller 1995). For the domain $\mathbf{\Omega}^+$, the *DtN* operator $\mathcal{A}$, defined on $\mathbf{\Gamma}$, acts as a dynamical boundary condition in traction.

3.2   Spatial discretization

In order to solve numerically the above problem, the physical domain $\mathbf{\Omega}^+$ is discretized, Fig. 2, into n_e non–overlapping elements $\mathbf{\Omega}_e$, $e = 1, \ldots, n_e$, such that $\mathbf{\Omega} = \cup_{e=1}^{n_e} \mathbf{\Omega}_e$. For each segment $\mathbf{\Omega}^e$,

an invertible local geometrical transformation $\mathcal{F}_e$ is defined which map the reference segment $\Lambda = [-1, 1]$ into $\mathbf{\Omega}_e$, i.e. $x(\xi) = \mathcal{F}_e(\xi)$, where ξ is a local reference coordinate system defined on Λ. In the 1D case, $\mathcal{F}_e$ is trivial to define, as well as its inverse.

In the following, the upper-script $^+$, for the restriction of u to the domain $\mathbf{\Omega}^+$, is dropped unless some possible confusion, and u_e^h denotes the restriction of u to the element $\mathbf{\Omega}^e$.

Associated with the spatial discretization of $\mathbf{\Omega}^+$, a piecewise-polynomial approximation of the kinematic admissible displacements is introduced :

$$\mathcal{C}_N^h = \left\{ u^h \in \mathcal{C}_t : u^h \in H^1(\mathbf{\Omega}^+) \quad \text{and} \quad u_e^h \circ \mathcal{F}_e \in \mathbb{P}_N(\Lambda) \right\}, \tag{25}$$

where $\mathbb{P}_N(\Lambda)$ is the set of the polynomials defined on Λ and of degree less than or equal to N, and $\circ$ is the functional composition symbol. The discrete solution u^h is therefore a continuous function such that its restriction to each element $\mathbf{\Omega}^e$ can be represented in terms of local polynomials after transformation to the reference element Λ. The spectral element approximation can be characterized by the total number of elements n_e and the polynomial degree N on the reference element Λ. The discrete variational problem then reads: find $u^h \in \mathcal{C}_N^h$, such that $\forall t \in \mathbf{I}$ and $\forall w^h \in \mathcal{C}_N^h$:

$$\left(w^h, \rho \frac{\partial^2 u^h}{\partial t^2} \right) + a\left(w^h, u^h \right) = \left(w^h, f \right) + \langle w^h, \mathcal{A}(u^h) \rangle_{\mathbf{\Gamma}}, \tag{26}$$

$$\left(w^h, \rho u^h \right)\Big|_{t=0} = 0, \tag{27}$$

$$\left(w^h, \rho \partial_t u^h \right)\Big|_{t=0} = 0. \tag{28}$$

The discretization is completed by the definition of a discrete inner product : a Gauss-Lobatto-Legendre (GLL) quadrature allows the computation of each element integral after transformation into the reference element Λ. This quadrature defines $N + 1$ integration points, $\{\xi_i^N, \ i = 0, N\}$, as the zeros of the polynomial $(1 - \xi^2) P_N'$ where P_N is the Legendre polynomial of degree N defined on Λ. The polynomial basis on Λ can now be defined by the Lagrange polynomials $\{h_i^N, \ i = 1, N\}$, associated with the GLL points, such that $h_i^N(\xi_j) = \delta_{ij}$, where δ is the Kronecker symbol. The value of the displacement at any arbitrary point $x \in \mathbf{\Omega}^e$ is obtained through a Lagrange interpolation,

$$u_e^h(x) = \sum_{i=0}^{i=N} h_i^N(\xi) u_i^e, \tag{29}$$

where $x = \mathcal{F}_e(\xi)$. The discrete displacement u^h is defined uniquely by its values u_e^i at the collocation points $\mathcal{F}_e(\xi_i)$ where ξ_i are the GLL integration points on Λ.

Expanding w^h as in (29), the discrete variational problem (26) is shown to be equivalent to the set of algebraic equations $\forall t \in \mathbf{I}$:

$$M \frac{\partial^2 U}{\partial t^2} = F^{ext} - F^{int}(U) + F^{DtN}(U), \tag{30}$$

where U is the displacement vector of all the displacements associated to the total number of integration points, e.g., defined as the set of all the integration points defined at the element level. The mass matrix M, the internal force vector $F^{int}(U)$, the source term F^{ext} results from the assembly of the element contributions M^e, $F^{int,e}$ and $F^{ext,e}$ according to the connectivity of each element with

$$M_{ij}^e = \sum_{e=1}^{e=n_e} \sum_{l=0}^{N} \left[h_i^N(\xi_l)\rho(\xi_l)h_j^N(\xi_l)\partial_\xi \mathcal{F}_e(\xi_l)\omega_l \right] , \tag{31}$$

$$F_i^{int,e} = \sum_{e=1}^{e=n_e} \sum_{l=0}^{N} \left[\lambda(\xi_l)\frac{\partial h_j^n}{\partial \xi}(\xi_l) \sum_{i=0}^{N} \left\{ \frac{\partial h_i^N}{\partial \xi}(\xi_l)u_i^e \right\} \left(\partial_\xi \mathcal{F}_e(\xi_l) \right)^{-1} \omega_l \right] , \tag{32}$$

$$F_i^{ext,e} = \sum_{e=1}^{e=n_e} \sum_{l=0}^{N} \left[h_i^N(\xi_l)f^e(\xi_l)\partial_\xi \mathcal{F}_e(\xi_l)\omega_l \right] , \tag{33}$$

where ω_l are the integration weights associated with the GLL quadrature. It is worth to note here that by construction the element mass matrix, and therefore the global mass matrix, is diagonal leading to fully explicit schemes in time and great computational efficiency. The same procedure can be apply to the DtN interface contribution which lead to a simple collocated expression in this simple 1D example.

The algebraic ordinary differential system (30) is solved in time using a classical Newmark scheme (Hughes, 1987) with an explicit predictor-corrector scheme. Such a time stepping is conditionally stable and requires that

$$\Delta t \leq \Delta t_C = C\frac{\mathrm{d}x}{\alpha} , \tag{34}$$

where $\mathrm{d}x$ is the size of the smallest grid cell, α the wave velocity and C the Courant number. The average size of a spectral element for a fixed size scales as n_e^{-1} while the minimum grid spacing between two Gauss-Lobatto-Legendre points within an element occurs at the edge and scales as N^{-2}. Therefore the critical time step $\Delta t_C \propto \mathcal{O}(n_e^{-1}N^{-2})$ and a compromise has to be found between the degree of the polynomial approximation and the number of elements. For the 1-D example, an empirical value of $C = 0.84$ has been found to provide stable results.

3.3   Construction of the *DtN* operator in the frequency domain

The construction of the *DtN* operator requires the solution of the scalar wave equation in $\mathbf{\Omega}^-$ assuming a Dirichlet boundary condition on the interface $\mathbf{\Gamma}$, i.e. $u_{\mathbf{\Gamma}}^-(t) = u_{\mathbf{\Gamma}}^+(t)$. This problem can be solved in the frequency domain, .i.e.

$$\omega^2 \rho(x)\hat{u}^-(x,\omega) + \frac{\partial}{\partial x}\left(\lambda(x)\frac{\partial \hat{u}^-(x,\omega)}{\partial x} \right) = 0 , \tag{35}$$

with the following boundary conditions :

$$\lambda(x)\frac{\partial \hat{u}^-}{\partial x}(x,\omega) = 0 \qquad \text{for} \quad x = 0\,,$$
$$\hat{u}^-_{\mathbf{\Gamma}}(\omega) = \hat{u}^+_{\mathbf{\Gamma}}(\omega) \quad \text{for} \quad x = L_0\,, \tag{36}$$

and where $\hat{u}$ is defined as :

$$\hat{u}(x,\omega) = \int_{-\infty}^{+\infty} u(x,t)e^{-i\omega t}\mathrm{d}t\,, \tag{37}$$

For a given frequency, the problem (35) has two solutions with only one satisfying the free boundary condition at $x = 0$. We denotes this solution $U(x,\omega)$ and the corresponding displacement and traction on the coupling interface, $\mathbf{\Gamma}$, $\mathcal{D}(\omega)$ where $\mathcal{T}(\omega)$ defined as :

$$\mathcal{D}(\omega) = U|_{\mathbf{\Gamma}}(\omega) \quad \text{and} \quad \mathcal{T}(\omega) = \lambda\frac{\partial U}{\partial x}\bigg|_{\mathbf{\Gamma}}(\omega)\,. \tag{38}$$

Solutions of the problem in $\mathbf{\Omega}^-$ are therefore of the form $\hat{u}(x,\omega) = a(\omega)U(x,\omega)$, where $a(\omega)$ is an excitation coefficient that may be determined from the Dirichlet boundary condition, corresponding to the continuity condition,

$$a(\omega) = \frac{\hat{u}^+_{\mathbf{\Gamma}}(\omega)}{\mathcal{D}(\omega)}\,, \quad \forall \omega \notin \Pi_d = \{\omega_n, n \in \mathbb{Z}\}\,, \tag{39}$$

where Π_d is the set of the eigenfrequencies ω_n for which $\mathcal{D}(\omega_n) = 0$. The actual traction on the coupling interface is given by :

$$\hat{T}^+(\omega) = \hat{T}^-(\omega) = a(\omega)\mathcal{T}(\omega) = \frac{\mathcal{T}(\omega)}{\mathcal{D}(\omega)}\hat{u}^+_{\mathbf{\Gamma}}(\omega)\,.$$

By definition, the *DtN* operator $\hat{\mathcal{A}}$ in the frequency domain is:

$$\hat{\mathcal{A}}(\omega) = \frac{\mathcal{T}(\omega)}{\mathcal{D}(\omega)}\,, \quad \forall \omega \notin \Pi_d\,. \tag{40}$$

Transforming back the traction in the time domain, using the causality, leads to :

$$T^+_{\mathbf{\Gamma}}(t) = \int_{-\infty}^{+\infty} \mathcal{A}(t-\tau)u^+_{\mathbf{\Gamma}}(\tau)\mathrm{d}\tau = \int_0^t \mathcal{A}(t-\tau)u^+_{\mathbf{\Gamma}}(\tau)\mathrm{d}\tau\,, \tag{41}$$

3.4   Computing the operator *DtN* in the time domain

The inverse transform of the *DtN* operator $\hat{\mathcal{A}}$ is not straightforward due to the singularities at all the frequencies in Π_d. The discrete spectrum, associated with these singular contributions, have first to be isolated from the continuous spectrum. Noting $\mathcal{A}'_n$ the Cauchy residual of $\hat{\mathcal{A}}$ at the eigenfrequencies ω_n, and using the continuity of $\mathcal{T}$

$$\mathcal{A}'_n = \lim_{\omega \to \omega_n}(\omega - \omega_n)\hat{\mathcal{A}}(\omega) = \mathcal{T}(\omega_n)\frac{\mathrm{d}\mathcal{D}}{\mathrm{d}\omega}\bigg|_{\omega_n}^{-1}\,. \tag{42}$$

The numerical computation of the derivative can be done using finite difference formula or more accurately using the kinetic energy as detailed in the appendix A:

$$\left.\frac{\mathrm{d}\mathcal{D}}{\mathrm{d}\omega}\right|_{\omega_n} = -\frac{2\omega_n I_1(\omega_n)}{\mathcal{T}(\omega_n)}, \tag{43}$$

where

$$I_1(\omega) = \int_0^{L_0} \rho(x) U^2(x,\omega)\,\mathrm{d}x, \tag{44}$$

and therefore to

$$\mathcal{A}'_n = -\frac{\mathcal{T}^2(\omega_n)}{2\omega_n I_1(\omega_n)}. \tag{45}$$

In practice, this requires an accurate computation of the kinetic energy I_1.

The *DtN* operator $\hat{\mathcal{A}}$ can be written as

$$\hat{\mathcal{A}}(\omega) = \underbrace{\sum_n \frac{\mathcal{A}'_n}{\omega - \omega_n}}_{\text{a}} + \underbrace{\left(\hat{\mathcal{A}}(\omega) - \sum_n \frac{\mathcal{A}'_n}{\omega - \omega_n}\right)}_{\text{b}}. \tag{46}$$

The inverse Fourier transform can be computed using Cauchy's theorem for the singular contributions (46.a) and a regular inverse numerical Fourier transform for the continuous contribution (46.b).

$$\mathcal{A}(t) = \underbrace{\sum_n \mathcal{A}'_n\,i\,e^{i\omega_n t}H(t)}_{\text{a}} + \underbrace{\frac{1}{2\pi}\int_{-\infty}^{\infty}\left(\hat{\mathcal{A}}(\omega) - \sum_n \frac{\mathcal{A}'_n}{\omega - \omega_n}\right)e^{i\omega t}\,\mathrm{d}\omega}_{\text{b}}. \tag{47}$$

where $H(t)$ is the Heaviside function. It is worth to note here that both contributions are in fact non causal and that the causality is only retrieve by summing up the two contributions.

3.5 Time regularization of the *DtN* operator

Due to the spectral element time discretization, the allowed maximum frequency is restricted to the Nyquist frequency ω_N. The corner frequency ω_c ($\omega_c < \omega_N$) of the source time function, defines implicitly a truncated *DtN* operator, $\hat{\mathcal{A}}_c(\omega) = \hat{\mathcal{A}} \circ \hat{\sqcap}(\omega)$, where

$$\hat{\sqcap}(\omega) = \begin{cases} 1 & \text{for } |\omega| \leq \omega_c \\ 0 & \text{for } |\omega| > \omega_c \end{cases}. \tag{48}$$

Since $\sqcap(t)$ is not a causal filter, $\hat{\mathcal{A}}_c$ is non causal and the inverse transform of the traction becomes :

$$T_{\mathbf{\Gamma}}^+(t) = (\mathcal{A}_c * u_{\mathbf{\Gamma}}^+)(t) = \int_0^{\infty} \mathcal{A}_c(t-\tau)u_{\mathbf{\Gamma}}^+(\tau)\mathrm{d}\tau, \tag{49}$$

but $u_{\mathbf{\Gamma}}^{+}(t)$ comes from the spectral element solution and is known only up to the current time step. The *DtN* operator has therefore to be regularized

$$\hat{\mathcal{A}}_r(\omega) = \hat{\mathcal{A}}(\omega) - \hat{\mathcal{C}}(\omega)\,, \tag{50}$$

where $\hat{\mathcal{C}}$ is an asymptotic approximation of $\hat{\mathcal{A}}$. At high frequencies, $\hat{\mathcal{A}}_r(\omega) \simeq 0$ and $\hat{\mathcal{A}}_r \circ \hat{\sqcap} \simeq \hat{\mathcal{A}}_r$ and the causality problem is avoided, and the traction can be computed as

$$T_{\mathbf{\Gamma}}^{+}(t) = \underbrace{(\mathcal{A}_r * u_{\mathbf{\Gamma}}^{+})(t)}_{\text{a}} + \underbrace{(\mathcal{C} * u_{\mathbf{\Gamma}}^{+})(t)}_{\text{b}}\,, \tag{51}$$

where the convolution term (51.a) is now well defined and the last term can be computed analytically.

Following Barry *et al.* (1988), $\hat{\mathcal{C}}$ can be constructed from the asymptotic solution of (35). We consider

$$\hat{u}^{-}(x,\omega) = e^{-i\omega\Phi(x)} \sum_{k\geq 0} u_k(x)(i\omega)^{-k}\,, \tag{52}$$

and for the stress:

$$\hat{\tau}^{-}(x,\omega) = e^{-i\omega\Phi(x)} \sum_{k\geq 0} \tau_k(x)(i\omega)^{-k+1}\,. \tag{53}$$

Assuming the normalization $\hat{u}_{\mathbf{\Gamma}}^{+}(\omega) = 1$, we have

$$u_k|_{\mathbf{\Gamma}} = \begin{cases} 1 & \text{pour } k = 0 \\ 0 & \text{pour } k \neq 0 \end{cases} \quad \text{and } \Phi_{\mathbf{\Gamma}} = 2n\pi,\ n \in \mathbb{Z}\,. \tag{54}$$

The second-order hyperbolic equation (35), is equivalent to a first-order hyperbolic system of equations in displacement and stress. Noting

$$\mathbf{y}(x,\omega) = \begin{pmatrix} \hat{u}^{-}(x,\omega) \\ \hat{\tau}^{-}(x,\omega) \end{pmatrix}\,, \tag{55}$$

the first-order system becomes :

$$\frac{\partial \mathbf{y}}{\partial x} = \mathbf{S}(x,\omega)\mathbf{y}\,, \tag{56}$$

with

$$\mathbf{S}(x,\omega) = \begin{pmatrix} 0 & \lambda(x)^{-1} \\ -\rho(x)\omega^2 & 0 \end{pmatrix}\,. \tag{57}$$

The solution $\mathbf{y}$ can be developed as

$$\mathbf{y}(x,\omega) = e^{-i\omega\Phi(x)} \sum_{k\geq 0} \mathbf{y}_k(x,\omega)(i\omega)^{-k}\,, \tag{58}$$

with

$$
\mathbf{y}_k(x,\omega) = \begin{pmatrix} u_k(x) \\ i\omega\tau_k(x) \end{pmatrix}.
\tag{59}
$$

In order to solve (56) as a perturbation problem, $\mathbf{S}$ is now developed in powers of $(i\omega)^{-1}$,

$$
\mathbf{S}(x,\omega) = \sum_{k\geq -1} \mathbf{S}_k(x,\omega)(i\omega)^{-k}.
\tag{60}
$$

In the 1D case, only $\mathbf{S}_{-1}$ is different from zero,

$$
\mathbf{S}_{-1}(x,\omega) = \begin{pmatrix} 0 & (i\omega\lambda(x))^{-1} \\ i\omega\rho(x) & 0 \end{pmatrix}.
\tag{61}
$$

Combining (55)–(56), (58) and (60), we get

$$
k = -1 \qquad (\mathbf{S}_{-1} + \Phi'\mathbf{I})\mathbf{y}_0 = 0,
\tag{62}
$$

$$
k \geq 0 \qquad (\mathbf{S}_{-1} + \Phi'\mathbf{I})\mathbf{y}_{k+1} = \mathbf{y}'_k - \sum_{j=0}^{j=k} \mathbf{S}_{k-j}\mathbf{y}_j,
\tag{63}
$$

where $\mathbf{I}$ is the identity matrix and " $'$ " denotes the x derivative. Equation (62) has a non-trivial solution if and only if $|\mathbf{S}_{-1}+\Phi'\mathbf{I}| = 0$ which means $\Phi'^2 - \frac{\rho}{\lambda} = 0$. The outgoing wave solution is $\Phi' = -\sqrt{\rho/\lambda}$ and from (62), we get

$$
\tau_0(x) = \rho\alpha u_0(x).
\tag{64}
$$

where α is the sound wave velocity. This condition is similar to the para-axial condition of order 0 of (Clayton & Engquist, 1977). After some manipulations, equation (63), for $k = 0$, gives

$$
\tau_1(x) = -(\rho\alpha)'\frac{\alpha}{2}u_0(x) + \rho\alpha u_1(x),
\tag{65}
$$

and, with $c_1 = -(\rho\alpha)'\alpha$, we obtain for $k = 1$,

$$
\tau_2(x) = \frac{\alpha}{2}\left(c'_1 - c_1\frac{(\rho\alpha)'}{\rho\alpha}\right)u_0(x) - \frac{\alpha}{2}(\rho\alpha)'u_1(x) + \rho\alpha u_2(x).
\tag{66}
$$

Setting $x = L_0$ in (64)–(66) and with the help of (54), we get a fourth order approximation of $\hat{\mathcal{C}}$:

$$
\hat{\mathcal{C}}(\omega) = \sum_{k=0}^{k=2} c_k \times (i\omega)^{-k+1},
\tag{67}
$$

with

$$
c_0 = \rho\alpha, \quad c_1 = -\frac{\alpha c'_0}{2}, \quad c_2 = \frac{\alpha}{2}\left(\frac{c_1 c'_0}{2c_0} - c'_1\right),
$$

where ρ, α and their derivatives are computed at $x = L_0^-$.

3.6   Validation tests of the coupled method

To validate the method, we performed several tests in two heterogeneous examples. In all cases, we compare the displacements, at three positions, obtained when using a full spectral element method and the coupled method. The difference between the two solutions, amplified by 100, is also shown.

In the first test, Fig. 3, the heterogeneity in Ω^- is smooth and can be represented using a fourth-order polynomial. All the terms in the expansion $\mathcal{C}$ are different from zero as shown in Fig. 4. The first term of the expansion $\propto (i\omega)$, is similar to a time derivation. When substracted from $\hat{\mathcal{A}}$, the regularized operator $\hat{\mathcal{A}}_r$ is closed to a filtered Dirac shape. The second term of the expansion $\propto (i\omega)^0$, is similar to a Dirac term. After substraction, the regularized $\hat{\mathcal{A}}_r$ get a filtered Heaviside shape. The third term of the expansion, $\propto (i\omega)^{-1}$, is similar to an integration. When substracted, all the non causal signal is now removed. The agreement between the coupled method and the spectral element solution solution, Fig. 5, is very good even at the coupling interface. The error is also shown as a function of the order of the expansion used to compute $\mathcal{C}$ in Fig. 6. For this smooth example, the third order term does not really improve the solution when compared to the second order approximation since the error is already of the order of the accuracy of the spectral element time stepping.

In a second test, we consider a rougher heterogeneity distribution, Fig. 7. In this case, the third order approximation is clearly more accurate even if the improvement is not that impressive due to the simplicity of the example.

It is worth to mention here, that even for these simple examples the coupled method leads to an interesting computational speed-up. Indeed, in the last example Fig. 7, the wave speed in Ω^- leads to a severe CFL condition for the full spectral element method. In contrast, the coupled method is only controlled by the far less stringent CFL condition in Ω^+. Such a computational speed-up will become clear when solving the elastodynamics equations in spherical earth models.

4   THREE DIMENSIONAL CASE

We now consider the case of a 3D spherical earth domain Ω with the surface boundary Ω. The lateral heterogeneities are restricted to be within the outer solid shell Ω^+, which may be composed itself of several subdomains, while the inner spherical domain Ω^- is assumed to be radially heterogeneous with solid and liquid subdomains. The coupling interface Γ between the outer shell and the inner spherical domain may be a physical interface, like the CMB, or an artificial interface somewhere within the mantle or the outer core.

The original elastogravity problem, within the outer shell Ω^+, is solved, in space and time, using the variational spectral element approximation. The explicit construction the *DtN* operator, on the

coupling interface $\boldsymbol{\Gamma}$, involves a modal solution within the inner spherical domain $\boldsymbol{\Omega}^-$. We focus on the actual coupling between the spectral element and the modal solution methods, and only sketch out the spectral element variational formulation in $\boldsymbol{\Omega}^+$ within the context of a conforming approximation, i.e. point-wise continuity conditions on the solid-solid Σ_{SS} and the solid-fluid Σ_{SF} interfaces associated with a conforming spatial discretization of $\boldsymbol{\Omega}^+$. In practice however, a more sophisticated non conforming spectral element approximation is used allowing mesh refinements both in the radial and lateral directions in order to resolve accurately the velocity and the geometry structures of realistic earth models. For a more thorough presentation of the non conforming spectral element approximation, in the context of global earth models, the readers are referred to Chaljub (2000) and Chaljub *et al.* (2001), where an efficient parallel implementation is also discussed in some details.

4.1   Variational approximation

We look now for a solution in the space of the kinematically admissible displacements,

$$\mathcal{C}_t = \left\{ \mathbf{u}(\mathbf{r}, t) \in H^1(\boldsymbol{\Omega}^+)^3 : \boldsymbol{\Omega}^+ \times \mathbf{I} \to \mathbb{R}^3 \right\}, \tag{68}$$

The problem to be solved is: find $\mathbf{u}^+ \in \mathcal{C}_t$, such that $\forall t \in \mathbf{I} = [0, T]$ and $\forall \mathbf{w} \in \mathcal{C}_t$

$$(\rho \frac{\partial \mathbf{u}}{\partial t^2}, \mathbf{w}) + a(\mathbf{u}^+, \mathbf{w}) - \langle \mathbf{T}_{\boldsymbol{\Gamma}}^+, \mathbf{w} \rangle_{\boldsymbol{\Gamma}} = (\mathbf{f}, \mathbf{w}), \tag{69}$$

$$\left. \left(\mathbf{w}, \rho \mathbf{u}^+ \right) \right|_{t=0} = 0, \tag{70}$$

$$\left. \left(\mathbf{w}, \rho \frac{\partial \mathbf{u}^+}{\partial t} \right) \right|_{t=0} = 0, \tag{71}$$

where $(\cdot, \cdot)$ is the classical L^2 inner product. The symmetric bilinear form $a(\cdot, \cdot)$ is now given by

$$a(\mathbf{u}^+, \mathbf{w}) = \int_{\boldsymbol{\Omega}^+} [\boldsymbol{\tau}(\mathbf{u}^+) : \boldsymbol{\nabla}(\mathbf{w})] \mathrm{d}\mathbf{x} + \int_{\boldsymbol{\Omega}^+} \rho \, \mathrm{sym} \left\{ (\mathbf{w} \cdot \mathbf{g}) \boldsymbol{\nabla} \cdot \mathbf{u}^+ - \mathbf{u}^+ \cdot \boldsymbol{\nabla}(\mathbf{w} \cdot \mathbf{g}) \right\} \mathrm{d}\mathbf{x}, \tag{72}$$

and

$$\langle \mathbf{T}_{\boldsymbol{\Gamma}}^+, \mathbf{w} \rangle_{\boldsymbol{\Gamma}} = \int_{\boldsymbol{\Gamma}} \left(\mathbf{T}_{\boldsymbol{\Gamma}}^+ \cdot \mathbf{w} \right) \mathrm{d}\mathbf{x}, \tag{73}$$

where sym denotes the symmetric part and $\mathbf{T}_{\boldsymbol{\Gamma}}^+ = \boldsymbol{\tau} \cdot \mathbf{n}|_{r=r_{\boldsymbol{\Gamma}}^+}$ is the traction on the spherical coupling interface $\boldsymbol{\Gamma}$.

The continuity conditions across the coupling interface $\boldsymbol{\Gamma}$, depend whether $\boldsymbol{\Gamma}$ is a solid-solid or solid-liquid interface :

$$\begin{aligned} \mathbf{T}_{\boldsymbol{\Gamma}}^+(\mathbf{r}, t) &= \mathbf{T}_{\boldsymbol{\Gamma}}^-(\mathbf{r}, t), \\ \mathbf{u}_{\boldsymbol{\Gamma}}^+(\mathbf{r}, t) &= \mathbf{u}_{\boldsymbol{\Gamma}}^-(\mathbf{r}, t), & \text{if } \boldsymbol{\Gamma} \text{ is a solid–solid interface,} \\ \mathbf{u}_{\boldsymbol{\Gamma}}^+(\mathbf{r}, t).\mathbf{n}_{\boldsymbol{\Gamma}}(\mathbf{r}) &= \mathbf{u}_{\boldsymbol{\Gamma}}^-(\mathbf{r}, t) \cdot \mathbf{n}_{\boldsymbol{\Gamma}}(\mathbf{r}), & \text{if } \boldsymbol{\Gamma} \text{ is a solid–fluid interface,} \end{aligned} \tag{74}$$

where $\mathbf{T}_{\boldsymbol{\Gamma}}^{\pm}$ and $\mathbf{u}_{\boldsymbol{\Gamma}}^{\pm}$ are the restrictions of $\mathbf{T}$ and $\mathbf{u}$ to $\boldsymbol{\Gamma}$ in $\boldsymbol{\Omega}^{\pm}$. Assuming a solution of the elasto-gravity

problem within the domain $\mathbf{\Omega}^-$, for a prescribed Dirichlet boundary condition along the interface $\mathbf{\Gamma}$, the *DtN* operator $\mathcal{A}$, that relates the displacement $\mathbf{u}_{\mathbf{\Gamma}}^-$ to the traction $\mathbf{T}_{\mathbf{\Gamma}}^-$, can be constructed. Taking into account the continuity equations, the *DtN* operator, for solid-solid coupling interface, is therefore:

$$\mathcal{A} \quad : \quad \mathbf{T}_{\mathbf{\Gamma}}^+(\mathbf{r}, t) = \mathcal{A}\left(\mathbf{u}_{\mathbf{\Gamma}}^+(\mathbf{r}, t)\right), \tag{75}$$

and for a solid–fluid interface,

$$\mathcal{A} \quad : \quad \mathbf{T}_{\mathbf{\Gamma}}^+(\mathbf{r}, t) = \mathcal{A}\left(\mathbf{u}_{\mathbf{\Gamma}}^+(\mathbf{r}, t) \cdot \mathbf{n}(\mathbf{r})\right). \tag{76}$$

4.1.1   Spatial discretization

The first step is to defined, in a Cartesian reference coordinate system, a spatial discretization of the outer shell $\mathbf{\Omega}^+$ into n_e non overlapping elements $\mathbf{\Omega}_e$ such that $\mathbf{\Omega} = \cup_{e=1}^{n_e} \mathbf{\Omega}_e$. The spectral element method puts the additional constraint that the spherical grid must be based on hexaedra. Furthermore, the spherical mapping should be as regular as possible and such that the elements of the mesh are not too distorted and the sampling of the grid-points as uniform as possible.

To satisfy the first constraint, we must be able, for each spherical interfaces of $\mathbf{\Omega}^+$, to tile a 2-sphere with quadrangles. This is achieved using the central projection of a cube onto its circumscribed sphere. Such a cubic-gnomic projection has been introduced by Sadourny (1972) and further extended by Ronchi *et al.* (1996) as the "cubed sphere". With the help of the central projection, the 2-sphere is decomposed into six regions isomorphic to the six faces of a cube. By choosing the coordinate lines within each region to be arcs of the great circles (see Fig. 8) six coordinate systems, with identical metrics, are obtained free of singularity.

With a constant angular distance between each great circles, a regular meshing of the six regions is defined in terms of deformed squares with uniform edge width. The surface mesh is quite uniform with a maximum distortion not exceeding 30% (Chaljub, 2000). The construction of a 3D mesh inside the spherical shell is then straightforward by simply radially connecting the quadrangles of two concentric discretized spherical interfaces. These interfaces can be mapped onto physical interfaces associated with radial discontinuities within the mantle. As a result, the spherical shell is discretized into regular hexaedra (see Fig. 9) and the associated geometrical transformation is known analytically (Chaljub *et al.*, 2001). It can be easily extended to take into account an interface topography. We refer to Chaljub *et al.* (2001) for more details and for the extension to the discretization of the whole sphere.

For each element $\mathbf{\Omega}_e$, an invertible geometrical transformation $\mathcal{F}_e$ can be defined allowing to map the reference cube $\Lambda \times \Lambda \times \Lambda$ into $\mathbf{\Omega}_e$, with $\Lambda = [-1, 1]$, such that $\mathbf{x}(\boldsymbol{\xi}) = \mathcal{F}_e(\boldsymbol{\xi})$ where $\boldsymbol{\xi} = (\xi_1, \xi_2, \xi_3)$ defines a local coordinate system associated with the reference unit cube.

Following the same steps than in the last section, we introduce a piecewise-polynomial approxi-

mation of the kinematic admissible displacements $\mathcal{C}_t$:

$$\mathcal{C}_N^h = \left\{ \mathbf{u}^h \in \mathcal{C}_t : \mathbf{u}^h \in H^1(\mathbf{\Omega}^+)^3 \quad \text{and} \quad \mathbf{u}_e^h \circ \mathcal{F}_e \in [\mathbb{P}_N(\Lambda)]^3 \right\}, \tag{77}$$

In the reference cube, $[\mathbb{P}_N(\Lambda)]^3$ is taken as the space generated by the tensor product of the polynomials of degree $\leq N$ in each of the three Cartesian directions. The discrete inner products involved in the variational formulation are constructed as the tensorial product of the 1-D Gauss-Lobatto-Legendre formulas in each of the local Cartesian directions ξ_1, ξ_2, ξ_3. This defines a grid of $(N+1)^3$ quadrature points. The piecewise polynomial approximation $\mathbf{u}_e^h$ of $\mathbf{u}$ is defined using the Lagrange interpolation associated with the grid composed of the Gauss-Lobatto-Legendre integration points. The Lagrange interpolants are therefore the tensor product of the one dimensional Lagrange interpolants. At the end of the discretization, the problem is reduced to an system of ordinary differential equations (30) in time which is solved by a classical Newmark algorithm.

4.2 *DtN* operator construction in the spectral and frequency domain

The construction of the *DtN* operator requires the solution of the elasto-gravity problem in the inner sphere $\mathbf{\Omega}^-$, assuming a Dirichlet boundary condition on the interface $\mathbf{\Gamma}$: $\mathbf{u}_\Gamma^- = \mathbf{u}_\Gamma^+$ for a solid-solid coupling or $\mathbf{u}_\Gamma^- \cdot \mathbf{n}_\Gamma = \mathbf{u}_\Gamma^+ \cdot \mathbf{n}_\Gamma$ for a solid-liquid coupling. For a spherically symmetric inner domain, the classical modal solution is computationally attractive. In the following, we outline the modal solution in the case of a solid-solid coupling. A similar solution can be found for the solid-liquid coupling case and only the explicit expression of the *DtN* operator in this case is given.

In the following, the domain $\mathbf{\Omega}^-$ is assumed to have a spherical symmetry. The problem can be formulated in the generalized spherical harmonics base (Phinney & Burridge, 1973), $\mathbf{e}_\alpha$, $\alpha \in \{-, 0, +\}$, defined as

$$\mathbf{e}_0 = \mathbf{e}_r, \quad \mathbf{e}_\pm = \frac{1}{\sqrt{2}}(\mp \mathbf{e}_\theta - i\mathbf{e}_\phi)$$

where $\mathbf{e}_r$, $\mathbf{e}_\theta$, $\mathbf{e}_\phi$ are unit vectors in the r, θ and ϕ directions. The fully normalized generalized spherical harmonics are denoted $Y_{\ell,m}^\alpha(\theta, \phi)$ where ℓ is the angular order, m the azimuthal order and α the component in the $\mathbf{e}_\alpha$ basis. The forward Legendre transformation of a given vector field $\mathbf{u}(\mathbf{r}, t)$ is defined by

$$\mathbf{u}_{\ell,m}(r, t) = \int_0^{2\pi} \int_0^\pi \mathbf{u}(r, \theta, \phi, t) \cdot \boldsymbol{\mathcal{Y}}_{\ell,m}^\star(\theta, \phi) \sin\theta \mathrm{d}\phi \mathrm{d}\theta. \tag{78}$$

where $\boldsymbol{\mathcal{Y}}_{\ell,m}$ is a tensor with components $[\boldsymbol{\mathcal{Y}}_{\ell,m}]_{\alpha\alpha'} = Y_{\ell,m}^\alpha \delta_{\alpha\alpha'}$ in the $\mathbf{e}_\alpha$ basis and $\boldsymbol{\mathcal{Y}}_{\ell,m}^\star$ its conjugate. The inverse Legendre transform is therefore

$$\mathbf{u}(\mathbf{r}, t) = \sum_{\ell,m} \mathbf{u}_{\ell,m}(r, t) \cdot \boldsymbol{\mathcal{Y}}_{\ell,m}(\theta, \phi), \tag{79}$$

where the sum over m extends from $-\ell$ to ℓ.

The momentum equation in the frequency domain is,

$$-\omega^2 \rho(\mathbf{r})\mathbf{u}^-(\mathbf{r}, \omega) - \boldsymbol{\mathcal{H}}(\mathbf{r})\mathbf{u}^-(\mathbf{r}, \omega) = 0 \,. \tag{80}$$

The solutions have to be regular at the origin $r = 0$, and must satisfy the Dirichlet condition at the coupling interface $\boldsymbol{\Gamma}$:

$$\mathbf{u}_{\boldsymbol{\Gamma}}^-(\mathbf{r}, \omega) = \mathbf{u}_{\boldsymbol{\Gamma}}^+(\mathbf{r}, \omega) \,. \tag{81}$$

Taking into account the spherical symmetry of $\boldsymbol{\Omega}^-$, we seek for a solution of of the form

$$\mathbf{u}^-(\mathbf{r}, \omega) = \mathbf{d}_{\ell,m}(r, \omega) \cdot \boldsymbol{\mathcal{Y}}_{\ell,m}(\theta, \phi) \,. \tag{82}$$

and the corresponding stress vector, defined on concentric spherical surfaces as $\mathbf{T}(\mathbf{r}, \omega) = \boldsymbol{\tau}(\mathbf{r}, \omega) \cdot \mathbf{e}_r$, is written as

$$\mathbf{T}^-(\mathbf{r}, \omega) = \mathbf{t}_{\ell,m}(r, \omega) \cdot \boldsymbol{\mathcal{Y}}_{\ell,m}(\theta, \phi) \,. \tag{83}$$

It is worth to mention here there is a one to one relation between this parameterization and the more classical one used for normal modes (e.g. Gilbert, 1971), where the solution is expressed as

$$\mathbf{u}^-(\mathbf{r}, \omega) = [U_{\ell,m}(r, \omega)\mathbf{e}_r + V_{\ell,m}(r, \omega)\boldsymbol{\nabla}_1 - W_{\ell,m}(r, \omega)(\mathbf{e}_r \times \boldsymbol{\nabla}_1)] Y_{\ell,m}^0(\theta, \phi) \,, \tag{84}$$

where $\boldsymbol{\nabla}_1$ is the gradient operator on the unit sphere. In the $\mathbf{e}_\alpha$-basis, we do have,

$$d_{\ell,m}^- = \frac{\zeta_\ell \gamma_\ell}{\sqrt{2}}(V_{\ell,m} - iW_{\ell,m}) \,,$$

$$d_{\ell,m}^0 = \zeta_\ell U_{\ell,m} \,, \tag{85}$$

$$d_{\ell,m}^+ = \frac{\zeta_\ell \gamma_\ell}{\sqrt{2}}(V_{\ell,m} + iW_{\ell,m}) \,,$$

where $\gamma_\ell = \sqrt{\ell(\ell + 1)}$ and $\zeta_\ell = \sqrt{(2\ell + 1)/4\pi}$.

Inserting (82) into (80) leads to two independent systems of second order differential equations in r degenerated for the azimuthal order m. The first system, spheroidal, is of order two, while the second, toroidal, is of order one (Takeuchi & Saito, 1972; Saito, 1988; Woodhouse, 1988). For a given ℓ and a fixed frequency ω, they are six independent solutions, four spheroidal ones and two toroidal ones, but only three of them satisfy the regularity condition at the origin : two spheroidal ones and one toroidal. These solutions are denoted $_q\mathbf{d}_\ell(r, \omega)$ with $q = \{1, 2, 3\}$.

The set of solutions $\{_q\mathbf{d}_\ell(r, \omega) \,, q = 1, 2, 3\}$ defines a complete basis for the displacement in $\boldsymbol{\Omega}^-$. The solution of the elasto-gravity equation (80) can therefore be written as :

$$\mathbf{u}_{\ell,m}^-(r, \omega) = \sum_q {}_qa_{\ell,m}(\omega){}_q\mathbf{d}_\ell(r, \omega) \,. \tag{86}$$

where $\{_q a_{\ell,m}(\omega)\}$, with $(\ell, m) \in \mathbb{N} \times [-\ell, \ell]$, are the excitation coefficients which have to be determined according to the Dirichlet boundary condition imposed on the coupling interface $\boldsymbol{\Gamma}$.

In the following, we note $\boldsymbol{\mathcal{D}}_\ell$ and $\boldsymbol{\mathcal{T}}_\ell$ the tensors defined in the $\mathbf{e}_\alpha$-basis by,

$$[\boldsymbol{\mathcal{D}}_\ell]^{q,\alpha}(\omega) = {}_q d_\ell^\alpha(r_{\boldsymbol{\Gamma}}, \omega), \quad [\boldsymbol{\mathcal{T}}_\ell]^{q,\alpha}(\omega) = {}_q t_\ell^\alpha(r_{\boldsymbol{\Gamma}}, \omega), \tag{87}$$

and $\tilde{a}_{\ell,m}$ the vector of components $[\tilde{a}_{\ell,m}]_q = {}_q a_{\ell,m}$. Taking into account the Dirichlet condition associated to the solid-solid coupling, we get

$$\tilde{a}_{\ell,m}(\omega) = \mathbf{u}_{\ell,m}^+(r_{\boldsymbol{\Gamma}}, \omega) \cdot \boldsymbol{\mathcal{D}}_\ell(\omega)^{-1} \qquad \forall\, (\ell, m, \omega),\ \omega \notin \Pi_\ell^d, \tag{88}$$

where Π_ℓ^d is the set of all eigenfrequencies for which $\boldsymbol{\mathcal{D}}_\ell$ is singular. It is worth to note here that, in contrast to the earth free oscillation problem, Π_ℓ^d is defined as the set of all the eigenfrequencies corresponding to an homogeneous Dirichlet boundary condition, see appendix B.

When $\tilde{a}_{\ell,m}(\omega)$ is known, the traction on the surface $\boldsymbol{\Gamma}$, on the $\boldsymbol{\Omega}^+$'s side, can be easily found using the continuity conditions :

$$\mathbf{T}_{\ell,m}^+(r_{\boldsymbol{\Gamma}}, \omega) = \mathbf{T}_{\ell,m}^-(r_{\boldsymbol{\Gamma}}, \omega) = \tilde{a}_{\ell,m}(\omega) \cdot \boldsymbol{\mathcal{T}}_\ell(\omega), \tag{89}$$

and therefore

$$\mathbf{T}_{\ell,m}^+(r_{\boldsymbol{\Gamma}}, \omega) = \mathbf{u}_{\ell,m}^+(r_{\boldsymbol{\Gamma}}, \omega) \cdot \boldsymbol{\mathcal{D}}_\ell(\omega)^{-1} \cdot \boldsymbol{\mathcal{T}}_\ell(\omega). \tag{90}$$

This explicitly defines the *DtN* operator :

$$\mathbf{T}_{\ell,m}^+(r_{\boldsymbol{\Gamma}}, \omega) = \boldsymbol{\mathcal{A}}_\ell(\omega) \cdot \mathbf{u}_{\ell,m}^+(r_{\boldsymbol{\Gamma}}, \omega) \qquad \forall \omega \notin \Pi_\ell^d, \tag{91}$$

where in the frequency–spectral domain

$${}^t\boldsymbol{\mathcal{A}}_\ell(\omega) = \boldsymbol{\mathcal{D}}_\ell^{-1}(\omega) \cdot \boldsymbol{\mathcal{T}}_\ell(\omega) \qquad \forall \omega \notin \Pi_\ell^d, \tag{92}$$

and ^{t} denotes the transposition. The *DtN* operator can be shown to be symmetric (see appendix B) and therefore, the transposition in expression (92) can be dropped.

In the case of a solid–fluid coupling interface $\boldsymbol{\Gamma}$, there is only one solution for (80) which satisfy the regularity condition at the origin. The tensors $\boldsymbol{\mathcal{D}}$ and $\boldsymbol{\mathcal{T}}$ reduce now to scalars $\mathcal{D}$ and $\mathcal{T}$. The expression of the *DtN* operator in the $\mathbf{e}_\alpha$-basis is given by:

$$[\boldsymbol{\mathcal{A}}_\ell(\omega)]^{\alpha\alpha'} = \mathcal{D}_\ell^{-1}(\omega)\mathcal{T}_\ell(\omega)\delta_{0,\alpha'}\delta_{0,\alpha}\ \ \forall \omega \notin \Pi_\ell^d. \tag{93}$$

4.3   Time and space regularization of the *DtN* operator

The spectral element approximation requires the interface traction $\mathbf{T}_\Gamma^+$ to be known in space and time,

$$\mathbf{T}_\Gamma^+(\mathbf{r}, t) = \sum_{\ell, m} \left[\int_0^t \boldsymbol{\mathcal{A}}_\ell(\tau) \cdot \mathbf{u}_{\ell, m}^+(r_\Gamma, t - \tau) \mathrm{d}\tau \right] \cdot \boldsymbol{\mathcal{Y}}_{\ell, m}(\theta, \phi) . \tag{94}$$

The sum over ℓ and m is the inverse Legendre Transform and the time integral involves a convolution. Numerically, the *DtN* operator requires a truncation both in the spherical harmonics expansion and in frequency. In order for the truncated problem to be well posed, it has to be regularized both in time and space. Such a regularization follows the same steps than in the 1D example.

The singularity contributions have first to be isolated as in (46). The Fourier transform can then be computed using Cauchy's theorem for the singular contributions and a regular Fourier transform for the continuous part. However, due to the truncature in frequency, $\boldsymbol{\mathcal{A}}_\ell(t)$ has to be regularized in order to circumvent the same causality problem that was encountered in the 1D example. This is done with the help of an asymptotic approximation $\boldsymbol{\mathcal{C}}_\ell(\omega)$, for the high frequencies, of the *DtN* operator $\boldsymbol{\mathcal{A}}$:

$$\boldsymbol{\mathcal{A}}_\ell^r(\omega) = \boldsymbol{\mathcal{A}}_\ell(\omega) - \boldsymbol{\mathcal{C}}_\ell(\omega) . \tag{95}$$

where $\boldsymbol{\mathcal{C}}_\ell(\omega)$ is given by :

$$\boldsymbol{\mathcal{C}}_\ell(\omega) = \sum_{j=0}^{j_{max}} \mathbf{c}_{\ell, j} \times (i\omega)^{-j+1} , \tag{96}$$

and the coefficients $\mathbf{c}_{\ell, j}$ can be explicitly computed, see appendix C for details. In practice, a third order approximation, $j_{max} = 2$, is required. The regularized *DtN* operator $\boldsymbol{\mathcal{A}}_\ell^r(\omega)$ is now causal and its inverse transform in space and time presents no difficulty. The traction on the coupling interface can be computed as :

$$\mathbf{T}_\Gamma^+(\mathbf{r}, t) = \sum_{\ell, m} \left[\int_0^t \boldsymbol{\mathcal{A}}_\ell^r(\tau) \cdot \mathbf{u}_{\ell, m}^+(r_\Gamma, t - \tau) \mathrm{d}\tau + \mathbf{c}_{\ell, 0} \cdot \mathbf{v}_{\ell, m}^+(r_\Gamma, t) + \mathbf{c}_{\ell, 1} \cdot \mathbf{u}_{\ell, m}^+(r_\Gamma, t) \right.$$
$$\left. + \mathbf{c}_{\ell, 2} \cdot \int_0^\tau \mathbf{u}_{\ell, m}^+(r_\Gamma, \tau) \mathrm{d}\tau \right] \cdot \boldsymbol{\mathcal{Y}}_{\ell, m}(\theta, \phi) , \tag{97}$$

where $\mathbf{v}^+$ is the first time derivative of $\mathbf{u}^+$. As shown in appendix C, $\mathbf{c}_{\ell, 0}$ corresponds to the Sommerfeld operator and does not depend on ℓ, i.e. $\mathbf{c}_{\ell, 0}$ is local in space, leading to :

$$\mathbf{T}_\Gamma^+(\mathbf{r}, t) = \mathbf{c}_{0,0} \cdot \mathbf{v}_\Gamma^+(\mathbf{r}_\Gamma, t) + \sum_{\ell, m} \left[\int_0^t \boldsymbol{\mathcal{A}}_\ell^r(\tau) \cdot \mathbf{u}_{\ell, m}^+(r_\Gamma, t - \tau) \mathrm{d}\tau + \mathbf{c}_{\ell, 1} \cdot \mathbf{u}_{\ell, m}^+(r_\Gamma, t) \right.$$
$$\left. + \mathbf{c}_{\ell, 2} \cdot \int_0^\tau \mathbf{u}_{\ell, m}^+(r_\Gamma, \tau) \mathrm{d}\tau \right] \cdot \boldsymbol{\mathcal{Y}}_{\ell, m}(\theta, \phi) . \tag{98}$$

The inverse Legendre transform in equation (94) or (98) requires to truncate the infinite sum over ℓ and m. The choice of the truncature ℓ_{max} is based directly on the dispersion curves Fig. 10 which

provides an upper angular order. Knowing the corner frequency of the spectral element approximation, a critical ℓ_c can be determined such that there is no eigenfrequency smaller than the corner frequency. Far enough from the source, the wave field has a maximum angular degree of ℓ_c and therefore $\ell_{max} = \ell_c$ provides an accurate approximation for the coupling. Such an estimation is only valid when the source is not too close to the coupling interface. When this is not the case, the choice $\ell_{max} = 2\ell_c$ has been found empirically to provide an accurate approximation.

Even though there is no causality problem induced by the space truncature, such a truncature is only well-posed for the lower-order spherical harmonics. The problem may be circumvented, as shown by Grote & Keller (1995), with the help of a spatially regularized operator $\mathcal{A}_\ell^s = \mathcal{A}_\ell - \mathcal{S}_\ell$:

$$\mathbf{T}_{\mathbf{\Gamma}}^+(\mathbf{r}, \omega) = \sum_{\ell=0}^{\ell_{max}} \sum_{m-\ell}^{+\ell} \mathcal{A}_\ell^s(\omega) \cdot \mathbf{u}_{\ell,m}^+(r_{\mathbf{\Gamma}}, \omega) \cdot \mathcal{Y}_{\ell,m}(\theta, \phi) + \mathcal{S}(\omega) \cdot \mathbf{u}^+(\mathbf{r}_{\mathbf{\Gamma}}, \omega) , \tag{99}$$

where $\mathcal{S}_\ell(\omega)$ may be any computationally efficient approximation of the *DtN* operator with the property : $\Im\langle \mathcal{S}\mathbf{u}, \mathbf{u}\rangle_{\mathbf{\Gamma}} < 0$, where $\Im$ denote the imaginary part. In practice for $\mathcal{S}_\ell(\omega)$, one can take the Sommerfeld operator:

$$\mathcal{S}_\ell(\omega) = i\omega \begin{pmatrix} \rho\beta & 0 & 0 \\ 0 & \rho\alpha & 0 \\ 0 & 0 & \rho\beta \end{pmatrix} . \tag{100}$$

where α and β are respectively the P- and S-wave velocities. The Sommerfeld operator is an absorbing boundary operator corresponding to the first order para-axial approximation (Clayton & Engquist, 1977). Therefore, all spurious waves, with spatial spectrum of angular order greater to ℓ_{max}, will not be transmitted by the regularized operator but actually absorbed, an interesting and stabilizing property. It is worth noting here that $\mathcal{S}_\ell(\omega) = i\omega\mathbf{c}_{\ell,0}$. Therefore the space regularization is already taken into account by the time regularization and (98) can be used directly to compute $\mathbf{T}_{\mathbf{\Gamma}}^+(\mathbf{r}, t)$ truncating the sum over ℓ to the appropriate ℓ_{max}.

5   VALIDATIONS TESTS OF THE 3D COUPLED METHOD

In this section, synthetic seismograms for a simple homogeneous sphere and the spherical earth model PREM (Dziewonski & Anderson, 1981) are computed and compared with the solution obtained by the summation of the free oscillations in order to test the accuracy of the method. In a homogeneous sphere, normal modes radial eigenfunctions are known analytically and eigenfrequencies are known up to the computer accuracy. In a spherically symmetric earth model, normal modes are known with a very good precision. Therefore, in both cases, the normal mode solution is a very accurate reference solution which allows for the validation of the coupled method.

In the homogeneous sphere test, only a solid–solid $\boldsymbol{\Gamma}$ interface is included. For the more realistic PREM test, the coupling interface $\boldsymbol{\Gamma}$ is set to be the CMB and includes a solid-liquid coupling.

5.1   Wave propagation in a homogeneous sphere

We consider a homogeneous solid sphere with a radius $r_{\boldsymbol{\Omega}} = 6371\,\text{km}$, a density $\rho = 3000\,\text{kg/m}^3$, a P-wave speed $\alpha = 8\,\text{km/s}$ and a S-wave speed $\beta = 6\,\text{km/s}$. The position of the solid-solid coupling interface $\boldsymbol{\Gamma}$ is set to $r_{\boldsymbol{\Gamma}} = 3471\,\text{km}$. The overall thickness of the outer spherical shell $\boldsymbol{\Omega}^+$ is $2500\,\text{km}$. Each of the 6 regions of $\boldsymbol{\Omega}^+$ are discretized with 8×8 elements horizontally and 2 elements vertically (see Fig. 11), with a total number of 768 elements.

In each element, the polynomial approximation is of degree $N = 8$, which set a total number of 559872 grid points in $\boldsymbol{\Omega}^+$. The shortest distance between two grid points is $38\,\text{km}$, which, for a Courant number of 0.4, leads to a maximal time step of $1.9\,\text{s}$. In the numerical experiment, the actual time step is $0.5\,\text{s}$ which is quite conservative.

For the source, the lowest period of the wavelet time function has been set to $125\,\text{s}$ which, for a wave speed of $5\,\text{km/s}$ (the approximate Rayleigh wave group velocity in this model), insures less than two wavelengths per element. The wavelet time function, Fig. 12, is a Ricker with a central frequency $1/312\,\text{Hz}$ and a corner frequency of $1/125\,\text{Hz}$. The source is an explosion of amplitude $10^{20}\,\text{kg}\,\text{m/s}^2$ and three different source depths are used:

(i) source A: at $398\,\text{km}$ depth. The source is very closed, compared to the wavelength to the free surface and provides a good test for the spectral element accuracy in the case of strong surface waves.

(ii) source B: at $1048\,\text{km}$ depth.

(iii) source C: at $2298\,\text{km}$ depth. The source is now very closed to, compared to the wavelength, the coupling interface $\boldsymbol{\Gamma}$ and provides a good test for the accuracy of the coupling when $\boldsymbol{\Gamma}$ is in the near field range.

In all these numerical experiments, $\ell_{max} = 37$, but for sake of security, we choose $\ell_{max} = 47$ for source A and B and $\ell_{max} = 119$ for source C, in order to capture with the near field. The explosion has been chosen for its symmetric radiation pattern, but a test with non diagonal moment tensor is also presented to check the transverse component and a more realistic source.

Snapshots of the wave propagation in $\boldsymbol{\Omega}^+$ are shown in a crossection, Fig. 13, for the source B. At $t = 660\,\text{s}$, the central time of the source time function is $400\,\text{s}$, the P-wave start to be absorbed by the *DtN* operator, without any visible spurious reflection. At 1035 s, the pP wave start now to be absorbed by the *DtN* operator. At 1551 s the P-wave emerges from $\boldsymbol{\Omega}^-$ into $\boldsymbol{\Omega}^+$. The X phase, a superposition

of higher spheroidal modes, is strongly excited by the source B. The Rayleigh wave, which is weakly excited due to the depth of the source, is however visible on the snapshots.

Traces, of the vertical component of the displacement, are also recorded on the surface as a function of the epicentral distance, Fig. 14. Despite the depth of the source, the Rayleigh wave is clearly visible. The Rayleigh wave is almost non dispersive for this frequency source range : a small dispersion is only observed, and accurately modeled, for the lowest frequencies as expected theoretically. The X-phase, which corresponds in terms of body waves to a superposition of P-wave subsurface reflections, is strongly excited. This phase is quite dispersive as expected theoretically and the dispersion is accurately modeled. Finally the P-wave is clearly observed as well as some several multiples PP, PPP, ... It is worth to note that this multiples tend slowly towards the X phase.

No spurious phase can be observed on Fig. 13 and 14. However, in order to assess the accuracy of the simulation, a direct comparison between the results obtained with the coupled method, for the three source positions, and the reference solution obtained by the normal modes summation is shown on Fig. 15. In each case the residual, i.e. the difference between the two solutions, has been multiplied by a factor ten. The agreement between the two solutions is indeed very good, with less than 1% of error. Surface waves, which are strongly excited in the case of the the source A, are very accurately modeled by the spectral element method, as well as the body waves (P- and S-waves) recorded directly on the coupling interface Γ, which is an especially difficult test for this method and clearly show that the DtN operator accurately capture the response of the inner sphere for all the phases. The same accuracy is achieved on the transverse component with a moment tensor ($M_{rr}=M_{\theta\theta}=M_{\phi\phi}=M_{r\theta}=0$ and $M_{r\phi}=M_{\theta\phi}=1$) using the source B location (Fig. 16).

5.2   Wave propagation in PREM

We consider the spherically symmetric reference earth model PREM. The coupling interface Γ is set at the CMB. The spectral element outer shell Ω^+ includes the whole mantle and the crust. This is in fact a quite challenging problem for the spectral element method due to the crustal structure inherent to the PREM model. The crust is characterized by slow wave velocities and the presence of very thin piecewise homogeneous layers with sharp elastic property contrasts: 15 and 10 km for the two uppermost layers. In the vertical direction, each of these concentric layers has to match with an element boundary in order to correctly approximate those contrasts. This drastically reduce the minimum size of the elements, in the vertical direction, and therefore put stringent constraints on the time step which must fulfill the CFL condition. Since each of these layers are piecewise homogeneous, the problem can be partly improved when using a very low vertical polynomial degree, a degree 2, within these crustal layers while retaining a degree 8 in the lateral directions. The time step imposed by the vertical

structure of the crust in PREM is of the order of $0.29\,$s. The slow wave velocities in the crust imply laterally a good spatial resolution in order to accurately represent the surface waves.

The mesh used in this example is built in order to match the nine surfaces of discontinuity in the mantle that are included in PREM. The mesh is non conforming (Chaljub *et al.*, 2001) in the vertical direction. In the lateral direction, 32 elements are used in the upper mantle and 16 elements in the crust. The non conforming interface is set at the $660\,$km transition zone. Such a mesh allow for a uniform CFL condition all through the mantle. This mesh could theoretically support a corner frequency of $1/45\,$Hz, but the actual corner frequency used in this example is $1/48\,$Hz, Fig. 18. The source is still explosive, for sake of simplicity, and its location is at $169\,$Km.

The vertical component of the displacement recorded at the surface, for PREM, is shown on Fig. 19 as a function of time and of the epicentral distance. In order to identify some of the body wave phases, time arrivals of various phases have been computed by an asymptotic ray tracing, as shown on Fig. 20 and superimposed on the synthetic seismograms of Fig. 19. The comparison between the time arrivals, derived from a high frequency approximation and a full wave form modeling, derived from a direct numerical simulation, is not that obvious due to finite frequency effects on the whole wave form, especially for body waves. Actually the notion of the "arrival time" only makes sense within the high frequency approximation. As a matter of fact, as for the P-wave, the ray tracing arrival time points sometimes to the maximum of the phase amplitude, in which case the agreement appears quite good, while sometimes it points to the minimum of the phase amplitude, or to a change of sign, mixing of different phases ... Obviously full waveforms obtained by direct numerical simulation does contain much more informations than traditional arrival time analysis based on asymptotic theories. However for the subject of this paper, such a comparison does not allow to assess the accuracy of the coupled method. A more thorough discussion of these results in the case of PREM and other laterally heterogeneous earth models will part of a forthcoming paper.

The accuracy can be assessed by a direct comparison between the synthetic seismograms obtained by the proposed direct numerical simulation and the classical normal modes summation method. Such a comparison is shown on Fig. 21 and Fig. 22 where displacements are recorded at the free surface and on the coupling interface, actually the CMB, for three different epicentral distances. The residual between the two solutions, amplified by a factor 10, does show a very good agreement, even when the displacement is recorded on the coupling interface. This clearly show that the DtN operator, corresponding in this case to a solid-fluid interface, accurately model the response of the earth core, for all the wave phases.

Interestingly enough, one should note here that if the PREM example was solved by a full spectral element approximation (Chaljub *et al.*, 2001), the geometry and the velocity structures of the inner core

would put stringent constraint on the time step. This is completely removed here in the coupled method since the core domain is now solved by a modal summation technique. Typically for large problems, such as the PREM example, the construction of the DtN operator and the coupling represents less than 13% of the whole CPU time. With the mesh used in this example and a corner frequency of $1/45$ Hz, a simulation over 3050 s, e.g. 12200 time steps, requires 30 hours on a cluster of 32 processors Pentium IV 900 MHz with 16 GB distributed memory and further minor optimizations should allow to reduce by a factor 1/3 the requested memory.

Fully 3D validation tests are very difficult to set up because a reference solution is missing in that case. Nevertheless some comparisons with method based upon approximation can be performed in the condition of validity of the approximation. Such a comparison with first order normal mode perturbation (Born approximation) has been attempted in Capdeville *et al.* (2002) and shows very good agreement when the heterogeneity velocity contrasts is weak .

6   CONCLUSIONS

A new method which couple a spectral element with a modal summation method for simulating 3-D seismic wave propagation in non rotating elastic earth models has been presented. The strategy is to decompose the earth model into a 3D heterogeneous outer shell and an inner sphere that is restricted to be spherically symmetric. The two domains are therefore connected through a spherical coupling interface that may be either a physical interface or an artificial one. Depending on the problem, the outer shell can be mapped either as the whole mantle or restricted to some portion of the upper mantle or the crust.

In the outer heterogeneous shell, the solution is sought in terms of the spectral element method based on a high order variational formulation in space and a fully second-order explicit time discretization. Within the inner sphere, the solution is sought in terms of a modal summation in the frequency domain after expansion of the space variable into the generalized spherical harmonics basis. The spectral element method combines the geometrical flexibility of classical finite element method with the exponential convergence rate associated with spectral techniques. Classical pole problems are avoided by tilling the spherical interfaces with six rectangular regions that can be easily mapped to rectangles. This is accomplished using the central or gnomic projection. The six regions can be further divided into quasi-uniform rectangular elements. The surface discretizations are then connected radially to build the 3D mesh of the outer shell. An essential feature of the spectral element method is that it can resolve sharp localized variations, as well as topographical features along the interfaces. High resolution can be obtained using mesh refinements with a non conforming discretization. The coupling with the modal summation method is achieved in the spectral element method by introducing a dynamic

coupling operator, the DtN operator, which can be explicitly constructed in the frequency/wavenumber domain. This allows to significantly speed up the computation. The key point here is the inverse transformation in the space-time domain of the coupling operator. This requires special attention and a suitable asymptotic regularisation. This is fully detailed for both a simple 1D example and 3D earth models.

The effectiveness of the method is then demonstrated for both the simple 1D example and 3D cases: a homogeneous elastic sphere and the PREM model. For spherically symmetric earth model, the method is shown to have most of the accuracy of spectral transform methods. However, the method has the advantage of allowing the resolution of wavefield propagation in a 3D laterally heterogeneous model for the same computational cost and without any perturbation hypothesis. Applications to 3D laterally heterogeneous earth models has already been performed and will be detailed in a forthcoming paper. The method has been highly parallelized on distributed memory architecture, both for the spectral element and the modal summation part, as detailed in Capdeville (2000), Chaljub (2000) and Chaljub, Capdeville, & Vilotte (2001). The coupled method allows to speed up the computation and makes the simulation of seismic wavefield in earth models down to 30 seconds possible today on a medium size parallel architecture such as a cluster of 32 processors with 32 GB of memory. This is in contrast with the more demanding full spectral element approximation, as detailed in Chaljub, Capdeville, & Vilotte (2001), even though the last approach is more general. The gain in memory and time computing obtain by using the coupled method compared to full spectral elements is strongly dependent on the Earth model, location on the *DtN* and frequency range. In cases presented in this paper, the gain obtain by the coupled method is the not sufficient to justify the coupled method (less that a factor two on both memory ans time computing). But there are cases, like the simulation in 3D D" models at period under 10s (Capdeville *et al.*, 2002), where the coupled method is the only option with a gain of more than 10 in memory (machine necessary to do the same thing with only spectral elements are not available), which fully justified the coupled method.

It is worth noting that no one scheme can be expected to be optimal for the entire range of applications we might wish to consider in the context of seismology. The method presented here is therefore a first step toward efficient direct numerical simulation methods for wavefield propagation and synthetic seismograms for some applications in global seismology. Extensions are already actually under study. Among them, it is worth to mention the incorporation of realistic surface topographies and the implementation of a spectral element strip between two domains in which the solution is sought via a modal summation technique. The latter will allow the study of highly localized heterogeneities in the vicinity of some interfaces like the core-mantle boundary at relatively high frequencies (Capdeville *et al.*, 2002).

7   ACKNOWLEDGMENTS

8   REFERENCES

Aki, K., 1981. Attenuation and scattering of short-period seismic waves in the lithosphere. In E. Husebye & S. Mykkeltveit (Eds.), *Identification of Seismic sources– earthquake or underground explosion*, pp. 515–541. Dordrecht: Reidel.

Alterman, Z., Aboudi, J. & Karal, F., 1970. Pulse propagation in a laterally heterogeneous solid elastic sphere. *Geophys. J. R. Astr. Soc.*, **21**, 243–260.

Barry, A., Bielak, J. & MacCamy, R. C., 1988. On Absorbing Boundary Conditions for Wave Propagation. *J. Comput. Phys.*, **79**, 449–468.

Bayliss, A., Jordan, K., LeMesurier, B. & Turkel, E., 1986. A fourth-order accurate finite difference scheme for the computation of elastic waves. *Bull. Seism. Soc. Am.*, **76**, 1115–1132.

Ben Belgacem, F., 1999. The mortar finite element method with Lagrange multipliers. *Num. Math*, **84**, 173–197.

Ben Belgacem, F. & Maday, Y., 1994. A spectral element methodology tuned to parallel implementations. *Comput. Methods Appl. Mech. Engrg.*, **116**, 59–67.

Bernardi, C. & Maday, Y., 1992. *Approximations spectrales de problèmes aux limites elliptiques*. Paris: Springer-Verlag.

Bernardi, C., Maday, Y. & Patera, A. T., 1994. A new nonconforming approach to domain decomposition: the mortar element method. In H. Brezis & J. Lions (Eds.), *Nonlinear Partial Differential Equations and Their Applications*, pp. 13–51. New York: Pitman and Wiley.

Capdeville, Y., 2000. *Méthode couplée éléments spectraux – solution modale pour la propagation d'ondes dans la Terre à l'échelle globale*. Ph. D. thesis, Université Paris 7.

Capdeville, Y., Larmat, C., Vilotte, J. P. & P., M. J., 2002. Numerical simulation of the scattering induced by a localized plume-like anomaly using a coupled spectral element and modal solution method. *Geophys. Res. Lett.*, in press.

Capdeville, Y., Romanowicz, B. & To, A., 2002. Coupling spectral elements and modes in a spherical earth: an extension to the "sandwich" case. *Geophys. J. Int.*. submitted.

Chaljub, E., 2000. *Modèlisation numérique de la propagation d'ondes sismiques à l'échelle du globe*. Ph.D. Thesis, Université Paris VII.

Chaljub, E., Capdeville, Y. & Vilotte, J., 2001. Solving elastodynamics in a solid heterogeneous 3-Sphere: a spectral element approximation on geometrically non-conforming grids. *J. Comp. Physics*. submitted.

Chaljub, E. & Tarantola, A., 1997. Sensitivity of SS precursor to topography on the upper–mantle 660-km discontinuity. *Geophys. Res. Lett.*, **24**, 2613–2616.

Chevrot, S., Montagner, J. & Sneider, R., 1998a. Corrigendum, 'The spectrum of tomographic models. *Geophys. J. Int.*, **135**, 311.

Chevrot, S., Montagner, J. & Sneider, R., 1998b. The spectrum of tomographic earth models. *Geophys. J. Int.*, **133**, 733–788.

Clayton, R. & Engquist, B., 1977. Absorbing boundary conditions for acoustic and elastic wave equations. *Bull. Seismol. Soc. Am.*, **67**, 1529–1540.

Clévédé, E., Mégnin, C., Romanowicz, B. & Lognonné, P., 2000. Seismic waveform modeling and surface wave tomography in a three-dimensional earth: asymptotic and non-asymptotic approaches. *Phys. Earth Planet. Int.*, **119**, 37–56.

Cummins, P., Geller, R., Haori, T. & Takeuchi, N., 1994. DSM complete synthetic seismograms: SH, spherically symmetric case. *Geophys. Res. Lett.*, **21**, 533–536.

Cummins, P., Geller, R. & Takeuchi, N., 1994. DSM complete synthetic seismograms: P-SV, spherically symmetric case. *Geophys. Res. Lett.*, **21**, 1663–1666.

Cummins, P. R., Takeuchi, N. & Geller, R. J., 1997. Computation of complete synthetic seismograms for laterally heterogeneous models using the Direct Solution Method. *Geophys. J. Int.*, **130**, 1–16.

Dablain, M., 1986. The application of high-order differencing to the scalar wave equation. *Geophysics*, **51**, 54–66.

Dahlen, F., 1969. The normal modes of a rotating elliptical Earth. *Geophys. J. R. Astr. Soc.*, **18**, 397–436.

Dahlen, F. A. & Tromp, J., 1998. *Theoretical Global Seismology*. Princeton University Press. NJ.

Ding, X. & Helmberger, D., 1997. Modeling D" structure beneath Central America with broadband seismic data. *Phys. Earth. Planet. Int.*, **101**, 245–270.

Dziewonski, A., 1995. Global seismic tomography of the mantle. *Rev. Geophys.*, **33**, 419–423. Supplement.

Dziewonski, A. M. & Anderson, D. L., 1981. Preliminary reference Earth model. *Phys. Earth Planet. Inter.*, **25**, 297–356.

Faccioli, E., Maggio, F., Paolucci, R. & Quarteroni, A., 1997. 2D and 3D elastic wave propagation by a pseudospectral domain decomposition method. *J. Seismology*, **1**, 237–251.

Finlayson, B., 1972. *The Method of Weighted residuals and variational principles*. New-York: Academic Press.

Fornberg, B., 1988. The pseudospectral method: accurate representation of interfaces in elastic wave calculations. *Geophysics*, **53**, 625–637.

Fornberg, B., 1995. A pseudospectral approach for polar and spherical geometries. *SIAM J. Sci. Comp.*, **16**, 1071–1081.

Fornberg, B., 1996. *A practical guide to Pseudospectral methods*. New York: Cambridge Univ. Press.

Friederich, W., 1998. Propagation of seismic shear and surface waves in a laterally heterogeneous mantle by multiple forward scattering. *Geophys. J. Int.*.

Friederich, W. & Dalkolmo, J., 1995. Complete synthetic seismograms for a spherically symmetric eath by a numerical computation of the Geen's function in the frequency domain. *Geophys. J. Int.*, **122**, 537–550.

Furumura, M., Kennett, B. & Furumura, T., 1999. Seismic wavefield calculation for laterally heterogeneous Earth models – II. The influence of upper mantle heterogeneity. *Geophys. J. Int.*, **139**, 623–644.

Furumura, T., Kennett, B. & Takenaka, H., 1998. Parallel 3-D pseudospectral simulation of seismic wave propagation. *Geophysics*, **63**, 279–288.

Gelfand, I., Monlos, R. & Shapiro, Z., 1963. *Representations of the rotation group and Lorentz groups and their applications*. New York: MacMillan.

Geller, R. & Ohminato, T., 1994. Computation of synthetic seismograms and their partial derivatives for heterogeneous media with arbitary natural boundary conditions using the Direct Solution Method. *Geophys. J. Int.*, **116**, 421–446.

Gilbert, F., 1971. Excitation of normal modes of the earth by earthquake sources. *Geophys. J. R. Astron. Soc.*, **22**, 223–226.

Givoli, D. & Keller, J., 1990. Non-reflecting boundary conditions for elastic waves. *Wave Motion*, **12**, 261–279.

Grand, S., VanDerHilst, R. & Widiyantoro, S., 1997. Global seismic tomography: A snapshot of convection in the earth. *Geol. Soc. Am. Today*, **7, No.4**, 1–7.

Grote, M. J. & Keller, J., 1995. On Nonreflecting Boundary Conditions. *J. Comput. Phys.*, **122**, 231–243.

Hara, T., Tsuboi, S. & Geller, R., 1993. Inversion for laterally heterogeneous upper mantle S-wave velocity structure using iterative waveform inversion. *Geophys. J. Int.*, **115**, 667–698.

Heikes, R. & Randall, D., 1995. Numerical integration of the shallow-water equations on a twisted icosahedral grid. Part II: A detailed description of the grid and an analysis of numerical accuracy. *Mon. Wea. Rev.*, **123**, 1881–1887.

Hughes, T. J. R., 1987. *The finite element method, linear static and dynamic finit element analysis*. Englewood Cliffs, NJ; Prentice–Hall International.

Igel, H., Takeuchi, N., Geller, R., Megnin, C., Bunge, H. P., Clévédé, E., Dalkomo, J. & Romanowicz, B., 2000. The COSY Project: verification of global seismic modeling algorithms. *Phys. Earth Planet. Inter.*, **119**, 3–23.

Igel, H. & Weber, M., 1996. P-SV wave propagation in the Earth's mantle using finite-differences: application to heterogeneous lowermost mantle structure. *Geophys. Res. Lett.*, **23**, 731–734.

Jakob-Chien, R. & Alpert, B., 1997. A fast spherical filter with uniform resolution. *J. Comp. Phys*, **136**, 580–584.

Kelly, K., Ward, R., Treitel, S. & Alford, R., 1976. Synthetic seismograms: a finite difference approach. *Geophysics*, **41**, 2–27.

Kendall, J. & Silver, P., 1996. Constraints from seismic anisotropy on the nature of the lowermost mantle. *Nature*, **381**, 409–412.

Kennett, B., 1997. Observational and theoretical constraints on crustal and upper mantle. *Phys. Earth. Planet. Int.*, **47**, 319–332.

Kennett, B. & Bowman, J., 1990. The velocity structure and heterogeneity of the upper mantle. *Phys. Earth. Planet. Int.*, **59**, 134–144.

Komatitsch, D. & Vilotte, J. P., 1998. The spectral element method: an effective tool to simulate the seismic response of 2D and 3D geological structures. *Bull. Seism. Soc. Am.*, **88**, 368–392.

Kosloff, D., Kessler, D., Filho, A., Tessmer, E., Behle, A. & Strahilevitz, R., 1990. Solution of the equations of dynamics elasticity by a Chebyshev spectral method. *Geophysics*, **55**, 748–754.

Kosloff, D. & Tal-Ezer, H., 1993. A modified chebyshev pseudospectral method with an $O(N^{-1})$ time step restriction. *J. Comput. Phys.*, **104**, 457–469.

Kostelec, P., Maslen, D., Healy, D. & Rockmore, D., 2000. Computational harmonic analysis for tensor fields on the two-sphere. *J. Comp. Phys.*, **162**, 514–535.

Lay, T., 1995. Seismology of the lower mantle and core-mantle boundary. *Rev. Geophys.*, 325–328. Supplement.

Lay, T., Garnero, E., Young, C. & Gaherty, J., 1997. Scale-lengths of shear velocity heterogeneity at the base of the mantle from S wave differential times. *J. Geophys. Res.*, **102**, 9887–9910.

Lay, T., Williams, Q. & Garnero, E., 1998. The core-mantle boundary layer and deep Earth dynamics. *Nature*, **392**, 461–468.

Levander, A., 1988. Fourth-order finite difference P-SV seismograms. *Geophysics*, **53**, 1425–1436.

Li, X. B. & Romanowicz, B., 1996. Global mantle shear velocity model developed using nonlinear asymptotic coupling theory. *J. Geophys. Res.*, **101**, 11,245–22,271.

Li, X. D. & Tanimoto, T., 1993. Waveforms of long–period body waves in slightly aspherical Earth model. *Geophys. J. Int.*, **112**, 92–102.

Liu, X. & Dziewonski, A., 1998. Global analysis of shear wave velocity anomalies in the lowermost mantle. In M. G. et al. (Ed.), *The Core-Mantle boundary region*, Volume 28 of *Geodyn. Ser.*, pp. 21–36. Washington D.C.: AGU.

Lognonné, P., 1991. Normal modes and seismograms in an anelastic rotating earth. *J. Geophys. Res.*, **96**, 20,309–20,319.

Lognonné, P. & Clévédé, E., 1997. Diffraction of long-period rayleigh waves by a slab: effects of mode coupling. *Geophys. Res. Lett.*, **24**, 1035–1038.

Lognonné, P. & Clévédé, E., 2000. Normal Modes of the Earth and Planets. In P. Jennings, H. Kanamori, & W. Lee (Eds.), *Handbook of Earthquake and Engineering Seismology*. Paolo Alto, CA: IASPEI. in press.

Lognonné, P. & Romanowicz, B., 1990. Modelling of coupled normal modes of the Earth: the spectral method. *Geophys. J. Int.*, **102**, 365–395.

Maday, Y. & Patera, A., 1989. Spectral element methods for the incompressible Navier-Stokes equations. In A. Noor & J. Oden (Eds.), *State of the Art Survey in Computational Mechanics*, pp. 71–143. New-York: ASME.

Masters, G., Johnson, S., Laske, G. & Bolton, H., 1996. A shear-velocity model of the mantle. *Philos. Trans. R. Soc. London, Ser. A*, **354**, 1385–1411.

Matzel, E., Sen, M. & Grand, S., 1996. Evidence for anisotropy in the deep mantle beneath Alaska. *Geophys. Res. Lett.*, **23**, 2417–2420.

Merilees, P., 1973. The pseudospectral approximation applied to shallow water equations on a sphere. *Atmosphere*, **11**, 13–20.

Newman, E. & Penrose, R., 1966. Note on the Bondi-Metzner-Sachs group. *J. Math. Phys.*, **7**, 836.

Patera, A. T., 1984. A spectral element method for fluid dynamics: laminar flow in a channel expansion. *J. Comput. Phys.*, **54**, 468–488.

Phinney, R. A. & Burridge, R., 1973. Representation of elastic-gravitational excitation of a spherical earth model by generalized spherical harmonics. *Geophys. J. R. Astron. Soc.*, **34**, 451–278.

Pollitz, F., 1998. Scattering of spherical elastic waves from small-volume spherical inclusion. *Geophys. J. Int.*, **134**, 390–408.

Priolo, E., Carcione, J. M. & Seriani, G., 1994. Numerical simulation of interface waves by high-order spectral modeling techniques. *J. Acoust. Soc. Am.*, **95:2**, 681–693.

Pulliam, J. & Sen, M., 1999. Seismic anisotropy in the core-mantle transition. *Geophys. J. Int.*.

Rančić, M., Purser, R. & Mesinger, F., 1996. A global shallow-water model using expanded spherical cube: Gnomonic versus conformal coordinates. *Quart. J. Roy. Met. Soc.*, **122**, 959.

Resovsky, J. & Ritzwoller, M., 1999. A degree 8 mantle shear velocity model from normal mode observations below 3 mHz. *J. Geophys. Res.*, **104**, 993–1014.

Ritzwoller, M. & Lavely, E., 1995. Three dimensional seismic models of the Earth's mantle. *Rev. Geophys.*, **33**, 1–66.

Romanowicz, B., 1987. Multiplet–multiplet coupling due to lateral heterogeneity: asymptotic effects on the amplitude and frequency of the Earth's normal modes. *Geophys. J. R. Astron. Soc.*, **90**, 75–100.

Romanowicz, B. & Roult, G., 1986. First order asymptotics for the eigenfrequencies of the Earth and application to the retrieval of large-scale variations of structure. *Geophys. J. R. Astr. Soc.*, **87**, 209–240.

Ronchi, C., Ianoco, R. & Paolucci, P. S., 1996. The 'Cubed Sphere': a new method for the solution of partial differential equations in spherical geometry. *J. Comput. Phys.*, **124**, 93–114.

Sadourny, R., 1972. Conservative finite-difference approximations of the primitive equation on quasi-uniform spherical grids. *Mon. Weather Rev.*, **100**, 136–144.

Saito, M., 1988. DISPER80: A subroutine package for the calculation of seismic normal–mode solutions. In D. J. Doornbos (Ed.), *Seismological alogorithms*, pp. 294–319. Academic Press, New York.

Snieder, R. & Romanowicz, B., 1988. A new formalis for the effect of lateral heterogeneity on normal modes and surface waves: I. Isotropic perturbations, perturbations of interfaces and gravitational perturbances. *Geophys. J. Int.*, **92**, 207–222.

Su, W., Woodward, R. & Dziewonski, A., 1994. Degree 12 model of shear velocity heterogeneity in the mantle. *J. Geophys. Res.*, **99**, 6945–6980.

Takeuchi, H. & Saito, M., 1972. Seismic surface waves. *Methods in computational Physics.*, **11**, 217–295.

Takeuchi, N., Geller, R. & Cummins, P. R., 2000. Complete synthetic seismograms for 3–D heterogeneous Earth models computed usind modified DSM operators and their applicability to inversion for Earth structure. *Phys. Earth Planet. Inter.*, **119**, 25–36.

Tromp, J. & Dahlen, F., 1992. Variational principles for surface wave propagation on a laterally heterogeneous Earth: 2. Frequency domain JWKB theory. *Geophys. J. Int.*, **109**, 599–619.

Valette, B., 1987. *Spectre des oscillations libres de la Terre : aspects mathématiques et géophysiques*. Thèse de Doctorat d'état, Université Paris VII.

Valette, B., 1989. Spectre de vibrations propres d'un corps élastique, autogravitant, en rotation uniforme et contenant une partie fluide. *C.R. Acad. Sci.*, **309**, 419–422. Série I.

van der Hilst, R., Widiyantoro, S., Creager, K. & McSweeney, T., 1998. Deep subsuction and aspherical variations in P-wavespeed at the base of the Earth's mantle. In G. et al. (Ed.), *Core-Mantle boundary region*, Volume 28 of *Geodyn. Ser.*, pp. 5–20. Washington D.C.: AGU.

van der Hilst, R., Widiyantoro, S. & Engdahl, E., 1997. Evidence for deep mantle circulation grom global tomography. *Nature*, **386**, 578–584.

Vasco, D. & Johnson, L., 1998. Whole earth structure estimated from seismic arrival times. *J. Geophys. Res.*, **103**, 2633–2671.

Vinnik, L., Romanowicz, B., Stunff, Y. L. & Makeyeva, L., 1996. Seismic anisotropy in the D" layer. *Geophys. Res. Lett.*, **22**, 1657–1660.

Virieux, J., 1986. P-SV wave propagation in heterogeneous media: velocity-stress finite difference method. *Geophysics*, **51**, 889–901.

Woodhouse, J., 261-283. The coupling and attenuation of nearly resonant multiplets in the Earth's free oscillation spectrum. *Geophys. J. R. Astr. Soc.*, **1980**, 61.

Woodhouse, J. H., 1988. The calculation of eigenfrequencies and eigenfunctions of the free oscillations of the earth and the sun. In D. J. Doornbos (Ed.), *Seismological algorithms*, pp. 321–370. Academic Press, New York.

Wu, T. & Yang, C., 1977. Some properties of monopole harmonics. *Phys. Review*, **16**, 1018.

Yarvin, N. & Rokhlin, V., 1998. A generalize one-dimensional fast multipole method with applications to filtering of spherical harmonics. *J. Comp. Phys.*, **147**, 594–609.

Zienkiewicz, O. & Morgan, K., 1983. *Finite elements approximation*. New-York: John Wiley and Sons.

9   FIGURE LEGENDS

Figure 1. The Earth model Ω, with boundary $\partial\Omega$ and internal radius r_{Ω}. The solid and fluid parts are Ω_S and Ω_F respectively. Σ_{SS} and Σ_{SF} denote respectively the set of all the solid-solid and solid-fluid interfaces. The spectral element domain is Ω^+ while the domain of modal summation is Ω^- with Γ denoting the artificial interface between Ω^+ and Ω^-.

Figure 2. The one dimensional domain Ω : the modal solution method is used in Ω^- and the spectral element method in Ω^+. The Discretization of the domain Ω^+ in six regions is also represented. The dotted lines denotes the $\mathcal{F}_{e=4}$ transformation of the reference segment into Ω_4. The Gauss–Lobatto–Legendre (GLL) integration points are shown with the black squares in the reference element $\Lambda = [-1, 1]$ for a polynomial degree $N = 8$.

Figure 3. 1-D smooth heterogeneous model with $L_0 = 3000\,\mathrm{m}$.

Figure 4. a): $\mathcal{A}(t) * g(t)$ computed for the the one dimensional example of Fig. 3. The source time wavelet, g, is a Gaussian of width $30s$, centered in $t = 1500\,\mathrm{s}$

b): $(\mathcal{A}(t) - \mathcal{C}(t)) * g(t)$ after applying the first order regularization term. The Gaussian derivative shape has disappeared, and only a Gaussian shape remains.

c): $(\mathcal{A}(t) - \mathcal{C}(t)) * g(t)$ after applying the second order regularization term. Now only a filtered Heaviside shape remains.

d): $(\mathcal{A}(t) - \mathcal{C}(t)) * g(t)$ after applying the third order regularization term. A causal signal is now retrieved.

Figure 5. Displacement computed for the smooth heterogeneous example of Fig. 3 and recorded at $x = L_0$ (a), $x = 3960\,\mathrm{m}$ (b) and $x = L$ (c). The time source function is a Ricker (second derivative of a Gaussian) of 30 s width and centered at $t_0 = 400\,\mathrm{s}$. The modal solution for the wole domain is shown in solid line. The difference with the coupled solution, amplified by a factor 100, is shown in dotted line. The amplitude is normalized with reference to the maximum displacement recorded at $x = L$.

Figure 6. Displacement recorded at $x = 3960\,\mathrm{m}$ for the heterogeneous example of Fig. 3 with the same source time function than Fig. 5. The solution obtained when using only the spectral element method is shown in solid line. The Dotted lines represent the difference, amplified by a factor 100, with the solution obtained using the coupled method with a first order regularization (error 1), a second order regularization (error 2), and a third order regularization (error 3).

Figure 7. Right: the same experiment as in Fig. 6 but for a rougher heterogeneity distribution shown on the left. The displacement is recorded at $x = 3960$ m.

Figure 8. The Gnomic projection: great circles used to mesh one region of the "cubic sphere".

Figure 9. Left: a splitted view of the six regions produced by the gnomic projection which map the six faces of a cube inscribed inside the sphere to the surface of the sphere. Right: a gathered view of the six regions of the sphere. Each region has its own coordinates system and the coordinate transformations can be calculated analytically.

Figure 10. The sphéroidal (left) and the toroidal (right) eigenfrequencies of the *DtN* operator computed for a homogeneous sphere.

Figure 11. The spectral element mesh used for the homogeneous sphere model. The regions 1 and 4 have been removed for visibility.

Figure 12. The source time function used for the homogeneous sphere model (left) and the correspnding source spectrum content (right). The central frequency is $3.2 \times 10^{-3} \ Hz$ (321 s) and the corner frequency is $8 \times 10^{-3} \ Hz$ (125 s).

Figure 13. The wave field propagation in a crossection of the homogeneous sphere model for an explosive source. The snapshots represent the x-component of the displacement field inside Ω^+, the spherical shell domain of the spectral element method, at different time steps of the propagation. The displacements in Ω^-, the inner sphere of the modal summation method, are not shown here. The accuracy of the coupling method can be assessed here looking at the transmitted wavefield.

Figure 14. The vertical component of seismograms, recorded at the surface, as a function of the epicentral distance from the source B. Different phases are pointed out here: Rayleigh (R), X phase (X) and P wave (P).

Figure 15. The vertical component of the displacement, at an epicentral distance of $90°$, recorded on the surface (left) and on the coupling interface Γ (right). The reference normal mode solution is drawn with the solid line, the coupled method solution is displayed with the dotted line and the residual between the two methods, amplified by a factor 10, is displayed with the bold dotted line. The method is very accurate and the maximum relative error is less than a few percents.

Figure 16. The transverse component of the displacement, at an epicentral distance of $49°$, recorded on the surface (left) and on the coupling interface Γ (right). The source is at 1048 km depth, with a moment tensor with $M_{rr}=M_{\theta\theta}=M_{\phi\phi}=M_{r\theta}=0$ and $M_{r\phi}=M_{\theta\phi}=1$. The reference normal mode solution is drawn with the solid line, the coupled method solution is displayed with the dotted line and the residual between the two methods, amplified by a factor 10, is displayed with the bold dotted line.

Figure 17. The non conforming mesh used for the PREM example: below the 660 km interface, the mesh has been derefined by a factor two in the horizontal direction. The color indicates the density structure of the model. The regions 1 and 4 have been removed here for visibility.

Figure 18. The source time function used for the PREM example (left) and the corresponding spectrum content (right). The corner frequency is $1/48$ Hz.

Figure 19. The vertical component of the seismograms computed in PREM and recorded at the surface, as a function of the epicentral distance. Time arrivals of some body waves computed by a ray tracing has been superposed and can be identified using Fig. 20.

Figure 20. Time arrivals of some body waves in PREM computed with a ray tracing.

Figure 21. Displacement recorded at the free surface in the PREM example. The vertical (right) and longitudinal (left) displacements are plotted for three epicentral distances. The modal solution (reference) is plotted with a solid line while the coupled method solution is displayed with a dotted line (superposed to the previous one). In a bold dotted line, the residual, multiplied by 10, between the two solutions is also shown on the same figures.

Figure 22. Displacement recorded at the CMB which is here the coupling interface Γ for the PREM example. The vertical (right) and longitudinal (left) displacements are plotted for three epicentral distances. The modal solution (reference) is plotted with a solid line while the coupled method solution is displayed with a dotted line (superposed to the previous one). In a bold dotted line, the residual, multiplied by 10, between the two solutions is also shown on the same figures.

APPENDIX A: RESIDUAL COMPUTATION

The analytical computation of the Cauchy residuals $\mathcal{A}'_n$ in equation (42) requires the evaluation of the derivative of $\mathcal{D}$ at ω_n. Using the continuity of $\mathcal{T}$ at the frequency ω_n,

$$\lim_{\omega \to \omega_n} (\omega - \omega_n)\hat{\mathcal{A}}(\omega) = \mathcal{T}(\omega_n) \left. \frac{\mathrm{d}\mathcal{D}}{\mathrm{d}\omega} \right|_{\omega_n}^{-1} . \tag{A1}$$

An expression of this derivative can be directly obtained from the weak form of the equation (35). The solution $U(x, \omega)$ of (35) satisfies $\forall w \in \mathcal{C}$

$$\left[\lambda(x)w(x)\frac{\partial U}{\partial x} \right]_{L_0} = -\omega^2 \int_0^{L_0} \rho(x)U(x)w(x)\,\mathrm{d}x + \int_0^{L_0} \lambda(x)\frac{\partial U}{\partial x}\frac{\partial w}{\partial x}\,\mathrm{d}x . \tag{A2}$$

With $w = U$ and noting I_1 the kinetic energy and I_2 the elastic strain energy,

$$I_1(\omega) = \int_0^{L_0} \rho U^2(x, \omega)\,\mathrm{d}x ,$$

$$I_2(\omega) = \int_0^{L_0} \lambda(x) \left(\frac{\partial U}{\partial x}(x, \omega) \right)^2 \mathrm{d}x ,$$

(A2) becomes

$$\left[\lambda(x)U(x, \omega)\frac{\partial U}{\partial x}(x, \omega) \right]_{L_0} = -\omega^2 I_1(\omega) + I_2(\omega) . \tag{A3}$$

For $\omega = \omega_n$, $U(x, \omega_n) = 0$ and therefore

$$-\omega_n^2 I_1(\omega_n) + I_2(\omega_n) = 0 . \tag{A4}$$

Furthermore, (A3) follows the Rayleigh's stationary principle, e.g. Takeuchi & Saito (1972) or Dahlen & Tromp (1998), and for all perturbations $\partial U(x, \omega_n)$ of $U(x, \omega_n)$:

$$-\omega_n^2 \partial I_1(\omega_n) + \partial I_2(\omega_n) = 0 \,. \tag{A5}$$

Computing the derivative of (A3) along ω, we obtain

$$\left[\lambda(x) \left(\frac{\partial U}{\partial \omega}\frac{\partial U}{\partial x} + U\frac{\partial^2 U}{\partial x \partial \omega} \right) \right]_{L_0} = -2\omega I_1 - \omega^2 \frac{\partial I_1}{\partial \omega} + \frac{\partial I_2}{\partial \omega} \,. \tag{A6}$$

Setting $\omega = \omega_n$ in the last equation, we finally obtain for $x = L_0$,

$$\left.\frac{\mathrm{d}\mathcal{D}}{\mathrm{d}\omega}\right|_{\omega_n} = -\frac{2\omega_n I_1(\omega_n)}{\mathcal{T}(\omega_n)} \,, \tag{A7}$$

and therefore

$$\mathcal{A}'_n = -\frac{\mathcal{T}^2(\omega_n)}{2\omega_n I_1(\omega_n)} \,. \tag{A8}$$

APPENDIX B: *DtN* OPERATOR USING RADIAL FUNCTIONS U,V AND W

For practical reason, it is of interest to express the operator *DtN* in terms of the radial functions (U, V, W), as defined in the equation (84), with the corresponding stress vectors (T_U, T_V, T_W), as classically used in surface wave seismology and normal modes theory (e.g. Gilbert 1971). The three independent solutions of (82) in $\mathbf{\Omega}^-$, regular in $r = 0$, are denoted according to (84) as $\left(U_\ell^{(1)}, V_\ell^{(1)}, 0 \right)$, $\left(U_\ell^{(2)}, V_\ell^{(2)}, 0 \right)$ and $(0, 0, W_\ell)$. Using (85) we obtain

$$\mathbf{\mathcal{D}}_\ell = \zeta_\ell \begin{pmatrix} \kappa_\ell V_\ell^{(1)} & U_\ell^{(1)} & \kappa_\ell V_\ell^{(1)} \\ \kappa_\ell V_\ell^{(2)} & U_\ell^{(2)} & \kappa_\ell V_\ell^{(2)} \\ -i\kappa_\ell W_\ell & 0 & i\kappa_\ell W_\ell \end{pmatrix} \,, \tag{B1}$$

and for the stress vectors

$$\mathbf{\mathcal{T}}_\ell = \zeta_\ell \begin{pmatrix} \kappa_\ell T_{V,\ell}^{(1)} & T_{U,\ell}^{(1)} & \kappa_\ell T_{V,\ell}^{(1)} \\ \kappa_\ell T_{V,\ell}^{(2)} & T_{U,\ell}^{(2)} & \kappa_\ell T_{V,\ell}^{(2)} \\ -i\kappa_\ell T_{W,\ell} & 0 & i\kappa_\ell T_{W,\ell} \end{pmatrix} \,, \tag{B2}$$

Where $\kappa_\ell = \gamma_\ell/\sqrt{2} = \sqrt{(\ell(\ell+1)/2)}$. The inverse of $\tilde{\mathcal{D}}$ is straightforward to compute:

$$\tilde{D}_\ell^{-1} = \frac{1}{2\Delta_\ell \kappa_\ell \zeta_\ell} \begin{pmatrix} U_\ell^{(2)} & -U_\ell^{(1)} & \dfrac{i\Delta_\ell}{W_\ell} \\ [4pt] -2V_\ell^{(2)}\kappa_\ell & 2V_\ell^{(1)}\kappa_\ell & 0 \\ U_\ell^{(2)} & -U_\ell^{(1)} & \dfrac{-i\Delta_\ell}{W_\ell} \end{pmatrix} \tag{B3}$$

where $\Delta_\ell = V_\ell^{(1)} U_\ell^{(2)} - V_\ell^{(2)} U_\ell^{(1)}$. This last equation is undefined for $\omega \in \Pi_\ell^d$, the set of all the eigen-frequencies of $\mathbf{\Omega}^-$ corresponding to a rigid displacement condition: $\Delta_\ell(r_{\mathbf{\Gamma}}, \omega) = 0$ or $W_\ell(r_{\mathbf{\Gamma}}, \omega) = 0$. As in the normal mode case, there are two types of eigenfrequencies: the spheroidal ones corresponding to the zeros of $\Delta_\ell(r_{\mathbf{\Gamma}}, \omega)$; the toroidal ones corresponding to the zeros of $W_\ell(r_{\mathbf{\Gamma}}, \omega)$. Performing the product of (B3) with (B2), the following expression for $\mathcal{A}$ is obtained:

$$
\mathcal{A}_\ell = \frac{1}{2\Delta_\ell}
$$

$$
\times
\begin{pmatrix}
T_{V\ell}^{(1)} U_\ell^{(2)} - T_{V\ell}^{(2)} U_\ell^{(1)} & (T_{U\ell}^{(1)} U_\ell^{(2)} - T_{u2} U_\ell^{(1)})/\kappa_\ell & T_{V\ell}^{(1)} U_\ell^{(2)} - T_{V\ell}^{(2)} U_\ell^{(1)} \\[2mm]
2\kappa_\ell (T_{V\ell}^{(2)} V_\ell^{(1)} - T_{V\ell}^{(1)} V_\ell^{(2)}) & 2(T_{U\ell}^{(2)} V_\ell^{(1)} - T_{U\ell}^{(1)} V_\ell^{(2)}) & 2\kappa_\ell (T_{V\ell}^{(2)} V_\ell^{(1)} - T_{V\ell}^{(1)} V_\ell^{(2)}) \\[2mm]
T_{V\ell}^{(1)} U_\ell^{(2)} - T_{V\ell}^{(2)} U_\ell^{(1)} & (T_{U\ell}^{(1)} U_\ell^{(2)} - T_{U\ell}^{(2)} U_\ell^{(1)})/\kappa_\ell & T_{V\ell}^{(1)} U_\ell^{(2)} - T_{V\ell}^{(2)} U_\ell^{(1)}
\end{pmatrix}
$$

$$
+ \frac{T_{W\ell}}{2W_\ell}
\begin{pmatrix}
1 & 0 & -1 \\
0 & 0 & 0 \\
-1 & 0 & 1
\end{pmatrix} .
$$

(B4)

where the radius r is set to $r_{\mathbf{\Gamma}}$.

In the case of a spherical symmetry, the radial eigenfunctions and the eigenfrequencies can be computed with the help of the minors corresponding to the solutions basis (Takeuchi & Saito, 1972; Saito, 1988; Woodhouse, 1988). In terms of these minors, the *DtN* operator has the following expression :

$$
\mathcal{A}(\omega) = \frac{1}{2m_2(r_{\mathbf{\Gamma}}, \omega)}
\begin{pmatrix}
m_3(r_{\mathbf{\Gamma}}, \omega) & m_1(r_{\mathbf{\Gamma}}, \omega)/\sqrt{2} & m_3(r_{\mathbf{\Gamma}}, \omega) \\[2mm]
-m_6(r_{\mathbf{\Gamma}}, \omega)/\sqrt{2} & 2m_4(r_{\mathbf{\Gamma}}, \omega) & -m_6(r_{\mathbf{\Gamma}}, \omega)/\sqrt{2} \\[2mm]
m_3(r_{\mathbf{\Gamma}}, \omega) & m_1(r_{\mathbf{\Gamma}}, \omega)/\sqrt{2} & m_3(r_{\mathbf{\Gamma}}, \omega)
\end{pmatrix}
$$

$$
+ \frac{y_6(r_{\mathbf{\Gamma}}, \omega)}{2y_5(r_{\mathbf{\Gamma}}, \omega)}
\begin{pmatrix}
1 & 0 & -1 \\
0 & 0 & 0 \\
-1 & 0 & 1
\end{pmatrix} .
$$

(B5)

where $m_1, \ldots, m_6$ denotes the minors corresponding to the spheroidal solutions and y_5, y_6 the radial eigenfunctions and the stress vector corresponding to the toroidal solution, as defined by (Saito, 1988). The ℓ dependence have been omitted for sake of simplicity. The symmetry of $\mathcal{A}$ results directly from the fact that $m_1 = -m_6$.

APPENDIX C: ASYMPTOTIC EXPANSION OF THE *DtN* OPERATOR IN THE 3D CASE

Following Takeuchi & Saito (1972), we seek a solution of (80) in the form of (82) for the displacement and of (83) for the stress vector. This leads to solve : for the solid-solid case, two 1D coupled first-order differential equations in r for the spheroidal solutions and one for the toroidal solution ; for the solid–fluid case, a 1D coupled first-order differential equation in r. In both cases, the procedure follows the same steps than in the 1D example of section 3.5.

For sake of simplicity, only a linearly isotropic medium will be considered here. Extension to transversely isotropic medium is quite straightforward and does not lead to any specific problem. The P-wave and S-wave velocities are denoted here respectively $\alpha = \sqrt{(\lambda + 2\mu)/\rho}$ and $\beta = \sqrt{\mu/\rho}$, where λ and μ are the elastic Lame parameters.

C1   Solid–fluid coupling

This involves only a scalar differential equation and therefore this case is very close to the 1D example. The only difference is that the expansion in $(i\omega)^{-k}$ of $\mathbf{S}(x,\omega)$ matrix has now more terms. Following Saito (1988),

$$\mathbf{S}(r,\omega) = \begin{pmatrix} -\dfrac{1}{r} & \dfrac{1}{\rho\alpha^2} - \dfrac{\ell(\ell+1)}{\omega^2\rho r^2} \\[2ex] -\omega^2\rho & \dfrac{1}{r} \end{pmatrix}. \tag{C1}$$

$\mathbf{S}(r,\omega)$ is expanded in $(i\omega)^{-1}$ as

$$\mathbf{S}(r,\omega) = \begin{pmatrix} 0 & \frac{1}{i\omega\rho\alpha^2} \\ i\rho\omega & 0 \end{pmatrix} i\omega + \begin{pmatrix} -\frac{1}{r} & 0 \\ 0 & \frac{1}{r} \end{pmatrix} + \begin{pmatrix} 0 & \frac{a_\ell}{i\omega} \\ 0 & 0 \end{pmatrix} \frac{1}{i\omega}. \tag{C2}$$

where $a_\ell = \ell(\ell+1)/\rho r^2$ and $\mathbf{S}_{-1}$, $\mathbf{S}_0$ and $\mathbf{S}_1$ are here equal to zero.

Equation (62) gives

$$\Phi'^2 - \frac{1}{\alpha^2} = 0. \tag{C3}$$

This last equation has two solutions. Keeping only the outgoing waves, we obtain $\Phi' = -1/\alpha$. Furthermore, (62) gives

$$T_0(r) = c_0 u_0(r), \tag{C4}$$

with $c_0 = \rho\alpha$.

After some algebra, (63) leads for $k = 1$

$$T_1(r) = \alpha\left(-\frac{c_0'}{2} + \frac{c_0}{r}\right) u_0(r) + c_0 u_1(r), \tag{C5}$$

and $u_0'(r) = -\frac{c_0'}{2c_0} u_0(r)$. We note $c_1(r) = \alpha \left(-\frac{c_0'}{2} + \frac{c_0}{r} \right)$.

and for $k = 2$,

$$T_2(r) = c_{2,\ell}(r) u_0(r) + \left(\frac{\rho \alpha}{r} - c_0' \right) u_1(r) + c_0 u_2(r) , \tag{C6}$$

where

$$c_{2,\ell}(r) = \frac{\alpha}{2} \left(-c_0^2 a_\ell - c_1' - \frac{c_1}{2} \frac{c_0'}{c_0} + \frac{c_1}{r} \right) . \tag{C7}$$

Setting $r = r_\Gamma$, we obtain the first three terms of the asymptotic expansion of $\mathcal{C}_\ell^{00}$,

$$\mathcal{C}_\ell^{00} = c_0(r_\Gamma) i\omega + c_1(r_\Gamma) + c_{2,\ell}(r_\Gamma) \frac{1}{i\omega} + \mathcal{O}\left((i\omega)^{-2} \right) . \tag{C8}$$

The remaining components $\mathcal{C}_\ell^{\alpha\alpha'}$ for $\alpha \neq 0$ or $\alpha' \neq 0$ are equal to zero. The first two terms of $\mathcal{C}_\ell^{00}$ do not depend upon ℓ which means that these operators are local in space in contrast to the third term $c_{2,\ell}$.

C2   Solid–solid coupling

This case involves two uncoupled systems of equations, one for the SH waves (toroidal) and one for the P–SV waves (spheroidal).

C2.1   *Toroidal case*

Once again, the equation to solve is a scalar one and the procedure is the same as in the previous case.

$$\mathbf{S}(r, \omega) = \begin{pmatrix} \frac{2}{r} & \frac{1}{\mu} \\ -\rho\omega^2 + \frac{\Omega_\ell \mu}{r} & -\frac{2}{r} \end{pmatrix} , \tag{C9}$$

where $\Omega_\ell = (\ell - 1)(\ell + 2)$ and $\mathbf{S}$ can be expanded as

$$\mathbf{S}(r, \omega) = \begin{pmatrix} 0 & \frac{1}{i\omega\mu} \\ i\omega\rho & 0 \end{pmatrix} i\omega + \begin{pmatrix} \frac{2}{r} & 0 \\ 0 & -\frac{2}{r} \end{pmatrix} + \begin{pmatrix} 0 & 0 \\ \frac{\Omega_\ell \mu}{r} & 0 \end{pmatrix} \frac{1}{i\omega} . \tag{C10}$$

For $k = 0$, one get

$$\Phi' = -\frac{1}{\beta} \quad \text{and} \quad T_0(r) = t_0 u_0(r) \tag{C11}$$

with $t_0 = \rho\beta$.

For $k = 1$,

$$T_1(r) = t_1 u_0(r) + t_0 u_0(1) \quad \text{with} \quad t_1 = -\frac{\beta}{2} \left(t_1' + 4\frac{t_0}{r} \right) \tag{C12}$$

For $k = 2$, one finally get

$$T_2(r) = t_2 u_0(r) - \beta \left(t_0' + 2\frac{t_0}{r} \right) u_1(r) + t_0 u_2(r) \,,\tag{C13}$$

with

$$t_2 = \frac{\beta}{2} \left(\frac{\Omega_\ell \mu}{r} + \frac{t_1}{2}\frac{t_0'}{t_0} - t_1' - 2\frac{t_1}{r} \right) \,.\tag{C14}$$

C2.2   Spheroidal case

In this case, the dimension of the solution space is now 2. Let first introduce here the following parameters :

$$\gamma_\ell = \sqrt{\ell(\ell+1)}\,, \qquad\qquad a = \frac{4}{r^2}\left(\lambda + 2\mu - \frac{\lambda^2}{\lambda + 2\mu} - \mu \right)\,,$$

$$b_\ell = \frac{\gamma_\ell}{r^2}\left(\lambda + 2\mu - \frac{\lambda^2}{\lambda + 2\mu} \right) - \frac{2\mu}{r^2}\,, \qquad d = 1 - \frac{2\mu}{\lambda + 2\mu}\,,$$

$$e_\ell = \gamma_\ell \frac{\mu}{\lambda + 2\mu}\,.$$

We have

$$\mathbf{S}(r,\omega) = \begin{pmatrix} \dfrac{d}{r} & \dfrac{1}{\lambda + 2\mu} & \dfrac{e_\ell}{r} & 0 \\[2mm] -\rho\omega^2 + a & -\dfrac{d}{r} & \dfrac{a\gamma_\ell}{2} & \dfrac{\gamma_\ell}{r} \\[2mm] -\dfrac{\gamma_\ell}{r} & 0 & \dfrac{2}{r} & \dfrac{1}{\mu} \\[2mm] \dfrac{a\gamma_\ell}{2} & -\dfrac{e_\ell}{r} & -\rho\omega^2 + b_\ell & -\dfrac{2}{r} \end{pmatrix}\tag{C15}$$

which can be expanded as

$$\mathbf{S}(r,\omega) = \begin{pmatrix} 0 & (i\omega\rho\alpha^2)^{-1} & 0 & 0 \\ i\omega\rho & 0 & 0 & 0 \\ 0 & 0 & 0 & (i\omega\rho\beta^2)^{-1} \\ 0 & 0 & i\omega\rho & 0 \end{pmatrix} i\omega + \begin{pmatrix} \frac{d}{r} & 0 & \frac{e_\ell}{r} & 0 \\ 0 & -\frac{d}{r} & 0 & \frac{\gamma_\ell}{r} \\ -\frac{\gamma_\ell}{r} & 0 & \frac{2}{r} & 0 \\ 0 & -\frac{e_\ell}{r} & 0 & -\frac{2}{r} \end{pmatrix}$$

$$+ \begin{pmatrix} 0 & 0 & 0 & 0 \\ ai\omega & 0 & \frac{a\gamma_\ell}{2}i\omega & 0 \\ 0 & 0 & 0 & 0 \\ \frac{a\gamma_\ell}{2}i\omega & 0 & b_\ell i\omega & 0 \end{pmatrix} \frac{1}{i\omega}\tag{C16}$$

Looking for a solution of the form

$$\mathbf{y}(r,\omega) = e^{-i\omega\Phi(x)} \sum_{k\geq 0} \mathbf{y}_k(x,\omega)(i\omega)^{-k}\,,\tag{C17}$$

with

$$\mathbf{y}_k(x, \omega) = {}^t\left(u_k(r), i\omega T_{u,k}(r), v_k(r), i\omega T_{v,k}(r)\right) , \tag{C18}$$

where ^{t} denotes the transpose operator.

Equation (62) leads to

$$\left(\Phi' - \frac{1}{\alpha^2}\right)\left(\Phi' - \frac{1}{\beta^2}\right) = 0 . \tag{C19}$$

This last equation has four solutions

$$\Phi' = \pm\frac{1}{\alpha} ,$$
$$\Phi' = \pm\frac{1}{\beta} .$$

Keeping only the outgoing waves, we get two solutions. The first solution is $\Phi' = -\alpha^{-1}$ for $r = r_{\Gamma}$ and

$$
\begin{aligned}
u^{(1)} \quad &= 1 \\
T_u^{(1)} \quad &= a_{10}i\omega \quad + a_{11} \quad\quad\quad + a_{12}(i\omega)^{-1} \\
v^{(1)} \quad &= c_{10} \quad\quad + c_{11}(i\omega)^{-1} \quad + c_{12}(i\omega)^{-2} \\
T_v^{(1)} \quad &= b_{10}i\omega \quad + b_{11} \quad\quad\quad + b_{12}(i\omega)^{-1}
\end{aligned} \tag{C20}
$$

The second solution is $\Phi' = -\beta^{-1}$ for $r = r_{\Gamma}$ and

$$
\begin{aligned}
u^{(2)} \quad &= c_{20} \quad\quad + c_{21}(i\omega)^{-1} \quad + c_{22}(i\omega)^{-2} \\
T_u^{(2)} \quad &= b_{20}i\omega \quad + b_{21} \quad\quad\quad + b_{22}(i\omega)^{-1} \\
v^{(2)} \quad &= 1 \\
T_v^{(2)} \quad &= a_{20}i\omega \quad + a_{21} \quad\quad\quad + a_{22}(i\omega)^{-1}
\end{aligned} \tag{C21}
$$

For the first solution, $\Phi' = -\alpha^{-1}$, equation (62) gives

$$T_{u,0}^{(1)}(r) = a_{10}(r)u_0^{(1)}(r) ,$$

with $a_{10} = \rho\alpha$, and also $v^{(1)}(r) = T_{v,0}^{(1)}(r)$. This implies that $c_{10} = b_{10} = 0$.

Now equation (63), for $k = 1$, leads to

$$T_{u,1}^{(1)}(r) = a_{11}(r)u_0^{(1)}(r) + a_{10}u_1^{(1)}(r) ,$$

$$v_1^{(1)} = c_{11}(r)u_0^{(1)}(r) ,$$

$$T_{v,1}^{(1)}(r) = b_{11}(r)u_0^{(1)}(r) ,$$

with

$$a_{11} = -\frac{\alpha}{2}\left(a'_{10} + 2\frac{a_{10}d}{r}\right),$$

$$b_{11} = \frac{\rho\alpha^2\beta^2}{r(\alpha^2 - \beta^2)}(e_\ell + \gamma_\ell),$$

$$c_{11} = \frac{b_{11}}{a_{10}} + \frac{\alpha e_\ell}{r}.$$

and for $k = 2$, equation (63) gives

$$T_{u,2}^{(1)}(r) = a_{12}(r)u_0^{(1)}(r) + \dots,$$

$$v_2^{(1)} = c_{12}(r)u_0^{(1)}(r) + \dots,$$

$$T_{v,2}^{(1)}(r) = b_{12}(r)u_0^{(1)}(r) + \dots,$$

where "..." stands for the remaining terms which take a zero value for $r = r_\Gamma$, and are therefore only relevant for the third order approximation of the solution of (63). The coefficients a_{12}, b_{12} and c_{12} can be explicitly computed :

$$a_{12} = -\frac{\alpha}{2}\left(a'_{11} - \frac{a'_{10}}{2a_{10}}a_{11} + \frac{a_{11}d}{r} - \frac{\gamma_\ell b_{11}}{r} + a + \frac{a_{10}c_{11}e_\ell}{r}\right),$$

$$b_{12} = \frac{\rho\alpha\beta^2}{r(\alpha^2 - \beta^2)}\left[a_{10}\left(c'_{11} - \frac{a'_{10}}{2a_{10}}c_{11} - \frac{2c_{11}}{r}\right) + b'_{11} - \frac{a'_{10}}{2a_{10}}b_{11} + \frac{a_{11}e_\ell}{r} + \frac{2b_{11}}{r} - \frac{a\gamma_\ell}{2}\right],$$

$$c_{12} = \left[\frac{b_{12}}{a_{10}} + \frac{1}{\rho}\left(b'_{11} - \frac{a'_{10}}{2a_{10}}b_{11} + \frac{a_{11}e_\ell}{r} + \frac{2b_{11}}{r} - \frac{a\gamma_\ell}{2}\right)\right],$$

Setting $r = r_\Gamma$ provides the asymptotic expansion of the first solution on Γ.

For the second solution, following the same steps it can be shown that

$$a_{20} = \rho\beta,$$

$$b_{20} = 0,$$

$$c_{20} = 0,$$

and

$$a_{21} = -\frac{\beta}{2}\left(a'_{20} + 4\frac{a_{20}d}{r}\right),$$

$$b_{21} = \frac{\rho\alpha^2\beta^2}{r(\alpha^2 - \beta^2)}(e_\ell + \gamma_\ell),$$

$$c_{21} = \frac{b_{21}}{a_{20}} - \frac{\beta\gamma_\ell}{r}.$$

with finally

$$a_{22} = -\frac{\beta}{2} \left(a'_{21} - \frac{a'_{20}}{2a_{20}} a_{21} + \frac{2a_{21}}{r} + \frac{e_\ell b_{21}}{r} - b_\ell - \frac{a_{20} c_{21} \gamma_\ell}{r} \right) ,$$

$$b_{22} = \frac{\rho \alpha^2 \beta}{r(\beta^2 - \alpha^2)} \left[a_{20} \left(c'_{21} - \frac{a'_{20}}{2a_{20}} c_{21} + \frac{dc_{21}}{r} \right) + b'_{21} - \frac{a'_{20}}{2a_{20}} b_{21} - \frac{a_{21} \gamma_\ell}{r} + \frac{db_{21}}{r} - \frac{a \gamma_\ell}{2} \right] ,$$

$$c_{22} = \left[\frac{b_{12}}{a_{20}} + \frac{1}{\rho} \left(b'_{21} - \frac{a'_{20}}{2a_{20}} b_{21} - \frac{a_{21} \gamma_\ell}{r} + \frac{db_{21}}{r} - \frac{a \gamma_\ell}{2} \right) \right] ,$$

Having characterized the asymptotic expansion of the two spheroidal solutions, they still have to be combined in order to obtain the asymptotic expansion of $\mathcal{C}$. First, the asymptotic expansion of Δ can be readily computed as

$$\Delta = V^{(1)} U^{(2)} - V^{(2)} U^{(1)} = -1 - c_{11} c_{22} (i\omega)^{-2} + \mathcal{O}\left((i\omega)^{-3} \right) . \tag{C22}$$

and

$$\mathcal{C}^{00} = \frac{T_u^{(2)} V^{(1)} - T_u^{(1)} V^{(2)}}{\Delta} ,$$
$$= a_{10} i\omega + a_{11} + (a_{12} + c_{11} c_{21} a_{10} - c_{11} b_{21}) (i\omega)^{-1} + \mathcal{O}\left((i\omega)^{-2} \right) , \tag{C23}$$

$$\mathcal{C}^{01} = \frac{T_v^{(2)} V^{(1)} - T_v^{(1)} V^{(2)}}{\sqrt{2} \Delta} ,$$
$$= \frac{1}{\sqrt{2}} \left[b_{11} + (b_{12} - c_{11} a_{21} - c_{12} a_{20}) (i\omega)^{-1} \right] + \mathcal{O}\left((i\omega)^{-2} \right) , \tag{C24}$$

$$\mathcal{C}^{10} = \frac{T_v^{(1)} U^{(2)} - T_v^{(2)} U^{(1)}}{\sqrt{2} \Delta} ,$$
$$= \frac{1}{\sqrt{2}} \left[b_{21} + (b_{22} - c_{21} a_{11} + c_{22} a_{10}) (i\omega)^{-1} \right] + \mathcal{O}\left((i\omega)^{-2} \right) , \tag{C25}$$

$$\mathcal{C}^{11} = \frac{T_v^{(1)} U^{(2)} - T_v^{(2)} V^{(1)}}{2\Delta} ,$$
$$= \frac{1}{2} \left[a_{20} i\omega + a_{21} + (a_{22} + c_{11} c_{21} a_{20} - c_{21} b_{11}) (i\omega)^{-1} \right] + \mathcal{O}\left((i\omega)^{-2} \right) . \tag{C26}$$

The full asymptotic expansion of $\mathcal{C}$ is obtained by adding the toroidal solution. One can check that $\mathcal{C}^{01} = \mathcal{C}^{10}$, and that the first two terms of $\mathcal{C}^{00}$ and $\mathcal{C}^{11}$ are local in space (independent of ℓ).
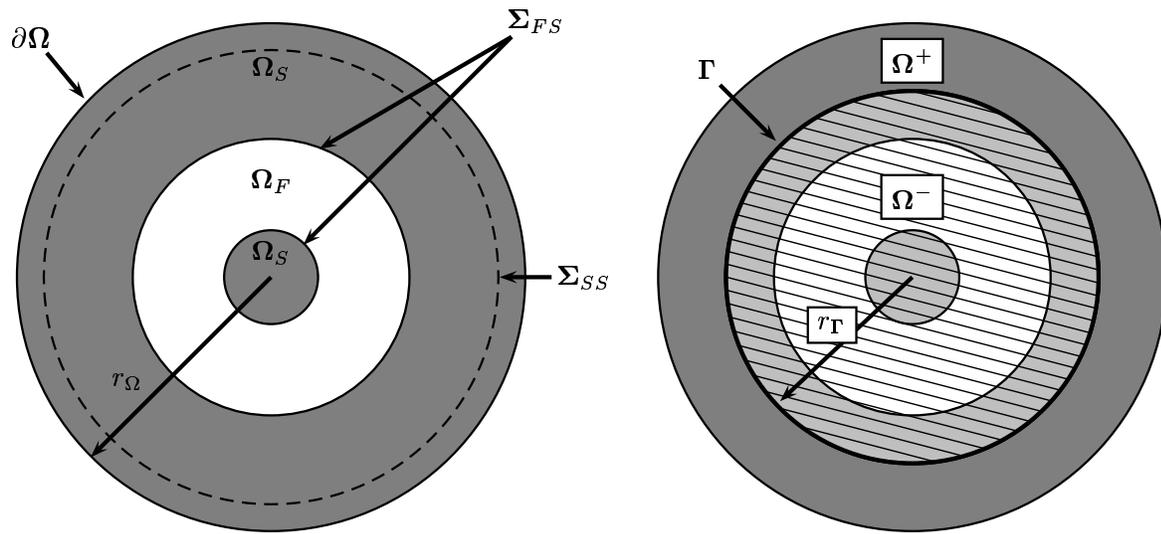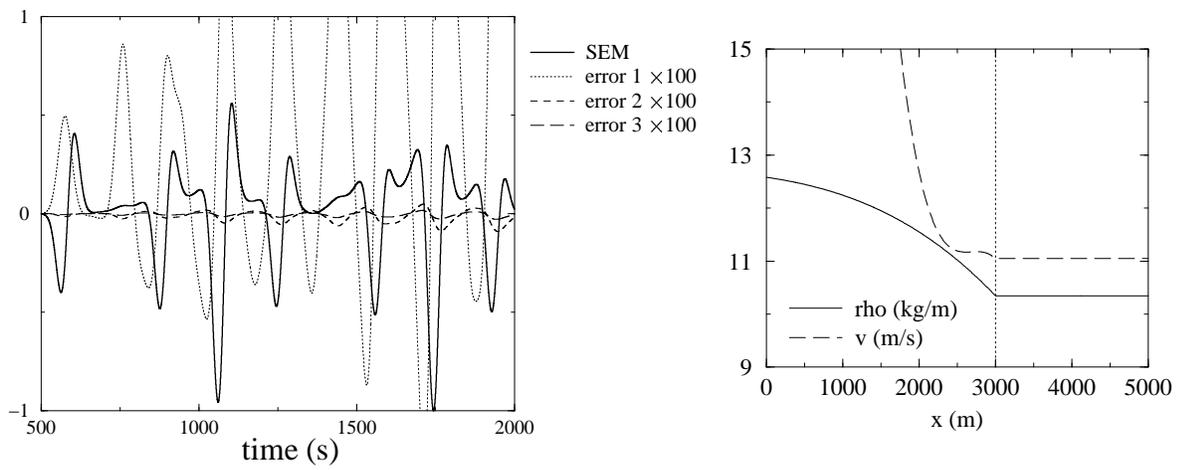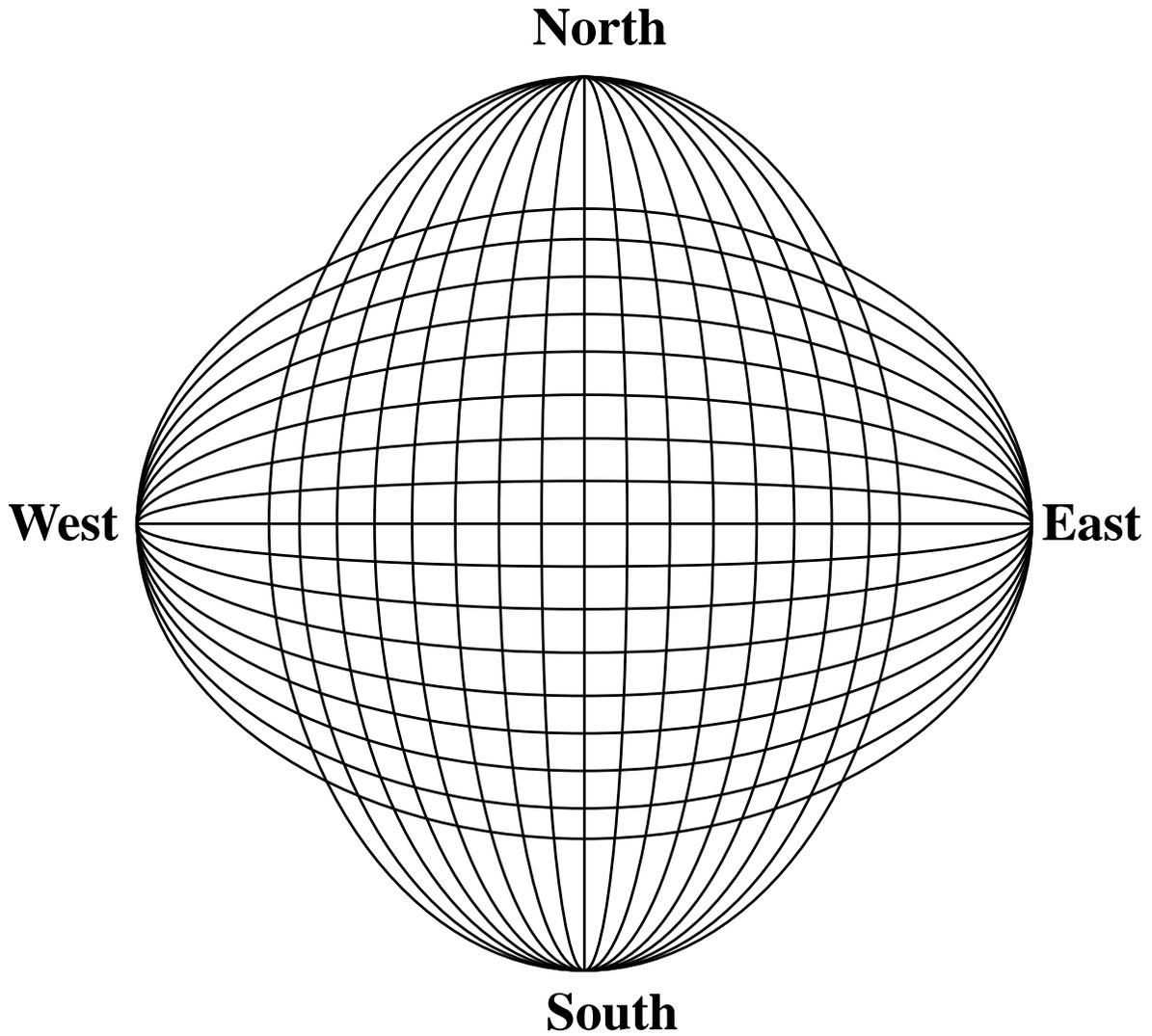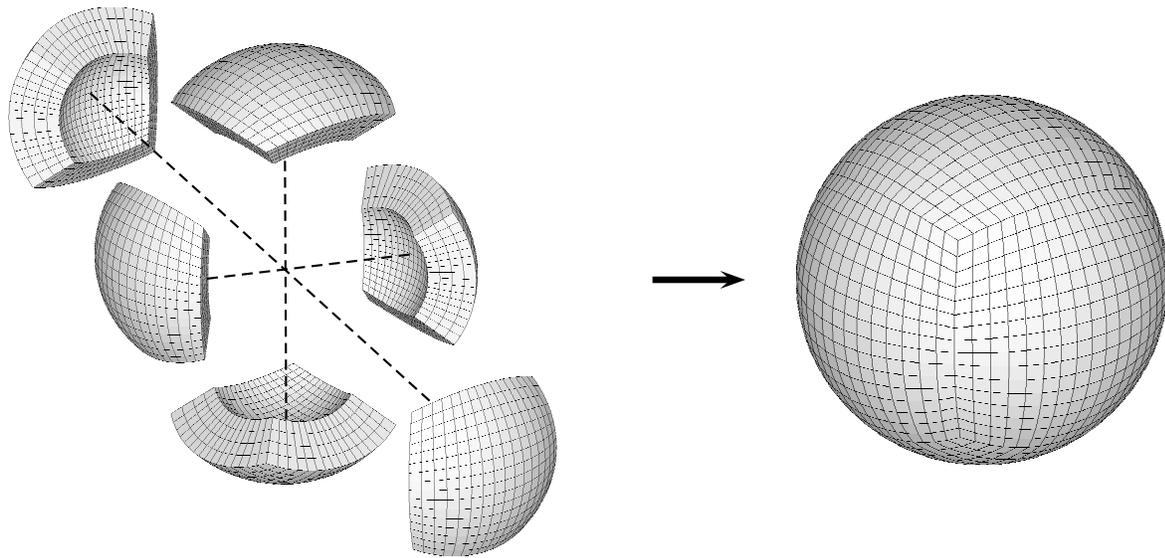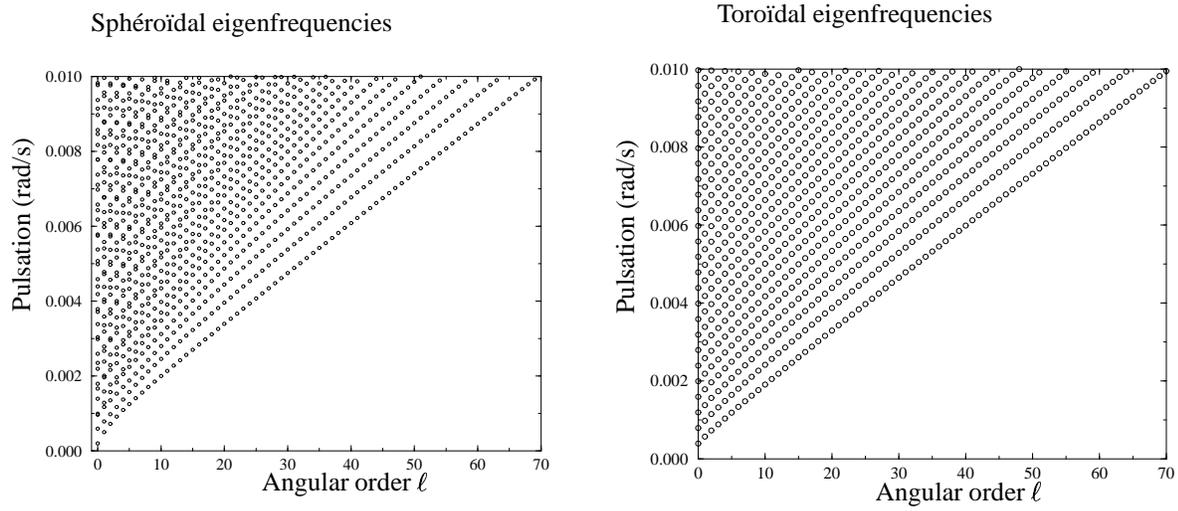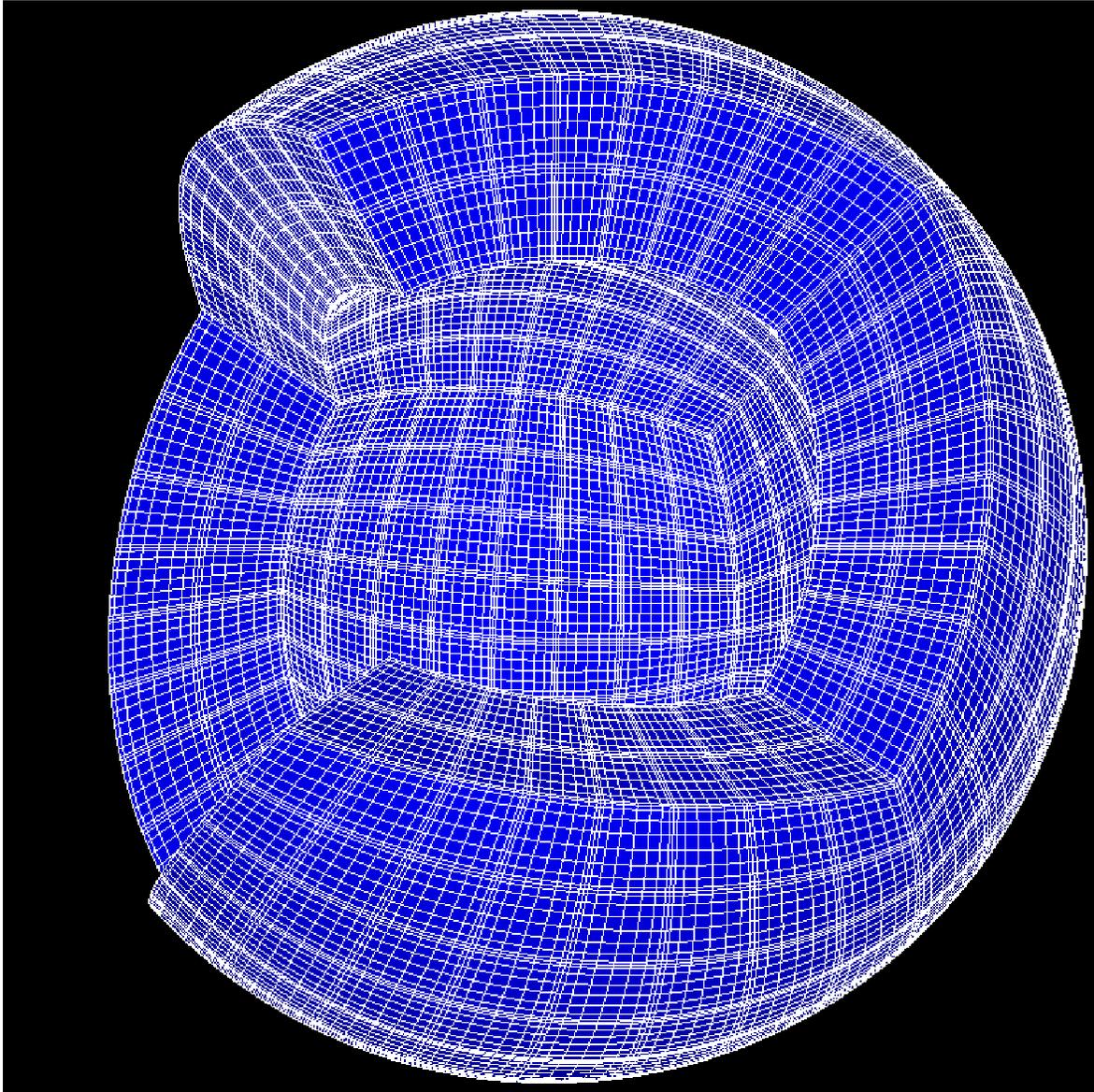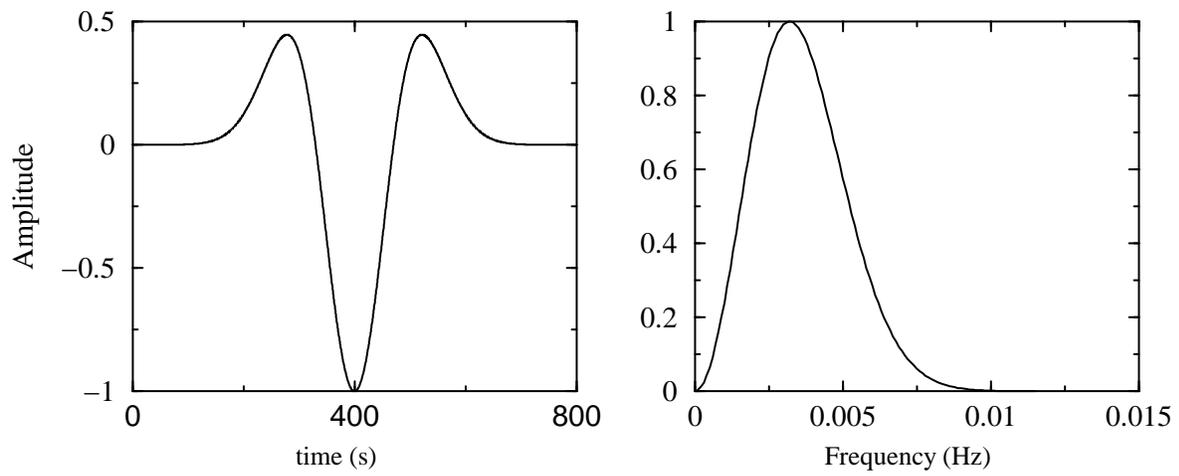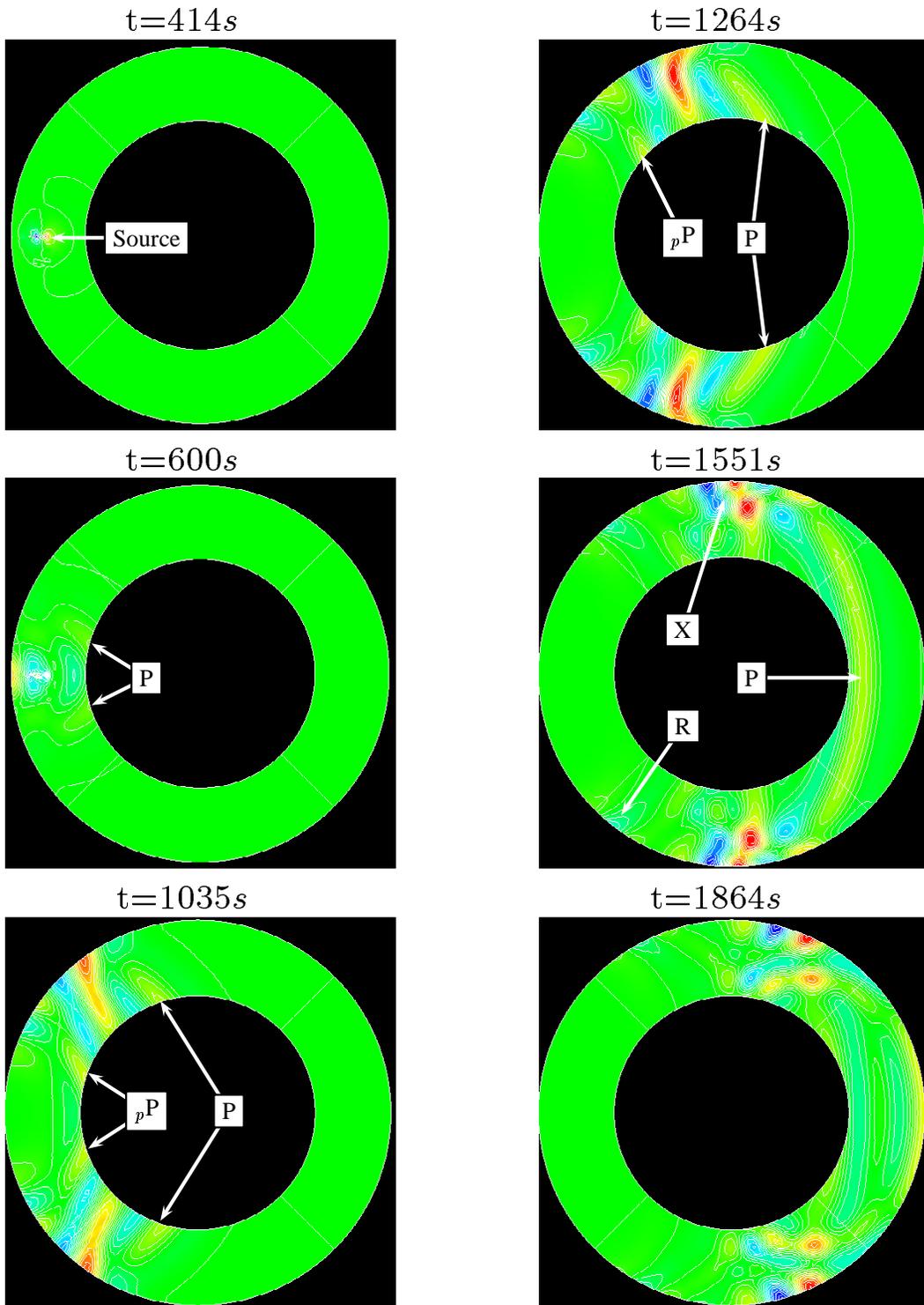
Y. Capdeville, E. Chaljub, J.P. Vilotte and J.P. Montagner
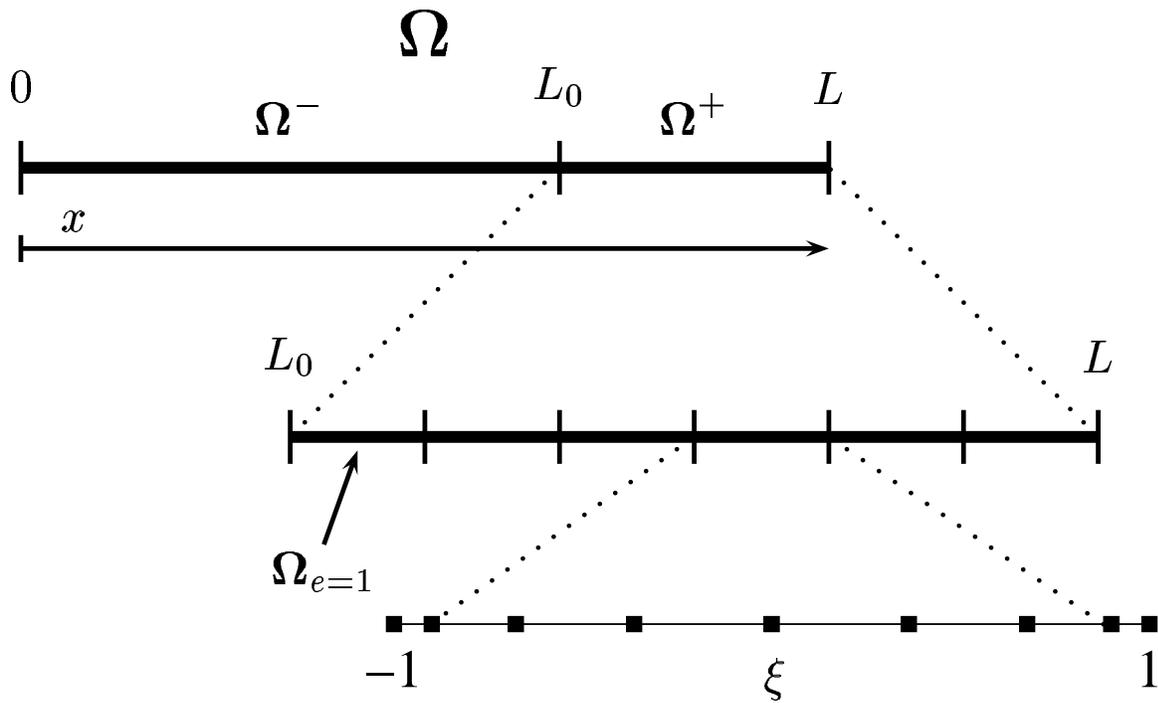
ms#XXXX : Figure 1

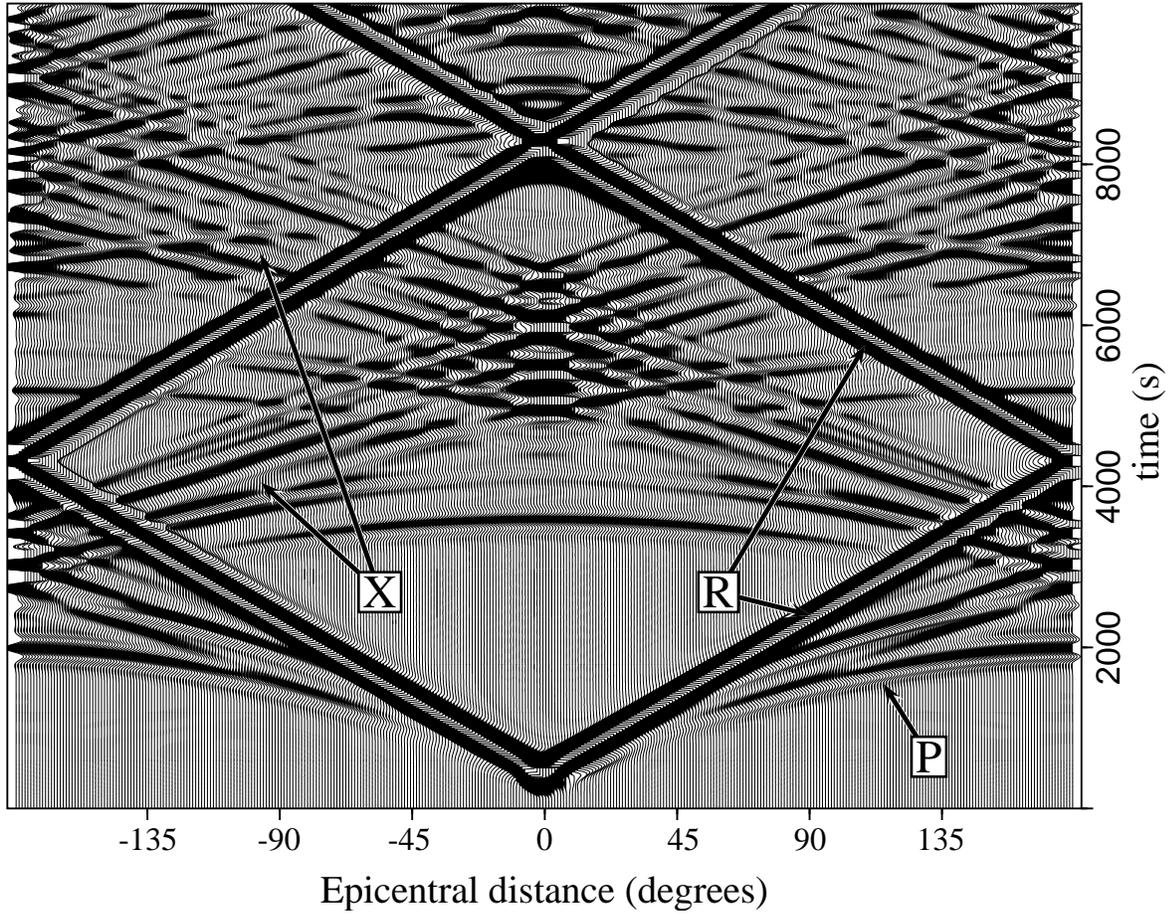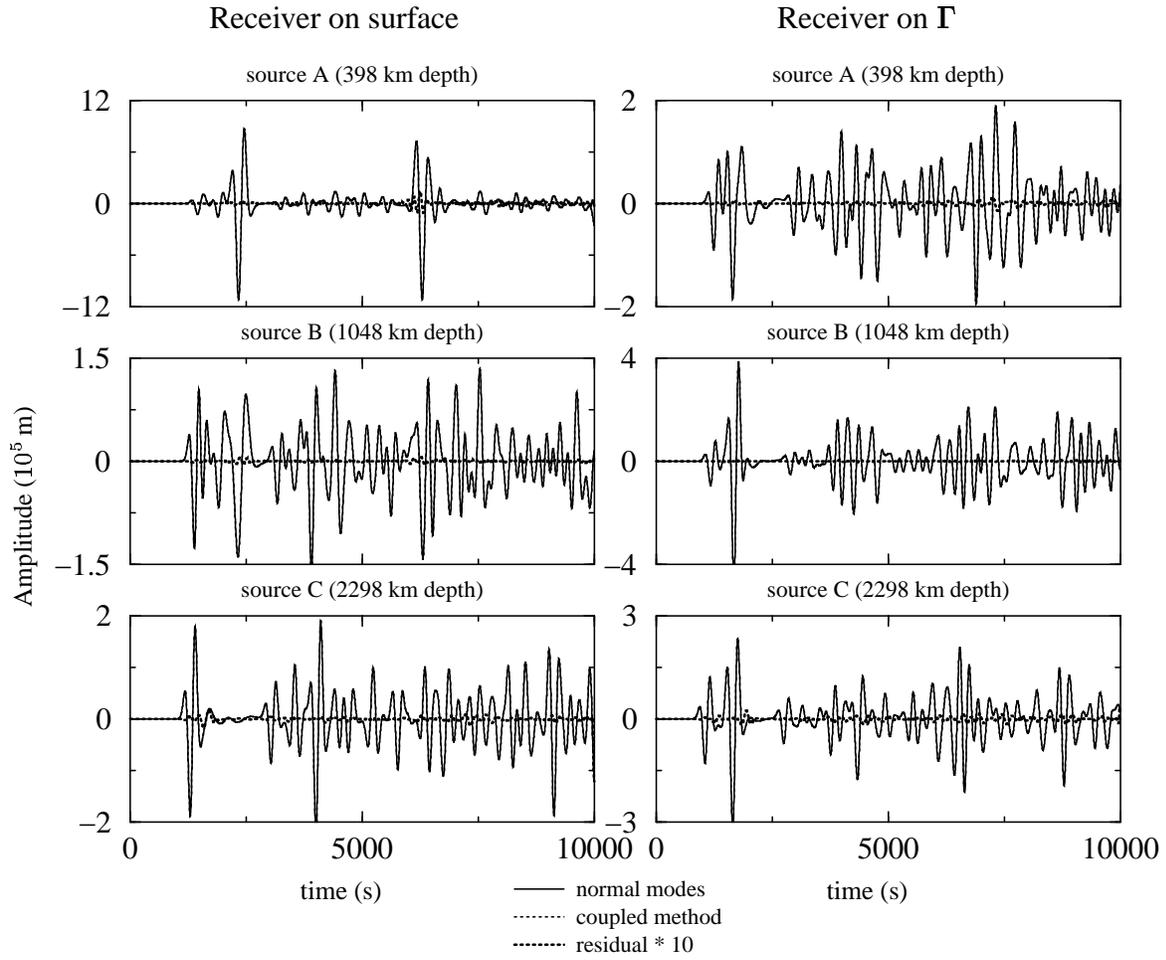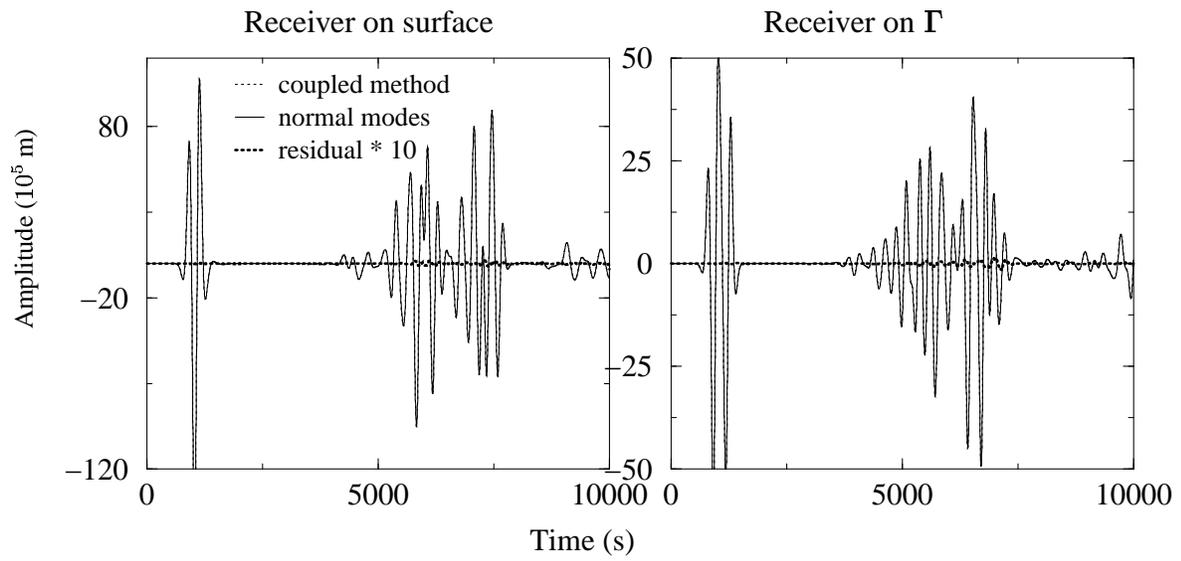**Y. Capdeville, E. Chaljub, J.P. Vilotte and J.P. Montagner**
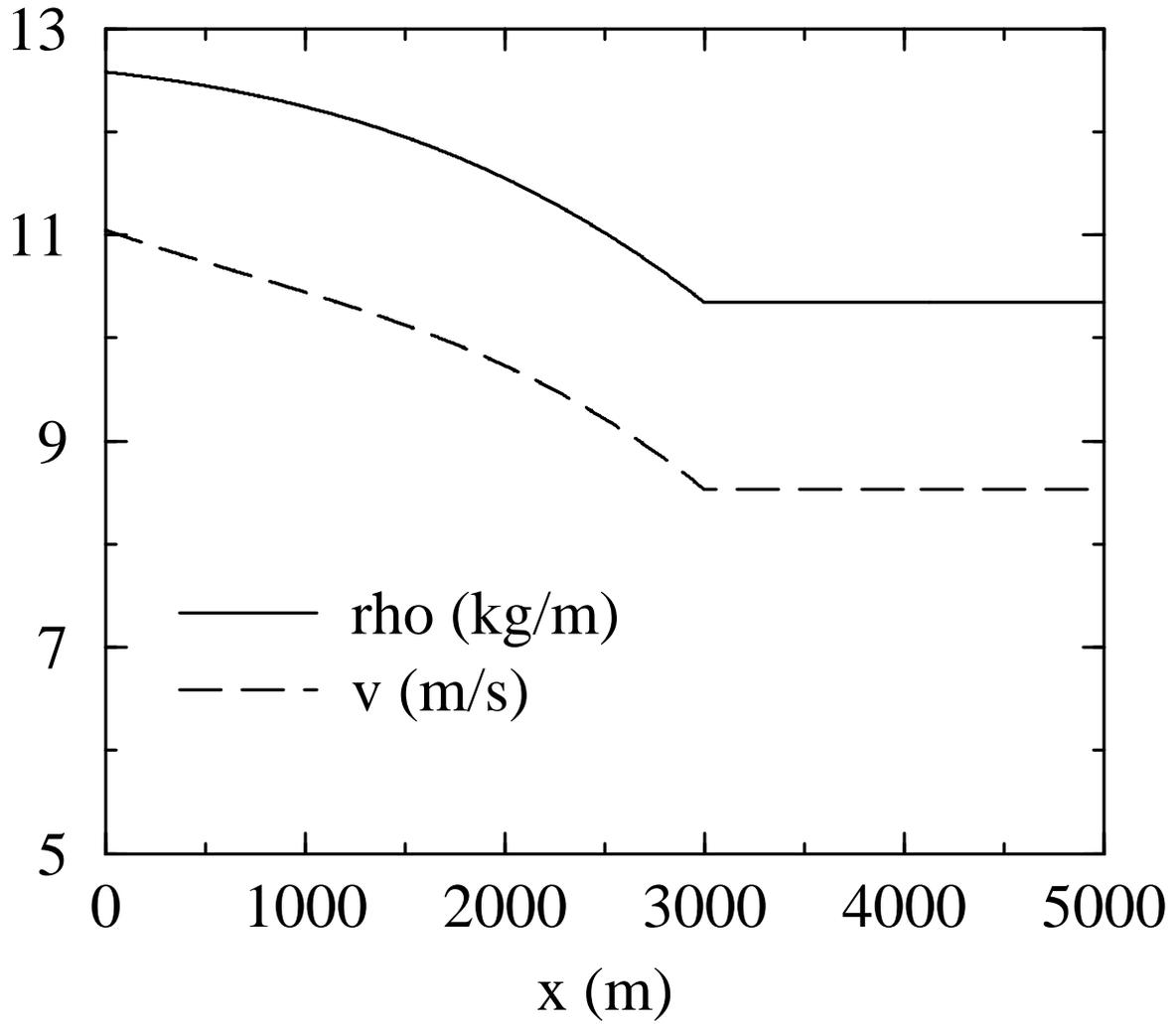
ms#XXXX : Figure 2

Y. Capdeville, E. Chaljub, J.P. Vilotte and J.P. Montagner
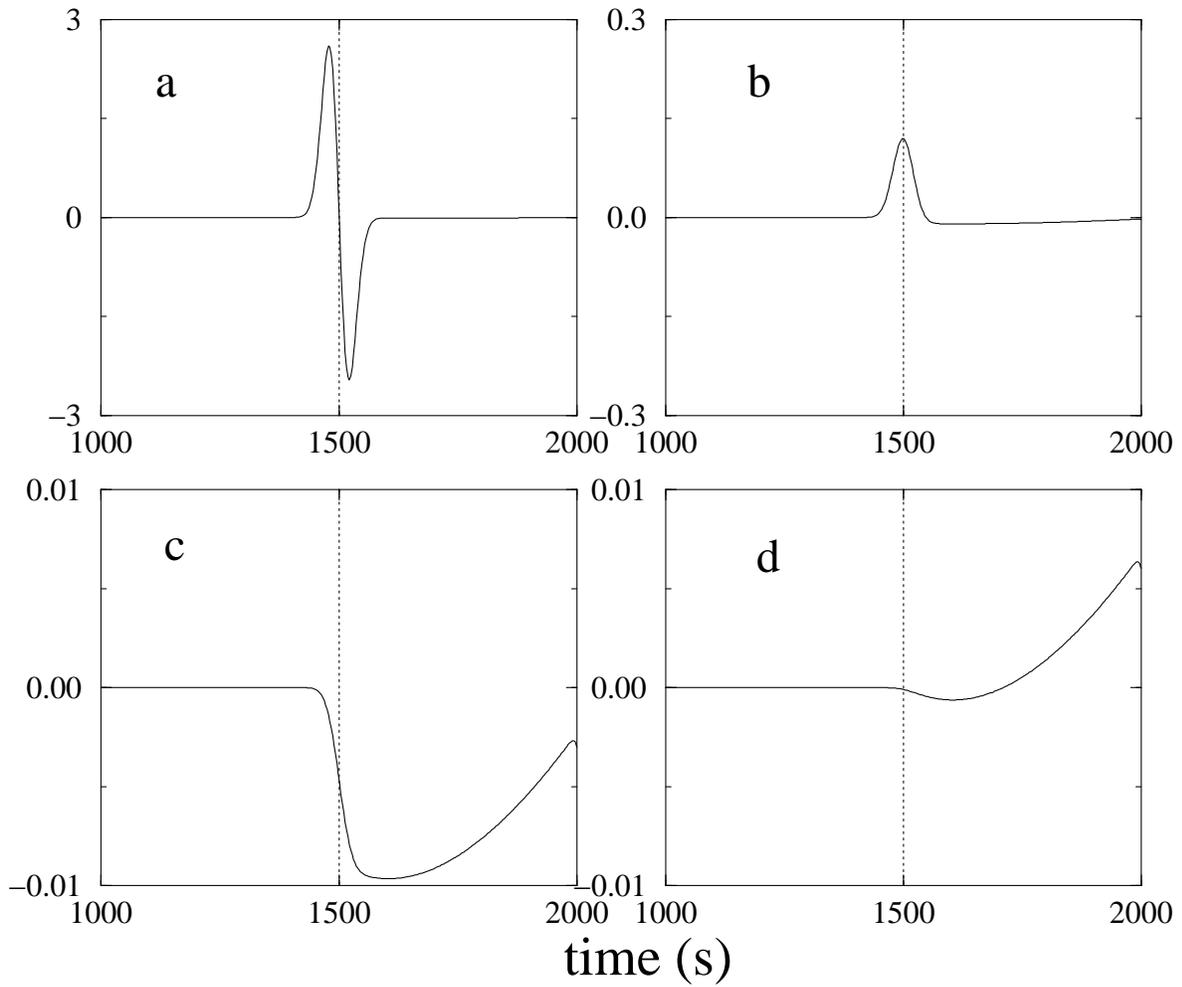
ms#XXXX : Figure 4

frag replacements

Y. Capdeville, E. Chaljub, J.P. Vilotte and J.P. Montagner

ms#XXXX : Figure 5

SEM
error 1 $\times 100$
error 2 $\times 100$
error 3 $\times 100$

time (s)

Y. Capdeville, E. Chaljub, J.P. Vilotte and J.P. Montagner

ms#XXXX : Figure 6

frag replacements
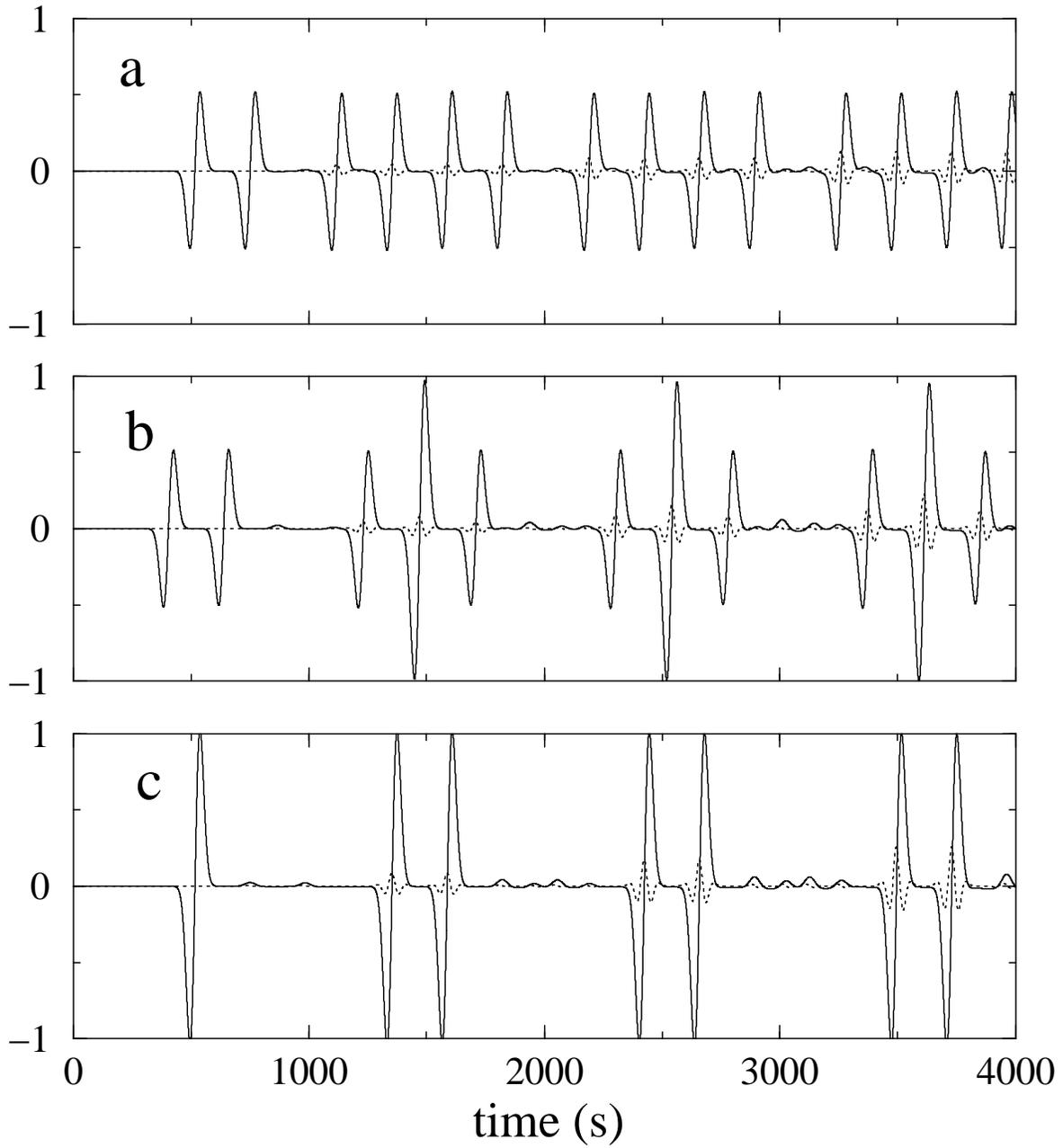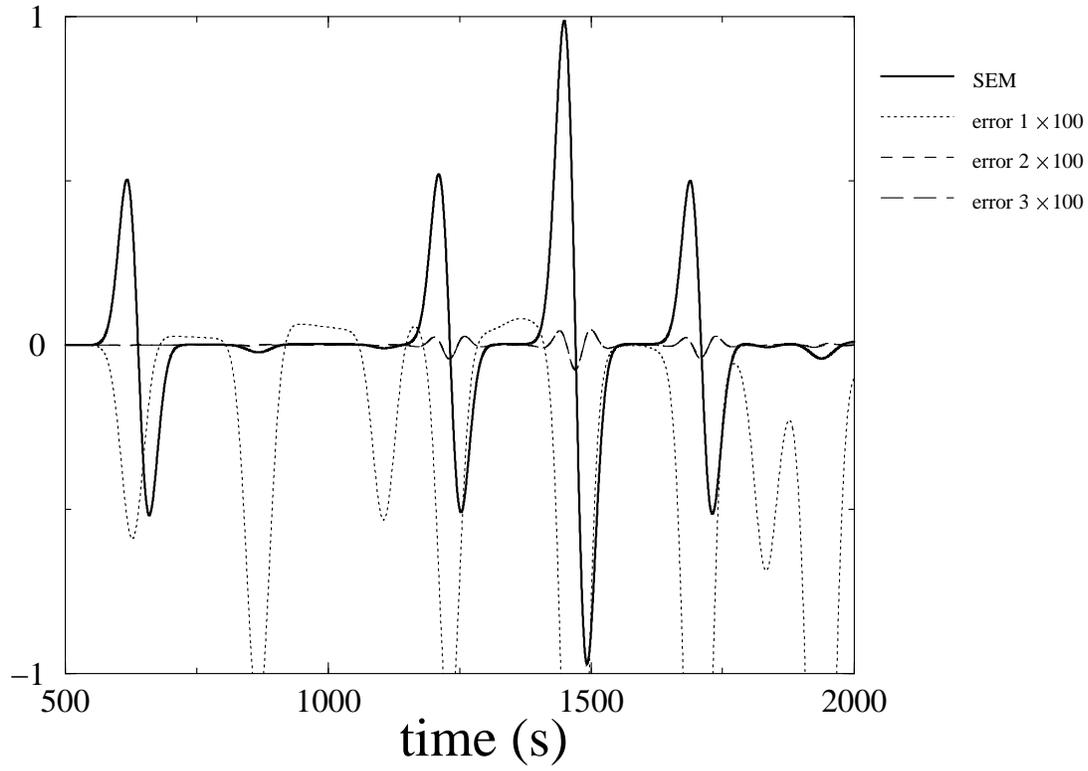
Y. Capdeville, E. Chaljub, J.P. Vilotte and J.P. Montagner

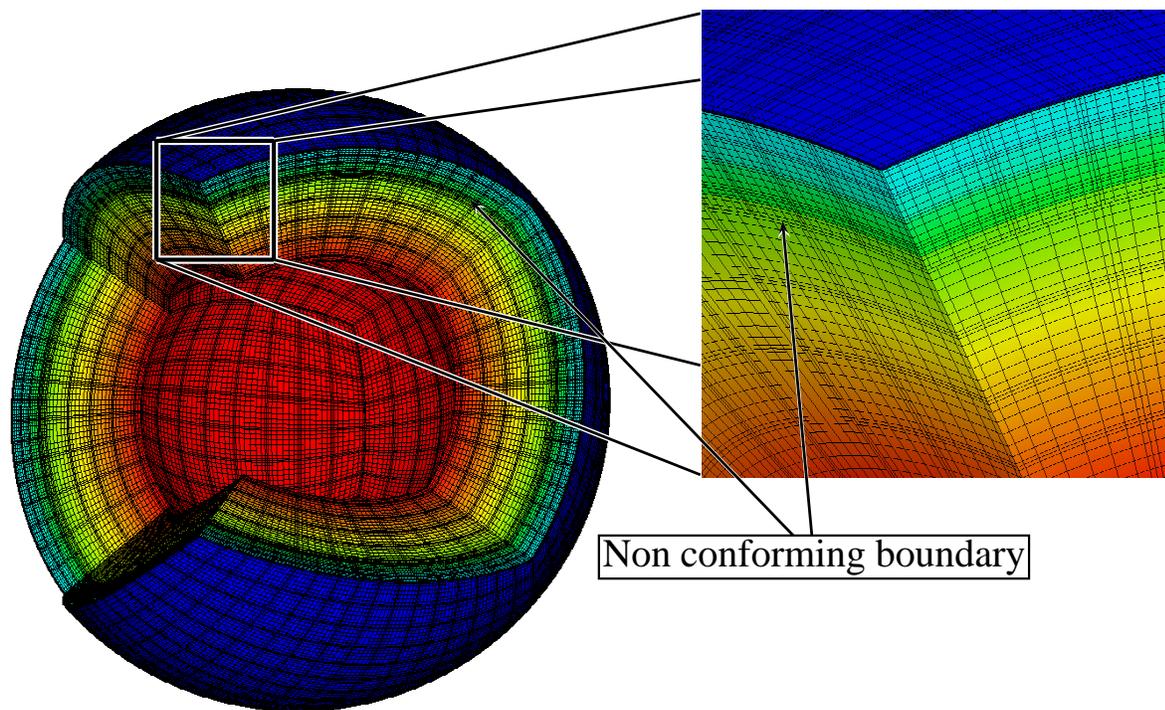**ms#XXXX : Figure 7**
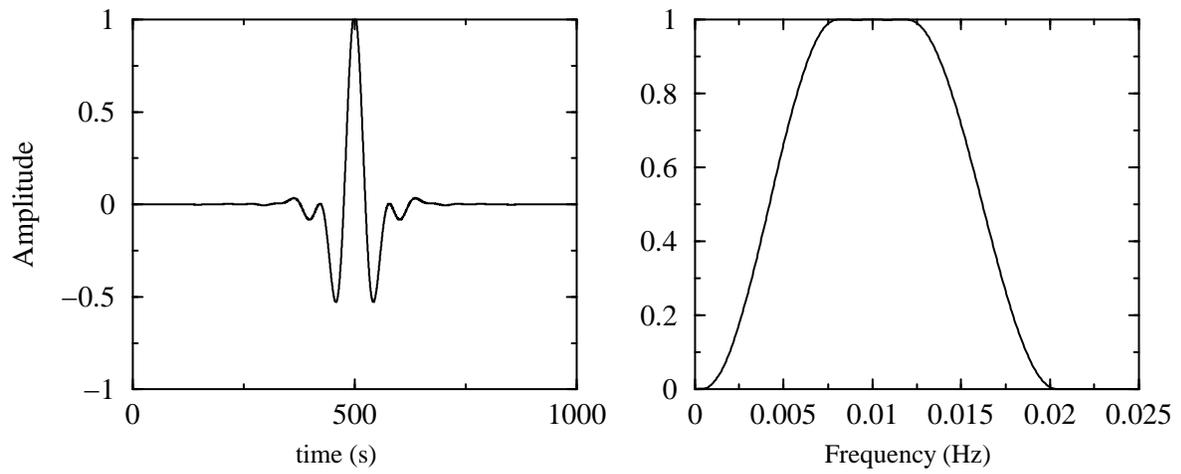
North

West

East

South

Y. Capdeville, E. Chaljub, J.P. Vilotte and J.P. Montagner

ms#XXXX : Figure 8

Y. Capdeville, E. Chaljub, J.P. Vilotte and J.P. Montagner

ms#XXXX : Figure 9
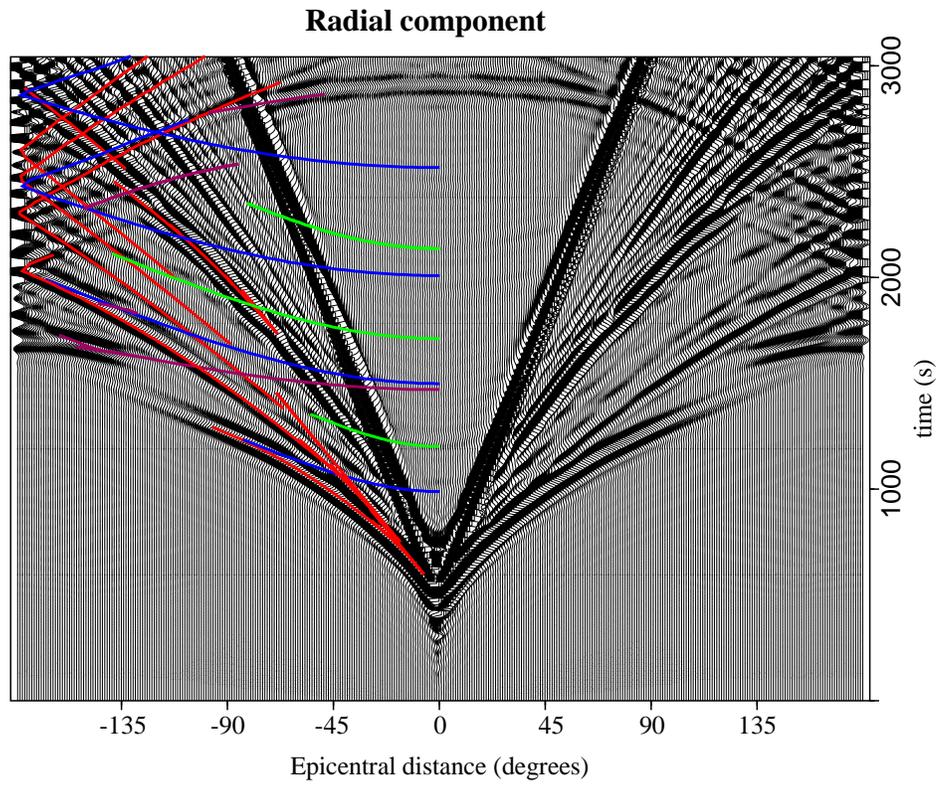
Sphéroïdal eigenfrequencies

Toroïdal eigenfrequencies

Y. Capdeville, E. Chaljub, J.P. Vilotte and J.P. Montagner

ms#XXXX : Figure 10

Y. Capdeville, E. Chaljub, J.P. Vilotte and J.P. Montagner

ms#XXXX : Figure 11

frag replacements

Y. Capdeville, E. Chaljub, J.P. Vilotte and J.P. Montagner

ms#XXXX : Figure 12

Vertical component

Y. Capdeville, E. Chaljub, J.P. Vilotte and J.P. Montagner

ms#XXXX : Figure 14

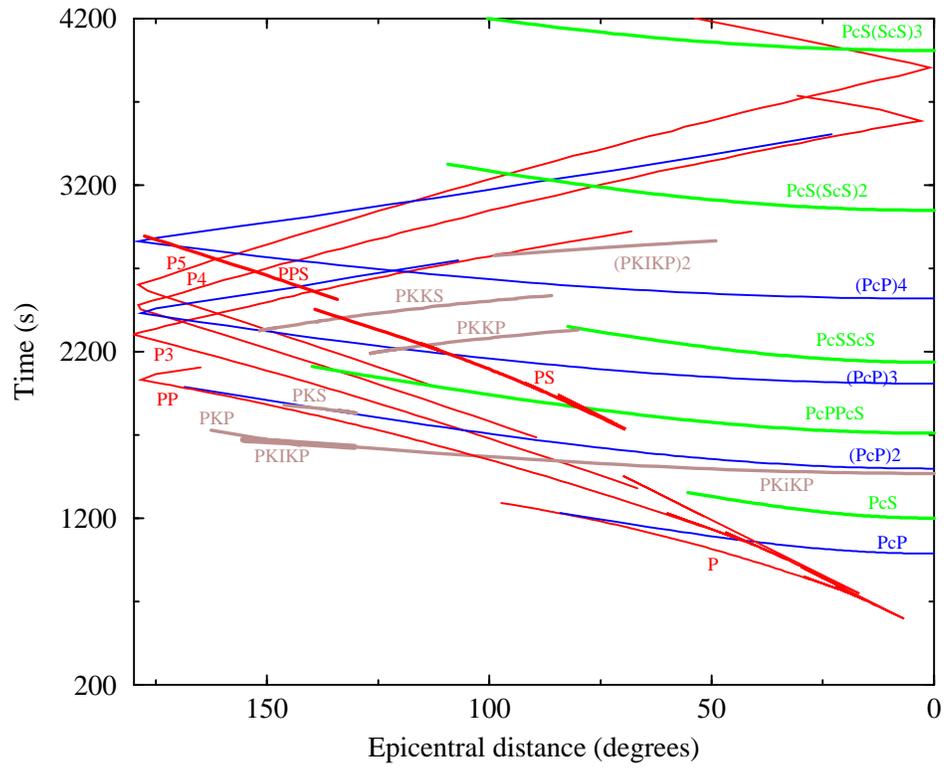PSfrag replacements
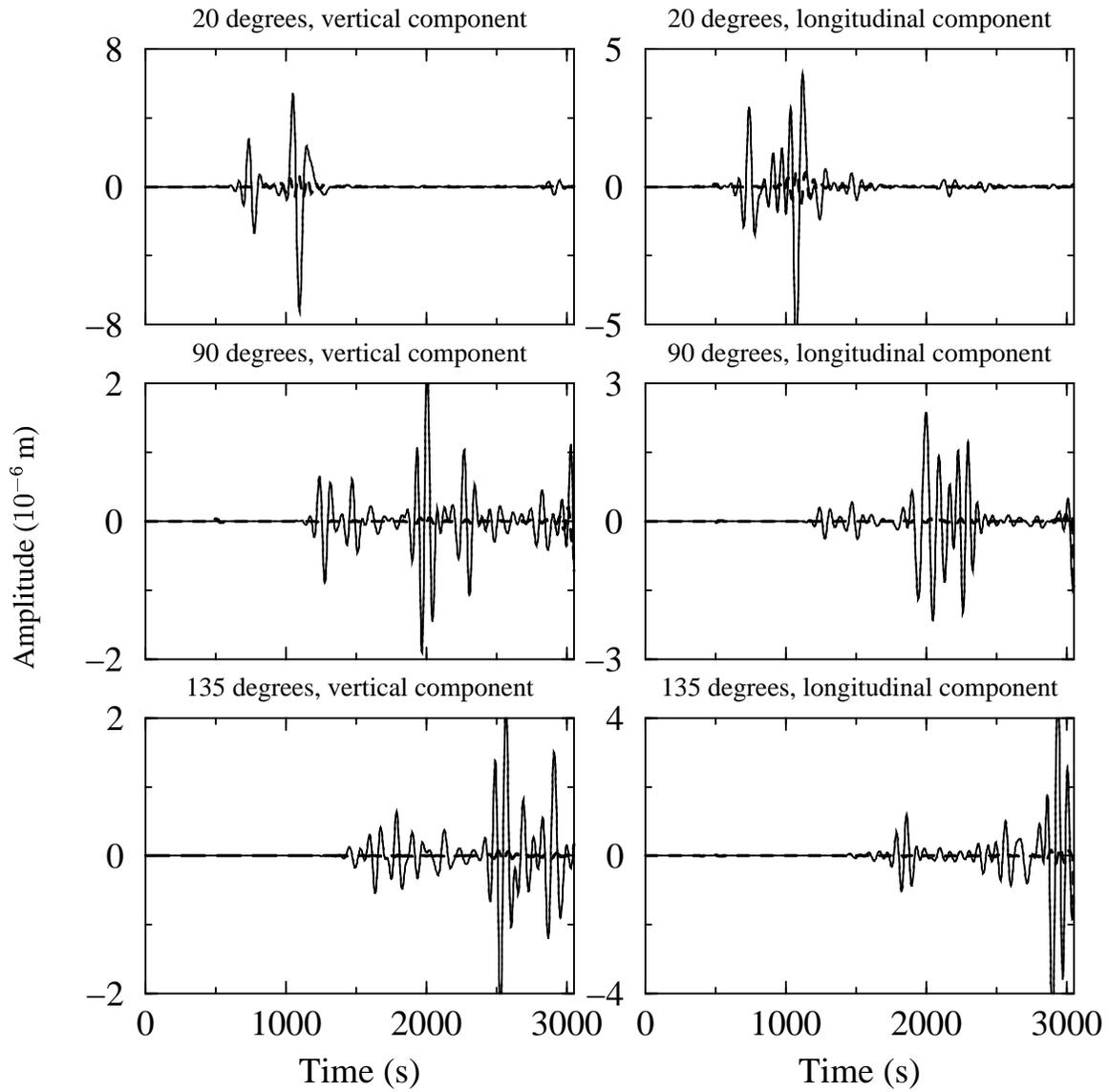
frag replacements

Y. Capdeville, E. Chaljub, J.P. Vilotte and J.P. Montagner

ms#XXXX : Figure 15

Y. Capdeville, E. Chaljub, J.P. Vilotte and J.P. Montagner
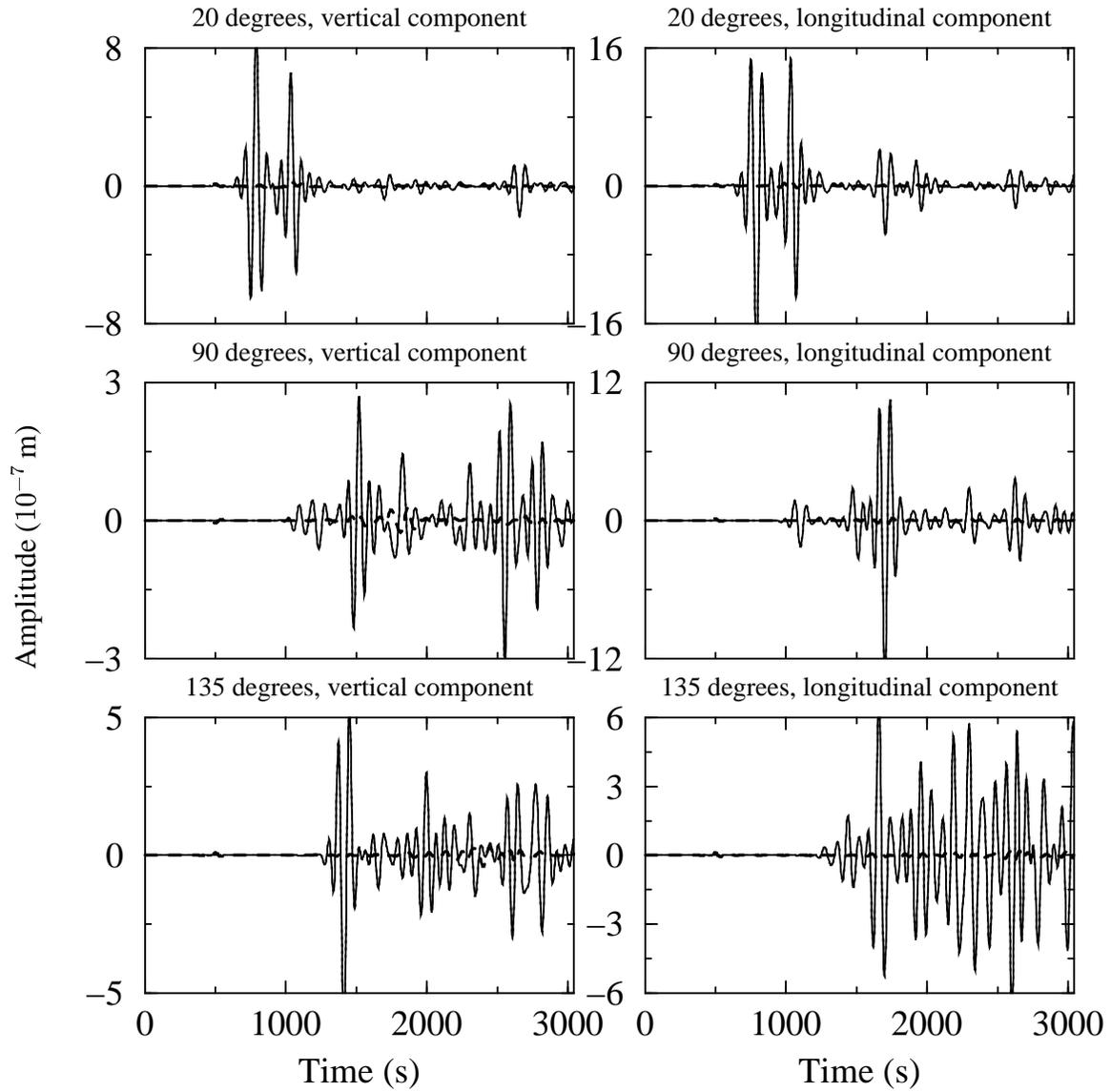
ms#XXXX : Figure 16

Non conforming boundary

Y. Capdeville, E. Chaljub, J.P. Vilotte and J.P. Montagner

ms#XXXX : Figure 17

Y. Capdeville, E. Chaljub, J.P. Vilotte and J.P. Montagner

ms#XXXX : Figure 18

Radial component

Y. Capdeville, E. Chaljub, J.P. Vilotte and J.P. Montagner

ms#XXXX : Figure 19

Y. Capdeville, E. Chaljub, J.P. Vilotte and J.P. Montagner

ms#XXXX : Figure 20

Y. Capdeville, E. Chaljub, J.P. Vilotte and J.P. Montagner

ms#XXXX : Figure 21

Y. Capdeville, E. Chaljub, J.P. Vilotte and J.P. Montagner

ms#XXXX : Figure 22